KU LEUVEN

FACULTY OF SCIENCE

Merging Compact Objects in the LISA Frequency Band

Hypercompact stellar clusters and the gravitational-wave background

Seppe STAELENS

Supervisor: Prof. G. Nelemans
KU Leuven, RU Nijmegen

Co-supervisor: Prof. P. Jonker
RU Nijmegen

Thesis presented in
fulfillment of the requirements
for the degree of Master of Science
in Astronomy and Astrophysics

Radboud Universiteit

Academic year 2022-2023

© Copyright by KU Leuven
Without written permission of the promoters and the authors it is forbidden to reproduce or adapt in any form or by any means any part of this publication. Requests for obtaining the right to reproduce or utilize parts of this publication should be addressed to KU Leuven, Faculteit Wetenschappen, Geel Huis, Kasteelpark Arenberg 11 bus 2100, 3001 Leuven (Heverlee), Telephone +32 16 32 14 01. A written permission of the promoter is also required to use the methods, products, schematics and programs described in this work for industrial or commercial use, and for submitting this publication in scientific contests.

"Déjà vu, I've just been in this place before."
- Dave Rodgers

Preface

After midnight. It's dark outside, and my energizing music is playing. At the moment, my thesis is still sprinkled with red-colored comments and todo's, but most of the text is written. I recognize this feeling from last year: almost done. When I told people that I would do another Master, their reaction was: *"Does that mean another thesis?"*, as if it is something daunting and utterly unpleasant. To be fair: it has been over 25 degrees all week, and that means I would rather join my friends at the beach instead of writing in my room all day. But, the research over the past few months *was in fact pleasant*. Just like last year, I feel confident that research is something that I would like to do in the foreseeable future. Going abroad this year (yes, the Netherlands can barely be considered abroad as a *Vlaming*) was scary at first, but it has been an amazing experience overall. This thesis represents the end of my year in Nijmegen, and therefore words of appreciation are in order.

First of all, I would like to thank prof. Gijs Nelemans and prof. Peter Jonker, who managed to provide me with two very interesting projects on short notice. I think it's amazing that both projects combined astrophysics with my previous knowledge in theoretical physics, which really caused them to spark my interest. I thank both of you for the efficient guidance, and trusting me and allowing me to work very independently. Both of you have also taught me a lot about the life as an academic, and I thank you for these off-topic conversations as well.
Furthermore, I already want to thank dr. Daniel Mayerson and dr. Pablo Marchant for willing to be the readers of my thesis.

This year, I have not only finished my Master in Astronomy and Astrophysics, but I have also taken my first big steps as a real scientist. A ~~million~~ billion thanks go out to Daniel, Fabio and Bart for helping me to convert the results of my previous thesis, together with additional more recent results, into my first official scientific paper - at this moment accepted for publication in *Physical Review D*. Another billion thanks go out to you for the talks, advice and support in shaping my future. I am excited to take on the next challenge, a PhD at the University of Cambridge, and I want to thank all the other people that helped me to get this position: in particular prof. Thomas Hertog and prof. Gijs Nelemans, for writing letters of recommendation, my parents, sister and Anouk for advice on CV's and motivation letters, and Cédric for proofreading my application late in the evening in *Villard-Reculas*.

This exchange would not have been such an amazing experience, if it wasn't for the amazing people that I met here. My inextendible love goes out to my fellow *best mentors for*

life. Dan, you have been my *mate* here all year, and I thank you for the gym and running sessions, the many laughs, the introduction to English culture and the occasional beer. I truly hope we see each other again the coming years, on the island. Salomé, I have told you this many times already, but I have an enormous amount of respect for you and your personality. Even though you're still *so* young, I admire your maturity and permanent *joie de vivre*. I hope I will hear your exuberant laugh many more times, perhaps in the world city of *Monfaucon*. Sarah, you have been here for me, literally since day one. You were the first person here that I could confidently call *my friend*. I thank you for being my flatmate, our *Breaking Bad* evenings, and most of all for being there for me when things were tough. Even though it wasn't always clear, I love you.
There are many more people that I met this year that I will miss when leaving. In no particular order: Chris, Kinga, Aideen, Alex, Anna, Anouk, Rhys, Andria, Ruby, Camilla, Giorgia, Maria, Samin, James, Anne-Sophie, Alex, Max, Holly, Laurine, Timi, Jas, Markéta, Angéline, Berit, Sari and the people from NSJV Zanshin. Thank you all for this unforgettable year.

Furthermore, I want to extend the love back to Belgium, and thank my parents, brother and sister (*ja, Zoë, Kwinten, bij naam zelfs deze keer*) and the rest of my family for their everlasting love and support. Additionally, even though I haven't seen you as much as I'd like to this year, I'd like to thank my friends Bram, Cédric and Matthieu for always being there for me. More love is extended to all inhabitants and visitors of *Casa del Koe* for providing a place to crash when I needed it.

Finally, I would like to extend my gratitude to dr. Eugene Vasiliev and dr. Nicholas Stone for discussions on the Coulomb logarithm, `PhaseFlow` and sink terms in the Fokker-Planck equation. Your input has proved valuable, and I am grateful for you taking time out of your undoubtedly busy schedules to help me out.

To you, reading this, I thank you for taking interest in my work. I proudly present you my Master's Thesis.

Seppe Staelens

Summary

As of 2015, a new window on the Universe has opened with the first ever direct detection of a gravitational wave. Today, ground-based interferometers have detected about ∼90 events, providing remarkable confirmations of the predictions of General Relativity as well as many new insights into black holes and neutron stars. These ground-based detectors operate in the high-frequency regime, with optimal sensitivity between ~ 10 and ~ 1000 Hz.

However, in this high-frequency regime, only the final stage of the inspiral of stellar-mass compact binaries is visible. There are many more expected phenomena that can be observed in the gravitational-wave sky, but are only visible at lower frequencies. To this end, the space-based LISA detector is set to launch in the mid 2030s. LISA will allow us to study gravitational waves in the frequency regime between 10^{-5} Hz and 0.1 Hz. This will allow us to see merging white dwarves, EMRIs, merging massive black holes and perhaps many more exciting phenomena that we are unaware of.

In this thesis, we explore two topics related to LISA science objectives, with the goal of adding to the extensive amount of preparatory work before the data will actually be obtained.

In first instance, we will focus on the gravitational-wave background sourced by extragalactic white-dwarf binaries. This is the sum of all the signals produced by binary white dwarves located outside of our Milky Way, which are individually unresolvable. We revisit old predictions for this background, and compare them to current best estimates for the (undetected) background due to binary black holes and neutron stars in the high-frequency band. This shows that the background from white dwarves is likely the dominant one between $\sim 10^{-4}$ Hz and 0.1 Hz., when these estimates are extrapolated to the LISA band. We determine our own prediction for the background due to extragalactic white dwarves, and find an amplitude at 1 mHz that is roughly a factor 5 larger than the original estimates. Due to this larger amplitude, the peak in the background around 10 mHz might be more easily resolved by LISA. Furthermore, we investigate how the background changes for other explorative models of the cosmic star formation history, and find that the effect is minor.

On the other hand, we also consider so-called hypercompact stellar clusters. These putative systems are predicted to form when supermassive black holes merge in star-rich environments, as would for example happen when galaxies merge. These clusters remain absent in observations, though studies predict that hundreds of these systems should be

observable. As one of LISA's main science objectives is to study the formation history of supermassive black holes, the detection of such a cluster would provide evidence that these mergers actually happen, and could provide a lot of information on the formation history of supermassive black holes.

Predictions for the observational properties of these clusters exist, but so far the inclusion of stellar-mass black holes was not considered in simulations. We take a first step in incorporating a stellar-mass black hole population, and find that their presence can cause the scale of the cluster to increase significantly. Using our new models, we focus on some specific faint Milky Way halo clusters that could potentially be these elusive clusters. We explore the parameter space that causes our model to agree with the observed properties of these candidates, and estimate the three-dimensional velocity dispersion. This quantity could help to determine the nature of the candidates.

Summary for a General Audience

In 1915, Einstein published his *Theory of General Relativity*, which provided a description of gravity in a revolutionary way. His theory has many profound implications, among which the existence of *gravitational waves*. These waves are ripples *of space itself*, meaning that they essentially distort lengths when they pass through the Earth. Gravitational waves arise as a consequence of the most violent events in the Universe, like for example the merger of two *black holes*. Luckily, these waves are created at distances far away from Earth, such that they have lost a lot of energy when they arrive at our detectors.

In 2015, such a gravitational wave was observed for the first time by the *Laser Interferometer Gravitational-Wave Observatory* (LIGO). By now, already 90 detections have been made, and provided the scientific community with a lot of information. The limitation of our current detectors is that they operate at *high frequencies*, between $\sim$ 10 Hz and $\sim$ 1000 Hz. This means that they can only see a small part of all the gravitational waves that are being created in the Universe.

The future space-based detector LISA, set to launch in the mid 2030s, aims to solve this problem. It will consist of three identical spacecraft that form an equilateral triangle with arms around 2.5 million km. They will shoot lasers in between them, as they can detect the effect of gravitational waves. Due to this new configuration, LISA will be most sensitive to waves with frequency between 0.01 mHz and 0.1 Hz. Therefore, LISA will see different phenomena than our ground-based detectors, leading to a new treasure of information.

In this thesis, we explore two topics related to LISA science goals. On the one hand, we will study the gravitational wave background due to extragalactic white-dwarf binaries. This is the collective signal of all the binary *white dwarves* (remnants of stars with a mass below 8 times that of the Sun) outside of the Milky Way, which LISA may be able to measure. We make our own prediction of how strong this signal is, and investigate whether it can be distinguished from other background signals.

On the other hand, we explore hypercompact stellar clusters. These systems are created when two supermassive black holes, with masses millions or billions of times that of our Sun, merge. They have not been observed yet, but we investigate whether the presence of small black holes, with masses only tens of times that of the Sun, could alter the predictions of the appearance of these clusters. We then compare our models to some observational candidates, and discuss how measuring the velocities of the stars in these candidate systems could lead to a definitive conclusion on their nature.

Contribution Statement

The idea of the dominant contribution of white dwarves to the total background came from my supervisor, prof. Nelemans. I have independently provided evidence for this claim, by making the extrapolation of the LVK estimates, resulting in Figure 2.3. The order-of-magnitude argument was the idea of my supervisor, however. The work in sections 2.4 and 2.5 is my own, although the theory in sections 2.4.1 and 2.5.1 is largely based on [Farmer and Phinney, 2003]. This includes all the figures in these sections, as well as the code that produced all of these results and figures. The results of the population synthesis code were given to me, and I did not have to run this myself.

Similarly, the idea to add stellar-mass black holes to the models of hypercompact stellar clusters was that of my supervisor, prof. Jonker. The work in sections 3.3.3, 3.4 and 3.5 is my own, including all the figures. The hyperplane (3.29) is the result of my own research, and is to my knowledge not remarked on in the literature.

List of Common Symbols

c	Speed of light
E	Energy
F	Flux
f	Gravitational-wave frequency
f_e	Gravitational-wave frequency in the source frame
f_r	Gravitational-wave frequency in the observer's frame
γ	Exponent of the stellar density distribution
L	Luminosity
$\ln \Lambda$	Coulomb logarithm
M_b	Mass of stars that remain bound to the SMBH
$M_\bullet$	Mass of the SMBH
$\mathcal{M}$	Chirp mass of a binary
$M_\odot$	The mass of the Sun, equal to $1.989 \cdot 10^{30}$ kg
ν	Orbital frequency of a binary
Ω	Dimensionless energy density
ψ	Star formation rate
r_{eff}	Projected half-light radius of a HCSC
r_k	Scale radius of a HCSC
σ	Velocity dispersion
V_k	Kick velocity
z	Redshift

List of Common Abbreviations

BH	black hole
FP	Fokker-Planck
GC	globular cluster
GR	General Relativity
GW	gravitational wave
GWB	gravitational-wave background
HCSC	hypercompact stellar cluster
pHLR	projected half-light radius
LISA	Laser Intereferometer Space Antenna
NS	neutron star
PS	population synthesis
PTA	pulsar timing array
SFH	star-formation history
SFR	star-formation rate
SMBH	supermassive black hole
smBH	stellar-mass black hole
TDE	tidal distruption event
WD	white dwarf

List of Figures

List of Tables

Contents

Chapter 1

Introduction

Our Universe is filled with stars, illuminating the dark emptiness of space. They are born out of clouds of dust and gas that collapse under their own gravity. Once the density has become sufficiently large, resulting in strong heating of the matter, a nuclear engine in the center ignites: energy and radiation get transported outwards, and a star is born. The lifecycle of the new-born star depends largely on its mass[1]. The minimal mass for a protostar to ignite is $\simeq 0.08 M_{\odot}$. Objects that fall below this limiting mass don't ignite and are referred to as *brown dwarfs*.

Above this critical mass, stars usually manage to start the first stage of nuclear burning, in which hydrogen is the fuel for the fusion reaction. When a star is burning hydrogen in equilibrium, it is said to be on the *main sequence* (MS). Stars spend most of their life on this main sequence, burning hydrogen in their cores, but at some point most of the fuel will be used. The core will now largely consist of helium - the product of hydrogen burning. The temperature in the core is not high enough to start the burning of helium. The core will contract to increase the temperature, as the fusion of helium requires a temperature much larger than was necessasry for hydrogen (10^8 K vs. $\sim 5 \cdot 10^6$ K). The exact details depend on the mass of the star, but there are three main outcomes, which we discuss in Sec. 1.1 (largely based on [Aerts, 2021]). Afterwards, we give a short introduction to gravitational waves in Sec. 1.2, and present the future gravitational-wave detector LISA in Sec. 1.3. This thesis is centered around 2 science topics that can be explored with this instrument, and we present our concrete goals and motivation in Sec. 1.4.

1.1 Stellar remnants

The luminosity L - the rate at which energy is radiated away - of a star is seen to increase when its mass M increases. Over the majority of the mass range, the relation

$$L \propto M^{3.3} \tag{1.1}$$

[1]This is the case for isolated stars. However, the majority of massive stars is expected to experience binary interaction [Sana et al., 2012]. This affects the stellar evolution, such that the life of a star in a binary can differ significantly from that of a similar star in isolation.

provides a good fit. Given that the energy reservoir available for nuclear fusion scales with M through Einstein's mass-energy relation, the lifetime T of a star scales as

$$T \propto \frac{M}{L} \propto M^{-2.3}\,. \tag{1.2}$$

This shows that the lifetime of stars drastically decreases when the mass increases, i.e. the more massive the star, the shorter its lifetime.

Stars with an initial mass $\lesssim 0.9M_\odot$ have main-sequence lifetimes that are longer than the current age of the Universe, and are therefore all still in their hydrogen burning phase. we focus and stars above this bound, which are all massive enough to start helium burning when the hydrogen in the core is depleted. In order to start a new burning cycle, the core of the star contracts to increase the temperature, enabling fusion of the next element: helium. Depending on the mass of the star, it can go through other burning cycles as well[2].

If the initial mass is $\lesssim 8M_\odot$, the burning of fuel will come to a halt before the core consists of iron. The star will lose a large part of its outer envelope (e.g. due to stellar winds or binary interaction), leaving only the core behind, which cools to a white dwarf (WD). The pressure that keeps this remnant from collapsing is provided by the electrons in the core, which form a degenerate electron gas. WDs typically have sizes comparable to the Earth, and masses $\gtrsim 0.1M_\odot$ and $\lesssim 1.44M_\odot$, known as the Chandrasekhar limit. The mass distribution of WDs peaks around 0.6 $M_\odot$ [Torres et al., 2021, Tremblay et al., 2016].

Stars with initial masses $\gtrsim 8M_\odot$ will go through all the burning cycles until the core consists of iron. As iron is the most stable element, the fusion of iron does not produce energy, but requires energy. The star has no way of producing energy through nuclear fusion to counteract the gravitational force, and its life is about to end: the core collapses under its own gravity, and the star explodes as a *supernova*. Highly energetic photons dissociate the heavy elements that were formed in the fusion cycles, and the core of the star now becomes a mixture of electrons, protons and neutrons. The density increases drastically due to the collapse of the star, and the protons and electrons recombine to neutrons. The increase in core pressure produces a shock wave that propagates through the outer layers that surround the core of neutrons. These outer layers get expelled, and the pressure in the core becomes so high that the neutrons become degenerate. The degenerate neutron gas is able to prevent further gravitational collapse, and the remnant is called a neutron star (NS). These objects have radii of $\mathcal{O}(10)$ km, and masses thought to be $\lesssim 2M_\odot$ [Burgio et al., 2021].

If the star has an initial mass $\gtrsim 25M_\odot$, the remnant after the supernova is too heavy to persist as a NS. There is no known mechanism that can support a heavier compact object, meaning that gravity will win and the remnant collapses into a black hole (BH). BHs are characterised by the fact that they possess an *event horizon*, a boundary close to the BH that is only traversable in one direction. The gravitational pull is so strong that even light cannot escape once it has crossed this horizon.

[2]Each of these new cycles, e.g. carbon burning and silicon burning, happens on a time-scale that is very short compared to that of the previous cycle.

It is important to make the distinction between theoretical and astrophysical black holes. The former are spacetimes, solutions of the Einstein equations in General Relativity (GR), that contain a singularity. The most famous examples are the Schwarzschild and Kerr spacetimes, which describe a non-rotating and rotating (uncharged) BH respectively. However, it is very hard to prove that the BHs we see in space actually correspond to these theoretical objects. So far, there is no evidence that this is not the case.

By now, there is extensive observational evidence for all three of these objects. WDs were originally discovered as very faint stars with spectra that did not match other stars of low luminosity [Adams, 1914, Flammarion, 1877, Van Maanen, 1917]. By now, tens of thousands white dwarves have been observed [Eisenstein et al., 2006, Gentile Fusillo et al., 2021].

Due to the conservation of angular momentum, a star that collapses to a NS causes the latter to have an enormous angular frequency, which can be $\mathcal{O}(10)$ Hz. The discovery of *pulsars* [Hewish et al., 1968], radio sources that show pulses with similar frequencies, established the existence of NSs. They are thought to originate from rapidly spinning NSs where the rotation axis and magnetic poles are misaligned. These pulses cannot be explained by rotating WDs: the centifugal force would cause the WD to get disrupted. Furthermore, observations of a NS binary lead to the first indirect detection of gravitational radiation [Taylor et al., 1979].

The first observational evidence for a BH came in 1972, when astronomers investigated the binary system Cygnus X-1. By analyzing the X-ray spectrum originating from the binary, together with the radial velocities of the visible companion, there was conclusive evidence that the companion of the star is a compact object [Bolton, 1972, Webster and Murdin, 1972]. As the mass of this invisible companion was estimated to be larger than $2M_{\odot}$, which is assumed to be too large for a white dwarf or neutron star, the authors concluded that the companion was possibly a black hole. The existence of BHs as astrophysical objects has since been solidified, culminating in the first direct observation of merging black holes with the use of a gravitational-wave detector [et al., 2016] and the direct imaging of the surroundings of a supermassive black hole (SMBH) by the Event Horizon Telescope [et al., 2019, 2022].

Even though the BHs as predicted by GR are able to explain current observations, it is expected that they are not the final description of these dark objects. Theoretical reasons for this exist, like the *information paradox* [Mathur, 2009] and the fact that we don't expect to see true infinities in nature. Therefore, other models for BHs have been given in theories that go beyond GR, that try to solve these problems [Cardoso and Pani, 2019]. Predictions have been made for their observational appearance (e.g. [Bacchini et al., 2021, Staelens et al., 2023]) and signatures in gravitational waves (e.g. [Guo et al., 2019, Konoplya and Zhidenko, 2011]), but as of today observations do not prefer them over the "classical" GR solutions.

1.2 Gravitational waves

The vast majority of knowledge that we have gathered about the Universe is the result of observations of electromagnetic radation. For centuries now, scientists have used telescopes to observe the night sky, and advances in technology have enabled us to look with increasing resolution and in different wavebands. However, as of 2015 a new window on the Universe has opened, with the first direct detection of a gravitational wave (GW) [et al., 2016]. GWs are a prediction of Einstein's theory of GR, and they are created in some of the most energetic events in the Universe. They enable us to study the gravitational force, in a way that complements the electromagnetic observations: the action of gravity on bodies is *dark*, meaning that we cannot expect all interesting events to be accompagnied with an electromagnetic signal. In this section, we review some basic aspects of the theory following [Carroll, 2019], briefly present the first succesful detectors.

1.2.1 Theory

Einstein's theory of GR relates the curvature of spacetime to the energy (matter) that is present in a region. The governing formula is

$$G_{\mu\nu} \equiv R_{\mu\nu} - \frac{1}{2} R g_{\mu\nu} = 8\pi T_{\mu\nu} \,, \tag{1.3}$$

where we set $G = c = 1$. In this formula, $R_{\mu\nu}$ and R are the Ricci tensor and scalar respectively, which are constructed out of first and second derivatives of the metric tensor $g_{\mu\nu}$. The metric tensor describes the spacetime, as well as the motion of particles in it. The right-hand side of (1.3) is proportional to the energy-momentum tensor $T_{\mu\nu}$, describing the matter and energy at every point in space. The interested reader can find some background on GR and the Einstein equations in Appendix A.

The easiest solutions of (1.3) can be obtained by setting the energy-momentum tensor to zero, i.e. vacuum solutions. For example, the Schwarzschild and Kerr solutions describe black holes, which are solutions of these vacuum equations. To study gravitational waves, we consider the case where the metric is almost that of flat space, i.e. the Minkowski metric $\eta_{\mu\nu} = \text{diag}(-1, 1, 1, 1)$. We decompose the metric as

$$g_{\mu\nu} = \eta_{\mu\nu} + h_{\mu\nu} \,, \tag{1.4}$$

where $h_{\mu\nu}$ is considered a perturbation on top of flat space, i.e. $|h_{\mu\nu}| \ll 1$. This assumption allows us to ignore terms that are of higher order in $h_{\mu\nu}$ - which is why it is also referred to as linearized gravity. For example, this means that the inverse metric is given by

$$g^{\mu\nu} = \eta^{\mu\nu} - h^{\mu\nu} \,, \tag{1.5}$$

where the indices on h are raised using the Minkowski metric. Using the metric (1.4) as an Ansatz, one can derive the linearized Christoffel symbols, Riemann tensor, Ricci tensor and scalar. Taking everything together, the linearized Einstein tensor becomes

$$G_{\mu\nu} = \frac{1}{2} \left(\partial_\sigma \partial_\nu h^\sigma{}_\mu + \partial_\sigma \partial_\mu h^\sigma{}_\nu - \partial_\mu \partial_\nu h - \Box h_{\mu\nu} - \eta_{\mu\nu} \partial_\rho \partial_\lambda h^{\rho\lambda} + \eta_{\mu\nu} \Box h \right) \,, \tag{1.6}$$

where $h = \eta^{\mu\nu} h_{\mu\nu}$ and $\Box$ is the d'Alembertian operator.

In principle, the metric tensor has ten independent components, as it can be seen as a symmetric 4×4 matrix. We decompose the metric perturbation as follows:

$$\begin{aligned} h_{00} &= -2\Phi \,, \\ h_{0i} &= w_i \,, \\ h_{ij} &= 2s_{ij} - 2\Psi\delta_{ij} \,, \end{aligned}$$

where Ψ is proportional to the trace of h_{ij} such that *the strain* s_{ij} is traceless:

$$\begin{aligned} \Psi &= -\frac{1}{6}\delta^{ij} h_{ij} \,, \\ 2s_{ij} &= h_{ij} - \frac{1}{3}\delta^{kl} h_{kl}\delta_{ij} \,. \end{aligned}$$

Due to the gauge freedom of GR, we can set the strain to be spatially transverse:

$$\partial_i s^{ij} = 0 \,. \tag{1.7}$$

The residual gauge freedom can be used to set

$$\partial_i w^i = 0 \,, \tag{1.8}$$

resulting in the so-called **transverse gauge**. Restricting to the vacuum case, the linearized Einstein tensor (1.6) tells us that, in the transverse gauge,

$$\begin{aligned} \Phi = \Psi &= 0 \,, \\ w_i &= 0 \,, \\ \Box s_{ij} &= 0 \,. \end{aligned}$$

We can summarise this as follows:

$$h^{\mathrm{TT}}_{\mu\nu} = \begin{pmatrix} 0 & 0 & 0 & 0 \\ 0 & & & \\ 0 & & 2s_{ij} & \\ 0 & & & \end{pmatrix} , \tag{1.9}$$

i.e. satisfying

$$\begin{aligned} h^{\mathrm{TT}}_{0\nu} &= 0 \,, \\ \eta^{\mu\nu} h^{\mathrm{TT}}_{\mu\nu} &= 0 \,, \\ \partial_\mu h^{\mu\nu}_{\mathrm{TT}} &= 0 \,, \\ \Box h^{\mathrm{TT}}_{\mu\nu} &= 0 \,. \end{aligned}$$

This is usually referred to as the **transverse traceless gauge**. The last of these equations is a wave equation. Therefore, we make the Ansatz

$$h^{\mathrm{TT}}_{\mu\nu} = C_{\mu\nu} e^{ik_\sigma x^\sigma} \,. \tag{1.10}$$

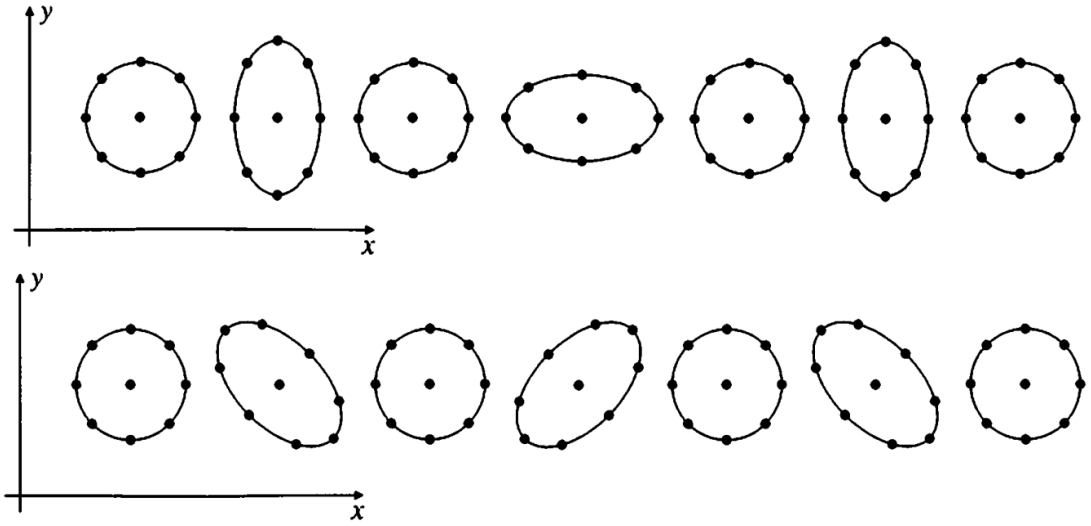

Figure 1.1: The effect of a gravitational wave on a ring of test particles, where the wave is polarized along the (*top*) "plus" polarization (*bottom*) "cross" polarization. The different figures correspond to different time instances. Figure taken from [Carroll, 2019].

The wave equation then results in $k_\sigma k^\sigma = 0$. So, demanding that the plane wave is a solution of the Einstein equations gives us that the wave vector must be null, i.e. the wave must travel at the speed of light. Ensuring that the wave is transverse gives us the condition that

$$k_\mu C^{\mu\nu} = 0\,. \tag{1.11}$$

This condition can be made more explicit by assuming a wave that travels in the z-direction, i.e. $k^\mu = (\omega, 0, 0, \omega)$, where ω is the frequency of the wave and the last component is fixed by the requirement that the wave vector is null. We then find that $C_{\mu\nu}$ takes the form

$$C_{\mu\nu} = \begin{pmatrix} 0 & 0 & 0 & 0 \\ 0 & h_+ & h_\times & 0 \\ 0 & h_\times & -h_+ & 0 \\ 0 & 0 & 0 & 0 \end{pmatrix}, \tag{1.12}$$

leaving only two independent components due to the requirement that $h^{\mathrm{TT}}_{\mu\nu}$ is symmetric and traceless. These two components are the two polarizations that a gravitational wave in GR can have[3]. The "plus" and "cross" polarization owe their name to the effect that polarized waves have on a circle of test particles, as can be seen in Figure 1.1.

The calculations outlined above form the most accessible explanation of gravitational waves in GR. Even though these calculations were performed shortly after Einstein published his theory, it was not until the 1960's that the existence of gravitational waves stood on firm footing. Even Einstein himself thought that the existence of these waves was a mere artifact of the coordinates, and would not have physical relevance. This changed

[3]The number of polarizations can increase in alternative theories of gravity. See e.g. [Hagihara et al., 2019].

with the pioneering work of e.g. Bondi, Sachs and Penrose, who created a new framework to deal with gravitational radiation, by working with the conformally completed spacetime [Bondi et al., 1962, Newman and Penrose, 1962, Sachs, 1962]. Since then, the physical reality of gravitational radiation seemed to be proven, and its consequencues were first observed less than two decades later [Taylor et al., 1979].

1.2.2 Ground-based detectors

Nowadays, the majority of gravitational-wave discoveries are attributed to the ground-based GW detectors. The most famous one is the Laser Interferometer Gravitational-Wave Observatory (LIGO), actually consisting of two detectors in Hanford and Livingston (USA). Together with Virgo (Italy) and KAGRA (Japan), they form the LVK collaboration, providing the majority of breakthroughs in the field.

All three are examples of a laser interferometer (see Figure 1.2). A standard interferometer consists of two perpendicular arms of length L, which is 4 km in the case of LIGO[4]. Each of these arms is formed by two mirrors, which reflect the light and increase the effective length of the arm by a factor ~ 300. When a gravitational wave passes through the observatory, it alters the length of both arms with a distance $\delta L_x, \delta L_y$, depending on the source location in the sky. The measured difference in length of the arms,

$$\Delta L(t) = \delta L_x - \delta L_y = h(t)L\,, \tag{1.13}$$

is expressed in a quantity $h(t)$ called the GW strain[5], which is on the order of 10^{-21} for the signals that LIGO detects. In the case that there is no wave passing by, the two laser beams interfere destructively, meaning that no light reaches the photodetector. However, when a wave passes by, the difference in length induces a phase difference in the beams, which no longer interfere destructively. Therefore, if light arrives at the detector, this must be due to a GW (assuming there is no noise). [et al., 2016]

The third gravitational-wave transient catalog (GWTC-3) [Abbott et al., 2021] contains 90 events that are likely of astrophysical origin, summarizing the detections of Advanced LIGO and Advanced Virgo up to the end of the third observing run. Most of them are binary BH mergers, but the catalog also contains two confident BH-NS binaries, and two NS binaries [Collaboration et al., 2022]. Other remarkable results include the first event detected by both LIGO and Virgo [et al., 2017] and a binary BH merger leading to an end product of $\sim 142 M_\odot$, falling in the mass range of *intermediate mass BHs* [et a;., 2020].

These ground-based interferometers operate in a *high frequency regime* (see Figure 2.1), on the order of 10-1000 Hz. In this band, they can detect signals from stellar-mass compact objects at low redshift. This is a consequence of Kepler's law (2.1), which we will come back to in Sec. 2.1. This means that these ground-based detectors are very good at detecting the actual merger of binaries consisting of BHs and NSs. However, they are insensitive to many other sources of GWs, which is why new detectors are being developed

[4]The arms of the Virgo and KAGRA detectors are about 3 km.

[5]The equation (1.13) should also contain a geometrical factor, as the relation between the strain and length difference depends on the source location with respect to the interferometer plane.

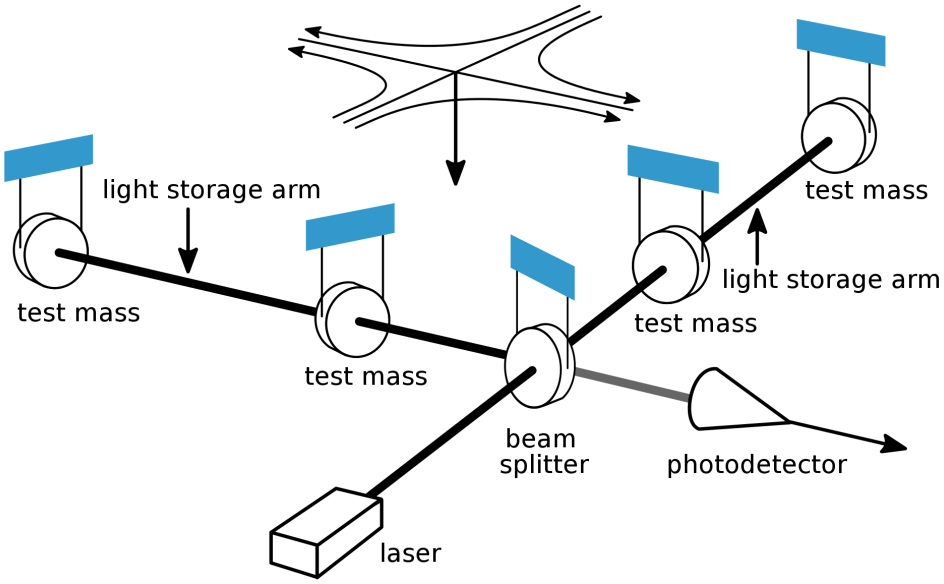

Figure 1.2: Schematic representation of a laser interferometer for GW observations. The laser emits light towards the beam splitter, which splits the beam in two. Both beams are then reflected between the mirrors, denoted as "test mass", before arriving back at the beam splitter. If no wave is passing through the observatory, the beams interfere destructively and no light is detected at the photodetector. ("LIGO" by MOBle is licensed under CC BY 2.0, following [Mayerson et al., 2019])

(see Sec. 1.3).

Aside from interferometers, pulsar timing arrays (PTAs) are also used nowadays to detect gravitational waves. The idea is to monitor a collection of pulsars, which serve as excellent cosmic clocks, and look for correlations in the arrival times of their pulses. We do not treat this further in this work, but the interested reader can consult a review like [Yunes and Siemens, 2013].

1.3 The LISA mission

The Laser Intereferometer Space Antenna (LISA) is the first space-based GW interferometer, set to launch in the mid 2030s. As explained in the previous section, current ground-based detectors have already detected many exciting events, but are not able to probe low-frequency GWs below 1-10 Hz: LISA is the proposed solution to this problem, and we provide a short overview in this section, largely based on [Amaro-Seoane et al., 2017].

LISA will scan a broad range of frequencies $f \sim 10^{-5} - 10^{-1}$ Hz, with peak sensitivity around 1 mHz. The observatory will consist of 3 identical spacecraft in a triangular formation, separated 2.5 million km and with 6 laser links between them, trailing Earth's orbit around the Sun. Each spacecraft will contain 2 freely falling test masses, that serve as end mirrors for different interferometer arms. A laser beam with a few Watts of power is emitted from each spacecraft, but due to beam divergence the received laser light has a

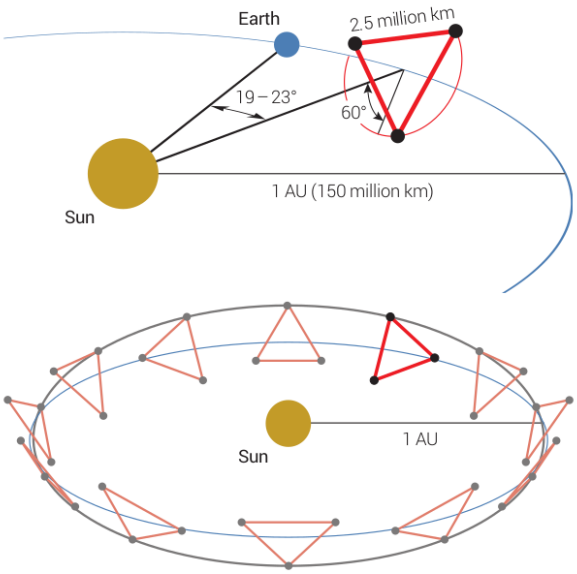

Figure 1.3: Depiction of the LISA orbit. [Amaro-Seoane et al., 2017]

decreased power on the order of some 100 pW. Therefore, the laser beam cannot simply be reflected as was the case for the ground-based detectors: instead, a fresh high-power beam is emitted, phase-locked to the incoming weak beam.

The technology behind the design was proven effective by the LISA Pathfinder mission: it is possible for a spacecraft to follow two encapsulated freely falling test masses, and to measure their relative positions. The combination of the three links resembles two interferometers that measure the two polarizations of the GW simultaneously, while a third *Sagnac* configuration is used to characterise the instrumental noise.

LISA will be located in a stable Earth-trailing heliocentric orbit, about 50 million km away from Earth (see Figure 1.3). Due to the orbit around the sun, the direction of the source can be reconstructed for signals that last at least several weeks. The nominal mission duration of LISA is 4 years, which can be extended up to 10 years.

LISA is designed with several science objectives in mind, listed in [Amaro-Seoane et al., 2017] as follows:

- **SO1:** Study the formation and evolution of compact binary stars in the Milky Way Galaxy.
- **SO2:** Trace the origin, growth and merger history of massive black holes across cosmic ages.
- **SO3:** Probe the dynamics of dense nuclear clusters using EMRIs.
- **SO4:** Understand the astrophysics of stellar origin black holes.
- **SO5:** Explore the fundamental nature of gravity and black holes.

- **SO6:** Probe the rate of expansion of the Universe.
- **SO7:** Understand stochastic GW backgrounds and their implications for the early Universe and TeV-scale particle physics.
- **SO8:** Search for GW bursts and unforeseen sources.

In this thesis, we will mainly focus on SO2 and SO7.

It is believed that most massive galaxies harbor a SMBH in their center. These black holes can have masses in the range $\sim 10^5 - 10^9 M_\odot$, and can be observed e.g. through violent accretion processes that radiate electromagnetic radiation. It is however unclear how they are formed. In particular, observations show that SMBHs at the upper end of this mass range already formed before the Universe was 1 Gyr old [Wang et al., 2021]. Therefore, if these SMBHs are formed hierarchically, many of their seeds must be present at early times. These seeds could form as the result of collapsing population-III stars, dense gas clouds, very compact clusters, or originate from primordial BHs [Volonteri, 2010]. These seeds would then grow through mergers and accretion, but the redshifts at which these mergers happen are too large for our ground-based interferometers to detect them.
LISA is hoped to see some of these seed black holes at large redshifts: it is designed to have the capability of detecting the inspiral of massive BHs between $10^3 M_\odot$ and $10^5 M_\odot$, at formation redshifts between 10 and 15. At lower redshifts ($z \lesssim 9$), it should detect coalescing BHs with masses on the order of $10^4 - 10^6 M_\odot$.

With respect to SO7, one of the main LISA goals is the direct detection of a stochastic gravitational-wave background (GWB). Different types of backgrounds exist (see Sec. 2.1), but its origin is encoded in its frequency dependence. The aim is to detect the GWB from coalescing binaries, for which upper limits exist based on LIGO data (Sec. 2.2). Furthermore, LISA is also designed to measure or set limits on any background of cosmological origin. The detection and characterization of such a background can lead to improved detections of individual resolved events.

1.4 Motivation and research objectives

The LISA Science Objectives that were layed out in the previous section underline the enormous amount of science that can be done once the detector is up and running. All these topics are still active fields of research, and this thesis aims to shed additional light on two of the science objectives.

On the one hand, Chapter 2 investigates the GWB generated by extragalactic WD binaries. SO7 revolves around the hope of detecting the GWB generated by inspiralling compact binaries, which remains undetected in the frequency band of ground-based detectors. A lot of work is done on the background generated by BH binaries, which is expected to dominate over that of the NS binaries. Upper limits on this background have been produced by [LIGO Scientific Collaboration, Virgo Collaboration, and KAGRA Collaboration et al., 2021], which we revisit in Sec. 2.2. However, we revisit earlier work by [Farmer and Phinney, 2003] in Sec. 2.3.1, in which predictions are made for

the background that arises from extragalactic WD binaries. We compare their estimates to the LVK results in Sec. 2.3.2, and note that they suggest that the WD background dominates in the LISA band. As all three components are present in this frequency band, the detector will only measure the sum of the different contributions. In theory, all these components exhibit the same frequency dependence, and therefore the question is wheter they can be disentangled. If the answer to this question is negative, the prospects of drawing conclusions for one of the components are grim. We model the WD background in Sec. 2.4 and 2.5, in which we provide our own predictions for the amplitude and investigate whether the WD contribution can be disentangled.

On the other hand, we work in the context of SO2, focusing on merging SMBHs. When two SMBHs merge, the remnant receives a recoil kick to conserve the momentum that is carried away by gravitational radiation. If this merger takes place in a star-dense region - like the center of a galaxy - stars that are strongly bound remain bound. This leads to a dense cluster that is ejected from the core of the galaxy, with the remnant SMBH in the center: a hypercompact stellar cluster (HCSC). These systems have not been observed yet, even though studies [Merritt et al., 2009, O'Leary and Loeb, 2012] predict that hundreds of these systems should be detectable with present-day telescopes. These systems would provide information about the merger event, as the kick velocity depends on the binary parameters. It turns out that this kick velocity is encoded in the observed velocity dispersion of HCSCs, and therefore observations of these systems would help determine the GW kick distribution, which in its turn constrains the merger history of SMBHs. Furthermore, the detection of a HCSC would also provide direct proof that SMBHs actually merge, which is one of the major assumptions underlying the LISA mission.

However, current predictions for the size of these clusters assume that, in addition to the central SMBH, the only members of such a HCSC are stars. In Chapter 3 we add a stellar-mass black hole (smBH) population to the cluster, and show that it can significantly increase the size of the cluster. We present a summary of the literature in Sec. 3.1 and 3.2.1, after which we motivate the addition of the smBH component in Sec. 3.2.2. We review the results of earlier simulations in 3.3, and present the models and Fokker-Planck code that we use in Sec. 3.3.3. We then discuss some general results in Sec. 3.4, and apply them to model two observational candidates in Sec. 3.5.

We finish by summarizing our conclusions in Chapter 4, where we also present future prospects for research related to this work.

Chapter 2

The Stochastic GW Background from Extragalactic WD Binaries

The first science objective that we want to address further is SO7, as described in 1.3: *"Understand stochastic gravitational-wave backgrounds and their implications [...]"*. We start with the general theory on GWBs in Sec. 2.1, in which we focus mainly on the background generated by coalescing compact binaries. In Sec. 2.2 we present the most recent observational constraints on GWBs, as determined by ground-based detectors. Subsequently, we focus on the predicted GWB generated by extragalactic WD binaries in Sec. 2.3.1, and compare this to the predictions for the BH and NS backgrounds in the remainder of Sec. 2.3. We point out[1] that the background from WD binaries is likely the dominant one in the LISA frequency band.
The remainder of this chapter aims to study and model this GWB. Sec. 2.4 presents a first approach that normalizes the final result to the predictions of 2.3.1, but investigates the influence of the WD population and redshift distribution by examining toy models. Finally, Sec. 2.5 presents the results of a more elaborate model, in which we do not normalize the final result and make our own prediction for the amplitude of the background. We also use this model to investigate the influence of the cosmic star-formation history (SFH) in Sec. 2.5.4. The cosmological parameters used throughout the Chapter are the Planck 2018 results [Planck Collaboration et al., 2020], and calculations are done with the `astropy` module in Python.

2.1 Gravitational-wave backgrounds

An astrophysical GWB is the collection of all GWs generated by astrophysical processes that are individually unresolved by the detectors. The background of interest for this research is that generated by a collection of inspiralling and merging binary systems. There is good reason to look for such a background, as it can teach us a lot about the merger rate as a function of redshift, thus constraining formation models for these binaries. We study this GWB in Sec. 2.1.1, and briefly comment on other types of backgrounds in Sec. 2.1.2.

[1] We are not the first ones to notice this, but generally speaking this seems to be forgotten.

2.1.1 Coalescing compact objects

Depending on the type of compact object, the signal will be observable in a certain frequency regime. Indeed, Kepler's third law tells us that the orbital separation of a binary a is linked to its orbital frequency ν and the component masses:

$$a^3\nu^2 = \frac{G(M_1 + M_2)}{4\pi^2}\,. \tag{2.1}$$

The frequency of the emitted GW, which we will denote as f, is twice the orbital frequency: $f = 2\nu$. So, depending on the masses and type of compact object, there is a minimal orbital separation (before merger) resulting in a maximal GW frequency. As the ground-based GW detectors operate in the high-frequency regime, they can only observe the final inspiral phase of binary smBHs, binary NSs or BH-NS binaries. Binaries consisting of more massive black holes, stars or white dwarves are not seen by these detectors, as they merge before they enter the required frequency regime. LISA, however, may be able to observe these binaries, depending on the amplitude of the signal.

Evidently, we expect that the gravitational-wave sky is dominated by sources in our own Milky Way, as they are nearby. This project is concerned with the stochastic background from *extragalactic* sources, which may a priori seem hard to detect given the dominant signal from the local sources. However, the galactic sources are expected to be anisotropically distributed with most of the sources located in the galactic disk. As LISA will monitor the entire sky, the detector beam pattern will rotate. This leads to the galactic signal being modulated, such that it can eventually be extracted from the measurements and separated from the extragalactic component [Adams and Cornish, 2014].

Theoretical derivation

We start by deriving the expected GWB produced by a population of compact binaries in the adiabatic inspiral phase, following [Phinney, 2001, Renzini et al., 2022]. The binary is characterized by the masses M_1, M_2, and we assume that Kepler's third law holds and that the orbits are circular[2]. Furthermore, we assume that the binary merges due to GW loss on a timescale much shorter than the age of the Universe. The reason is that we can then assume that all of the inspiral occurs at the same redshift as the merger. In general, this is a good approximation, since the frequency evolution of the binary depends strongly on the frequency, such that in general binaries either merge quickly or not at all. Indeed, it turns out that the orbital frequency ν of the binary evolves as [Farmer and Phinney, 2003]

$$\dot{\nu} = K\nu^{11/3}\,, \tag{2.2}$$

where K is a constant depending on the chirp mass

$$\mathcal{M} = \frac{(M_1 M_2)^{3/5}}{(M_1 + M_2)^{1/5}} \tag{2.3}$$

[2]This assumption is reasonable, since generally speaking the binary circularizes. [Farmer and Phinney, 2003] also considers eccentricity for the orbits, which leads to emission at all harmonics n of the orbital frequency, with $f_n = n\nu$.

of the binary:

$$K = \frac{96}{5}(2\pi)^{8/3}\left(\frac{G\mathcal{M}}{c^3}\right)^{5/3} \approx 3.7\cdot 10^{-6}\left(\frac{\mathcal{M}}{M_\odot}\right)^{5/3}\ \mathrm{s}^{5/3}\,. \tag{2.4}$$

This allows us to derive that a single binary, born at time t_0, obeys

$$\nu(t)^{-8/3} - \nu_0^{-8/3} = 8K(t_0 - t)/3\,, \tag{2.5}$$

where ν_0 is the frequency at birth, at time t_0.

We focus on the dimensionless energy density spectrum

$$\Omega_{\mathrm{GW}}(f_r) = \frac{1}{\rho_c c^2}\frac{\mathrm{d}\mathcal{E}_{\mathrm{GW}}}{\mathrm{d}\ln f_r}\,, \tag{2.6}$$

where f_r is the received GW frequency, and $\rho_c = \frac{3H_0^2}{8\pi G}$ is the critical density for a closed Universe. We will focus on isotropic backgrounds here, but it is possible to include anisotropy by adding a dependency on the line of sight $\mathbf{n}$ (see (2.16)). First, we define the GW frequency in the rest frame of the emitter f_e, which is related to the measured frequency f_r as $f_e = f_r(1+z)$ due to cosmic redshift.

In an isotropic and homogeneous Universe, the present-day energy density is equal to

$$\begin{aligned}\mathcal{E}_{\mathrm{GW}} &= \int_0^\infty \mathrm{d}f_e \int_0^\infty \mathrm{d}z N(z)\frac{1}{1+z}\frac{\mathrm{d}E_{\mathrm{GW}}}{\mathrm{d}f_e}\\ &= \int_0^\infty \frac{\mathrm{d}f_r}{f_r} f_r \int_0^\infty \mathrm{d}z N(z)\frac{\mathrm{d}E_{\mathrm{GW}}}{\mathrm{d}f_e}\,,\end{aligned} \tag{2.7}$$

where $N(z)$ is the number density of emitters at redshift z, and $\frac{\mathrm{d}E_{\mathrm{GW}}}{\mathrm{d}f_e}$ is the energy spectrum of the source measured in its own rest frame , such that we included a factor $(1+z)$ to account for the redshift. Therefore, we must have that

$$\Omega_{\mathrm{GW}}(f_r) = \frac{f_r}{\rho_c c^2}\int_0^\infty \mathrm{d}z N(z)\frac{\mathrm{d}E_{\mathrm{GW}}}{\mathrm{d}f_e}\,. \tag{2.8}$$

We allow for variation in the source population by averaging over the source population parameters

$$\left\langle N(z)\frac{\mathrm{d}E_{\mathrm{GW}}}{\mathrm{d}f_e}\right\rangle = \int \mathrm{d}\theta p(\theta) N(z;\theta)\frac{\mathrm{d}E_{\mathrm{GW}}(\theta)}{\mathrm{d}f_e} \tag{2.9}$$

to find that

$$\Omega_{\mathrm{GW}}(f_r) = \frac{f_r}{\rho_c c^2}\int_0^\infty \mathrm{d}z \left\langle N\frac{\mathrm{d}E_{\mathrm{GW}}}{\mathrm{d}f_e}\right\rangle\,. \tag{2.10}$$

We can approximate the emitted GW radiation by the leading quadrupole order [Hawking and Israel, 1989]

$$\frac{\mathrm{d}E_{\mathrm{GW}}}{\mathrm{d}f_e} = \frac{\pi^{2/3}}{3}G^{2/3}\mathcal{M}^{5/3}f_e^{-1/3} \qquad \text{for } f_{\min} < f_e < f_{\max}\,. \tag{2.11}$$

The limiting frequencies depend on the source properties. The lower limit $f_{\min}$ is set by the separation of the system after circularisation, and is such that the final merger is smaller than the Hubble time. The frequency at which the source emits increases over time, until the binary components come into Roche lobe contact, or the evolution becomes dominated by tidal forces. This sets a minimal orbital separation, and therefore a maximal frequency for the binary. As an example, for 2 white dwarfs of $0.3M_{\odot}$ we need $f_{\min} > 10^{-4}$ Hz in order to merge in less than 10^{10} yr, whereas $f_{\max} \approx 0.01$ Hz. A pair of neutron stars, however, has $f_{\max} \approx 1.4 \cdot 10^{3}$ Hz. [Phinney, 2001]

The co-moving number density can be rewritten as an integral over $\mathcal{M}$

$$N(z) = \int_{\mathcal{M}_{\min}}^{\mathcal{M}_{\max}} \frac{\mathrm{d}N}{\mathrm{d}\mathcal{M}} \mathrm{d}\mathcal{M} \tag{2.12}$$

to find

$$\Omega_{\mathrm{GW}}^{\mathrm{CB}}(f_r) = \frac{(\pi G)^{2/3}}{3\rho_c} f_r^{2/3} \int_0^{\infty} \mathrm{d}z \frac{1}{(1+z)^{1/3}} \int_{\mathcal{M}_{\min}}^{\mathcal{M}_{\max}} \mathrm{d}\mathcal{M} \frac{\mathrm{d}N}{\mathrm{d}\mathcal{M}} \mathcal{M}^{5/3} \,. \tag{2.13}$$

It should be noted that the limiting frequencies may depend on the chirp mass (e.g. the size of the Roche lobe changes), such that it may not be completely correct to sum over all the different chirp masses and keep this exact frequency dependence. In the case of a single chirp mass, however, the integral over $\mathcal{M}$ becomes trivial to find that

$$\Omega_{\mathrm{GW}}^{\mathrm{CB}}(f_r) \propto f_r^{2/3} \mathcal{M}^{5/3} \,. \tag{2.14}$$

We will often use this result in the form

$$\Omega\left(f\right) = \Omega\left(f_{\mathrm{ref}}\right) \left(\frac{f}{f_{\mathrm{ref}}}\right)^{2/3} , \tag{2.15}$$

where f_{ref} is a reference frequency at which we can estimate / measure the GWB.

The main result is that the GWB from coalescing binaries is expected to scale as $\Omega \propto f^{2/3}$, and is independent of the details of the cosmology, other than the assumption of homogeneity and isotropy. Furthermore, it only depends on the source characteristics through the distribution in redshift and chirp mass, and the limiting frequencies.

However, in practice the frequency dependence of the GWB can differ from (2.15). One of the approximations we made is that the entire merger process happens at one specific redshift, which is not exact. Secondly, if there is a distribution in chirp mass, the $f^{2/3}$ behaviour only holds at frequencies at which all the binaries can emit. For frequencies above the maximal frequency for some of the binaries, the increase in Ω will be less steep, as some of the systems do not contribute anymore.

If new sources are being injected, [Farmer and Phinney, 2003] show that $\Omega \propto f^{10/3}\mathcal{M}^{10/3}$ for $f \lesssim f_{\min}$, under the assumption that the binaries are distributed roughly uniform in $\log \nu$ at their birth. Recall that $f_{\min}$ was defined as the minimum birth frequency of a binary such that it merges in less than a Hubble time, and that the strong frequency dependence of (2.2) means that binaries either remain at an approximate constant frequency, or merge quickly. Therefore, we will refer to $f \gtrsim f_{\min}$ ($\Omega \propto f^{2/3}$) as the *spiral-in* regime, and to $f \lesssim f_{\min}$ ($\Omega \propto f^{10/3}$) as the *static* regime.

2.1.2 Other backgrounds

In the previous section, we have considered an isotropic background. It is however possible to relax that assumption, and consider anisotropic GWBs. The reason for the anisotropy can be that the sources follow a particular distribution on the sky, or line-of-sight effects due to small anisotropies in the matter density through which the waves propagate. The fractional GW density is then redefined per solid angle

$$\Omega(f, \mathbf{n}) = \frac{1}{\rho_c c^2} \frac{\mathrm{d}\mathcal{E}_{\mathrm{GW}}}{\mathrm{d}\ln f \, \mathrm{d}\mathbf{n}} \,. \tag{2.16}$$

This anisotropic GWB has been looked for as well, but without success so far [LIGO Scientific Collaboration, Virgo Collaboration, and KAGRA Collaboration and others, 2021].

The frequency dependence (2.15) is a particular example of a power-law GWB

$$\Omega\left(f\right) = \Omega\left(f_{\mathrm{ref}}\right) \left(\frac{f}{f_{\mathrm{ref}}}\right)^{\alpha} \,, \tag{2.17}$$

where $\alpha = \frac{2}{3}$. There are other proposed backgrounds with more exotic origin that also exhibit a power-law dependence on the frequency [Renzini et al., 2022]. A noteworthy example is a GWB that arises as a byproduct of inflation, which should be approximately frequency-independent ($\alpha = 0$) above $\sim 10^{-18}$ Hz. Such a background should have left imprints on the cosmological microwave background, which astrophysicists can look for [Kamionkowski et al., 1997]. Other examples of cosmological backgrounds include those due to phase transitions and cosmic strings. There are other astrophysical sources that can produce a background as well, like supernovae, that can give rise to a background for which $\alpha = 3$, and rotating neutron stars [Regimbau, 2011]. An illustration of possible backgrounds across the frequency spectrum is given in Figure 2.1.

2.2 Upper limits from LVK

In this section we summarize the current constraints on stochastic GWBs, as obtained by the LVK collaboration[3]. The first three observing runs of Advanced LIGO and Advanced Virgo have lead to a total of 90 observed GW events [Abbott et al., 2021]. Scientists have looked for an isotropic stochastic GWB in the data, but no evidence has been found so far. They were able to place upper limits on the GWB however, which will be used in Sec. 2.3.2.

Importantly, the ground-based interferometers observe in the frequency range $f \sim 10 - 10^3$ Hz, in which we don't expect to observe WD binaries, as the required orbital separation is too small for a WD binary to emit at this frequency. Therefore, only smBHs and NSs are expected to contribute to a background from coalescing compact binaries.

[3] I was informed by Hannah Duval that in the foreseeable future results should be published that are obtained with PTAs, which may or may not have detected some background signal. The principles behind these detections can be found in e.g. [Allen and Romano, 2022, DeRocco and Dror, 2023, Jenet and Romano, 2014]. I thank Hannah for pointing this out to me

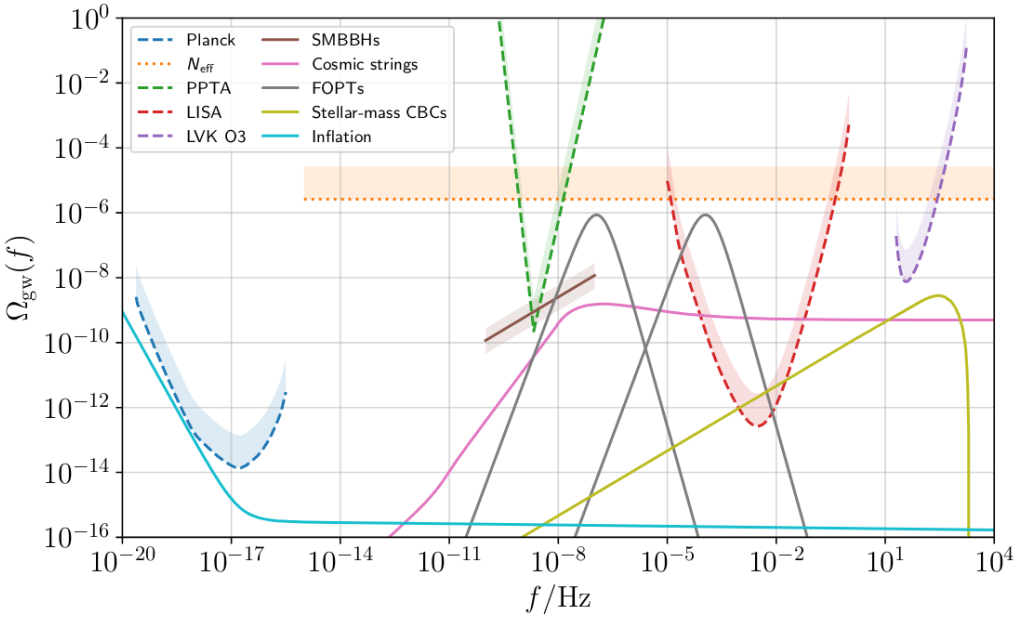

Figure 2.1: An overview of potential GWB signals across the frequency spectrum. FOPT refers to a first-order phase transition, and a full description of all these sources is given in [Renzini et al., 2022]. The dashed curves show the sensitvities of various experiments. This is Figure 1 in [Renzini et al., 2022]

Searches for a GWB have employed a cross-correlation search, in which the data in frequency is compared to the expected power-law dependence of the energy density. The current upper limit at the 95% confidence level is [LIGO Scientific Collaboration, Virgo Collaboration, and KAGRA Collaboration et al., 2021]

$$\Omega_{\rm GW}(25\ {\rm Hz}) \leq 3.4 \cdot 10^{-9}\,. \tag{2.18}$$

Combining this upper limit with the established detections[4] in GWTC2, estimates can be made for the GWB for binaries consisting of BHs or NSs. These estimates are [LIGO Scientific Collaboration, Virgo Collaboration, and KAGRA Collaboration et al., 2021]

$$\Omega_{\rm BH}(25\ {\rm Hz}) = 4.7^{+1.6}_{-1.4} \cdot 10^{-10}\,, \tag{2.19}$$
$$\Omega_{\rm NS}(25\ {\rm Hz}) = 2.0^{+3.2}_{-1.4} \cdot 10^{-10}\,, \tag{2.20}$$

Using (2.15), we can extrapolate these estimates into the frequency range in which LISA will operate. We take $f_{\rm ref} = 25$ Hz, and the estimates above. The reason that we can extrapolate the estimates in this way, is that that $f_{\rm min}$ is lower for BHs and NSs than it is for white dwarfs (see Table 2.1). Therefore, we expect the $\Omega \propto f^{2/3}$ behaviour to

[4]It should be noted that, in a more recent arXiv preprint [Collaboration et al., 2022] updated values for these estimates are given. They are based on GWTC3 [Abbott et al., 2021], and therefore also include an estimate for BH-NS mergers. These more recent estimates are $\Omega_{\rm BH}(25\ {\rm Hz}) = 5.0^{+1.4}_{-1.8} \cdot 10^{-10}, \Omega_{\rm NS}(25\ {\rm Hz}) = 0.6^{+1.7}_{-0.5} \cdot 10^{-10}, \Omega_{\rm BHNS}(25\ {\rm Hz}) = 0.9^{+2.2}_{-0.7} \cdot 10^{-10}$. The combination of the latter two is comparable to what we used now for the NS background, and subdominant to the BH contribution anyway. For the sake of time until the deadline, the figures in this Chapter are not updated to display these new values, as the conclusions would not be altered. In what follows, we thus use the values given in the text.

extend until below 10^{-4} Hz, which was an estimate for $f_{\min}$ in the case of WDs. These extrapolations can be seen in Figure 2.3.

2.3 Extragalactic white dwarf binaries in the LISA band

Given the constraints and estimates provided in the previous section, we now turn to the GWB originating from extragalactic WD binaries. These systems only emit below $\lesssim 0.1$ Hz, and are therefore not detectable by ground-based detectors. We revisit the study [Farmer and Phinney, 2003] that modelled this background and summarize their findings in Sec. 2.3.1. Afterwards, we extrapolate the observational constraints from the LIGO band to the LISA band, and argue that the predicted GWB from binary WDs likely dominates over the other components in Sec. 2.3.2.

2.3.1 Model for the GWB

The authors of [Farmer and Phinney, 2003] modelled the GWB due to extragalactic close binaries descending from low to intermediate-mass stars. The resulting energy density is shown in Figure 2.2, for the interval 10^{-6} Hz $< f < 0.1$ Hz. To obtain these results, the authors used a population synthesis code[5], keeping track of the different types of binaries that can contribute to the background. For example, they also keep track of main-sequence (MS) stars and naked helium stars (nHe), and determine their contribution to the background as well.

The thin solid line in Figure 2.2 is due to binary WDs, and dominates the GWB above 10^{-4} Hz. It displays the spectral shape derived in the Sec. (2.1.1), where the transition between the static and spiral-in regimes happens around 10^{-4} Hz. The slope above this frequency is slightly steeper than 2/3, which is due to the spectrum being a sum of different spectra with varying chirp masses. Around 0.01 Hz, the spectrum displays a peak: above this frequency, many binaries merge, which leads to the subsequent decline.

In first instance, we approximate this simulated GWB with a $\Omega \propto f^{2/3}$ background between 10^{-4} Hz and 10^{-2} Hz, through (2.15). To this end, we use the estimate[6] $\Omega_{\rm WD}\,(1\text{ mHz}) = 3.57\cdot 10^{-12}$, obtained in [Farmer and Phinney, 2003] as model A. This is a good approximation to the simulation results, though slightly overestimating the background around 10^{-4} Hz. The resulting approximated GWB is plotted in Figure 2.3. The shaded green region around this estimate corresponds to the uncertainty $1\cdot 10^{-12} \lesssim \Omega_{\rm BWD}(1\text{ mHz}) \lesssim 6\cdot 10^{-12}$, derived by the same authors.

[5] We follow a similar method in Sec. 2.5.

[6] It should be noted that $\sim 10\%$ of this amplitude is due to nHe-WD pairs. Even though these are strictly speaking not WD binaries, we keep their contribution when comparing to the BH and NS components in Sec. 2.3.2.

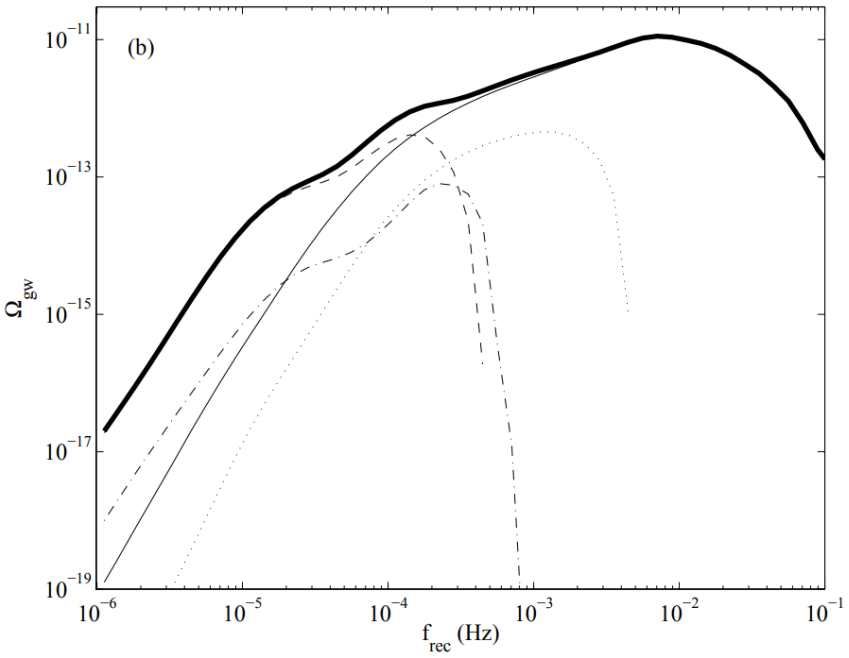

Figure 2.2: The GWB for model A in [Farmer and Phinney, 2003], described by the dimensionless energy density (2.6) as function of the observed GW frequency. Solid line: WD-WD pairs; dotted line: nHe-WD pairs; dashed line: MS-MS binaries, and dot-dash line: WD-MS binaries. The total signal (the sum of all components) is given by the thick solid line.

2.3.2 Relative amplitudes

Interestingly, the general consensus in the community is that the GWB from extragalactic WD binaries will not be detectable by LISA [Boileau et al., 2022, Flauger et al., 2021, Renzini et al., 2022]. The expectation is that, if LISA is able to measure a stochastic GWB with the correct frequency dependence[7], it will be produced by smBHs and NSs. In this section we revisit this consensus, by comparing the simulation results from the previous section against the estimates from Sec. 2.2, which we extrapolate to the LISA band. The result can be seen in Figure 2.3, showing that the WD background is likely to dominate. We investigate this prediction in more detail in the following sections.

Figure 2.3 shows that the GWB extrapolated[8] from the current upper limit is almost coincident with the predicted WD background[9]. This means that, even if the GWB in the LVK frequency band is equal to the current upper limit, the background from WD binaries is of equal importance as the one generated by BHs and NSs. However, if we base ourselves on the current best estimates, the WD background is seen to be the dominant one. This means that, should LISA detect a GWB originating from coalescing compact binaries (i.e. with the dependence (2.15)), it will likely be dominated by the signal from WD binaries. Such a detection is certainly possible: Figure 2.3 also shows the approxi-

[7]Potentially, LISA will also detect other cosmological backgrounds, like the ones discussed in 2.1.2.

[8]Recall the discussion from 2.2. We can expect the BH and NS background to closely follow the predicted $f^{2/3}$ shape, meaning that the extrapolation using (2.15) should be fairly accurate.

[9]An updated version of this Figure is given in Appendix B.1, as Figure B.1. See footnote 4

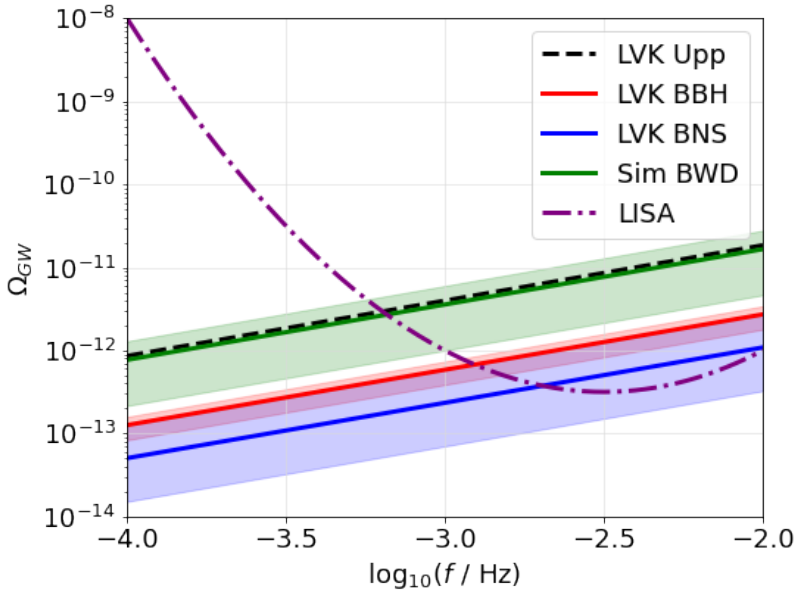

Figure 2.3: Comparison of the different components that make up the GWB due to coalescing compact binaries, described by (2.15). The dashed black line describes the extrapolated upper limit on the background as derived in [LIGO Scientific Collaboration, Virgo Collaboration, and KAGRA Collaboration et al., 2021]. The solid lines and shaded regions are the estimates for the backgrounds generated by binary WDs, BHs and NSs [Farmer and Phinney, 2003, LIGO Scientific Collaboration, Virgo Collaboration, and KAGRA Collaboration et al., 2021]. The dot-dash line is a parabola that approximates the sensity curve of the planned LISA mission, for comparison.

mate LISA sensitivity curve[10].

This claim is backed up by a comparable conclusion in [Schneider et al., 2001], where the extragalactic GWB is calculated for binary WDs, BHs, NSs and mixtures. They also conclude that the extragalactic signal is dominated by WDs, with the runner-up being NS-WD binaries. However, they estimated the signal to be larger, but their method is critically analysed in [Farmer and Phinney, 2003] and arguments are given for the improved estimate of the latter. Subsequently, their study was backed up by an improved estimate for the extragalactic NS-WD background as well [Cooray, 2004], which again was lower than the estimate for WDs, thus preserving the hierarchy orginally found in [Schneider et al., 2001].

A more recent study [Liang et al., 2022] also shows evidence for the dominant contribution of binary WDs. Here, scientists working around the planned TianQin detector (a project similar to LISA) discuss the prospects of detecting a GWB in the low-frequency band. To this end, they based themselves on [Rosado, 2011], from which they extracted estimates

[10]All the figures in this chapter show a parabolic approximation to the LISA sensitivity curve, based on Figure 7 in [Renzini et al., 2022]. The purpose of this sensitivity curve is purely illustrative, in order to have a rough idea of the detection capabilities of LISA. Therefore, a more advanced implementation is not necessary.

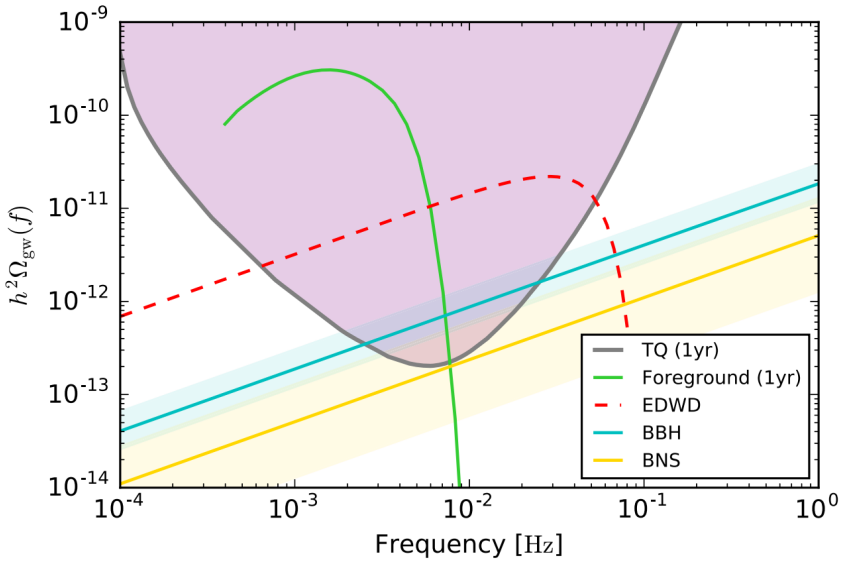

Figure 2.4: Comparison of different gravitational-wave backgrounds based on [Rosado, 2011]. The foreground is due to Galactic WD binaries, EDWD corresponds to extragalactic WD binaries and BBH and BNS to binary BHs and NSs, respectively. The gray curve is the sensitivity curve for the TianQin observatory with 1 year operation time. Figure taken from [Liang et al., 2022].

for the background produced by different compact objects. Their results are shown in Figure 2.4, and lead to similar conclusions as we draw here. Furthermore, this study also acknowledges the background from [Farmer and Phinney, 2003], which leads them to believe that the WD background dominates as well.

An order-of-magnitude argument

We now give another argument to estimate the relative amplitudes from the different GWB components, to further motivate the dominant contribution of WDs. Observations help us estimate the current merger rate R (in the entire Universe), for which order-of-magnitude estimates[11] can be found in Table 2.1. In the same table, we give a typical value for the chirp mass of the different compact binaries. Furthermore, we can determine the merger time at frequency f (i.e. the time until merger for a binary with orbital frequency $\nu = f/2$) from (2.5):

$$\begin{aligned} \nu^{-8/3} &\approx \frac{8K}{3} t_m(\nu) \\ \Leftrightarrow t_m(f) &\approx \frac{3}{8K}\left(\frac{f}{2}\right)^{-8/3} . \end{aligned} \tag{2.21}$$

Setting this merger time to 10 Gyr, and taking the typical values for the chirp mass in Table 2.1 gives us the estimates for $f_{\rm min}$ that can be found in the same table. The merger

[11] We take representative values from [Collaboration et al., 2021, 2022] for the BH and NS merger rates, and use that the present volume of the Universe is on the order of $\sim 1.2 \cdot 10^4$ Gpc^3 (calculated with `astropy`). The WD merger rate in the Milky Way is calculated in [Nelemans et al., 2001]. They find $2.2 \cdot 10^{-2}$ yr^{-1}, for which we can make a rough extrapolation by using that the observable Universe contains $\sim 10^{10} - 10^{11}$ galaxies [Conselice et al., 2016, Lauer et al., 2021].

Table 2.1: Order-of-magnitude estimate for the merger rate and typical value for the chirp mass, for three different compact binaries. For each of these chirp masses, the minimum GW frequency in order to merge within 10 Gyr is given as well. Based on [Collaboration et al., 2021, Nelemans et al., 2001]

Binary	Merger rate [yr^{-1}]	chirp mass $\mathcal{M}$ [$M_\odot$]	$f_{\min}$ [Hz]
Black holes	$2.8 \cdot 10^5$	20	$2.7 \cdot 10^{-6}$
Neutron stars	$1.3 \cdot 10^6$	1.2	$1.6 \cdot 10^{-5}$
White dwarfs	$10^8 - 10^9$	0.5	$2.7 \cdot 10^{-5}$

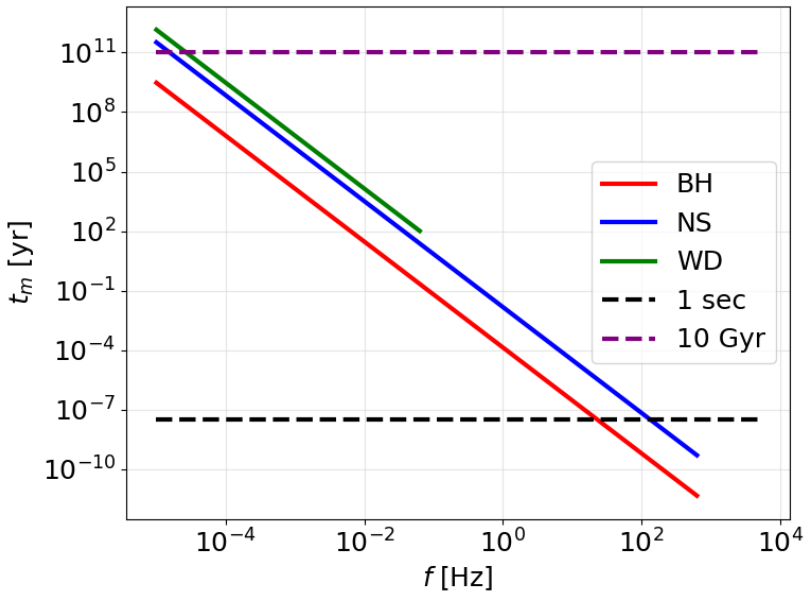

Figure 2.5: Merger time as a function of GW frequency for the three different types of compact binaries. Typical values for the chirp mass are taken from Table 2.1.

time as function of the GW frequency is plotted in Figure 2.5. Note that the expression (2.21) is an approximation, which breaks down at frequencies close to the merger frequency. Therefore, the results in Figure 2.5 (and Figure 2.6) should be considered as only correct at frequencies much smaller than the merger frequency.

We now argue that

$$N(f) \propto R\, t_m(f)/f \propto R\mathcal{M}^{-5/3} f^{-11/3}\,. \tag{2.22}$$

Indeed, this is most easily seen if we reverse the flow of time. Suppose binaries are created at a birth rate R, all with the same orbital frequency ν_m (i.e. the frequency at which the binary normally would merge). These systems evolve towards lower frequencies, according to the time-reversed (2.5). The amount of time for a system to evolve to frequency ν_0 is equal to $t_m(\nu_0)$. This means that there are $t_m(\nu_0) \cdot R$ binaries between frequency ν_0 and ν_m, all created in the timespan $t_m(\nu_0)$. Reversing the flow of time does not change the number of systems, meaning that there are $t_m(\nu_0) \cdot R$ systems that will merge within the

same timespan. If we now want the number of systems $N(f)$ at a certain frequency f, we find that this has to obey the proportionality (2.22) by taking the derivative.

The rate at which a binary loses orbital energy is given by[12] [Peters and Mathews, 1963]

$$L = \frac{32}{5}\frac{G^4}{c^5}\frac{(M_1 M_2)^2(M_1+M_2)}{a^5}\,. \tag{2.23}$$

Using Kepler's law, we find that this means that

$$L = \frac{32(4\pi^2)^{5/3}}{5}\frac{G^{7/3}}{c^5}\mathcal{M}^{10/3}\nu^{10/3}\,,$$

or in terms of dimensionless quantities

$$L = 2.2\cdot 10^{38}\left(\frac{\mathcal{M}}{M_\odot}\right)^{10/3}\left(\frac{\nu}{\mathrm{Hz}}\right)^{10/3}\ \mathrm{J\ s^{-1}}\,. \tag{2.24}$$

We will now use the equivalent definition [Farmer and Phinney, 2003]

$$\Omega(f_r) = \frac{1}{\rho_c c^3} f_r F_{f_r}\,, \tag{2.25}$$

where $F_{f_r} = \frac{\mathrm{d}F(f_r)}{\mathrm{d}f_r}$ is the specific flux received from an object with specific luminosity L_{f_e} at redshift z. It is given by

$$F_{f_r} = \frac{L_{f_e}}{4\pi d_L(z)^2}\left(\frac{\mathrm{d}f_e}{\mathrm{d}f_r}\right)\,, \tag{2.26}$$

where $d_L = (1+z)d_M$ is the luminosity distance to redshift z, and d_M is the proper motion distance. The specific luminosity is given by

$$L_{f_e} = L\,\delta(f_e - 2\nu)\,, \tag{2.27}$$

where the luminosity L is given by (2.24). For this argument, we assume that the redshift distribution for the different compact binaries is similar, such that we can neglect the factors depending on the redshift. Therefore, we find using $f = 2\nu$

$$\Omega \propto N(f,t) L\, f\, \delta(f_e - f) \propto R\,\mathcal{M}^{5/3} f^{2/3}\,. \tag{2.28}$$

The right-hand side of this result is plotted in Figure 2.6 for the different compact binaries. These results exhibit the expected $\Omega \propto f^{2/3}$ behaviour. Even though the absolute amplitudes are not taken into account here, the relative amplitudes give a good idea of the hierarchy. This indeed shows that the NS binaries probably give rise to the smallest contribution, whereas the WD binaries can compete with the BHs, depending on the merger rate. Therefore, it is not unthinkable that the GWB from WD binaries provides the dominant contribution.

[12] In this expression we neglect contributions of non-zero eccentricity, which is a good approximation as it turns out that binaries circularize in general.

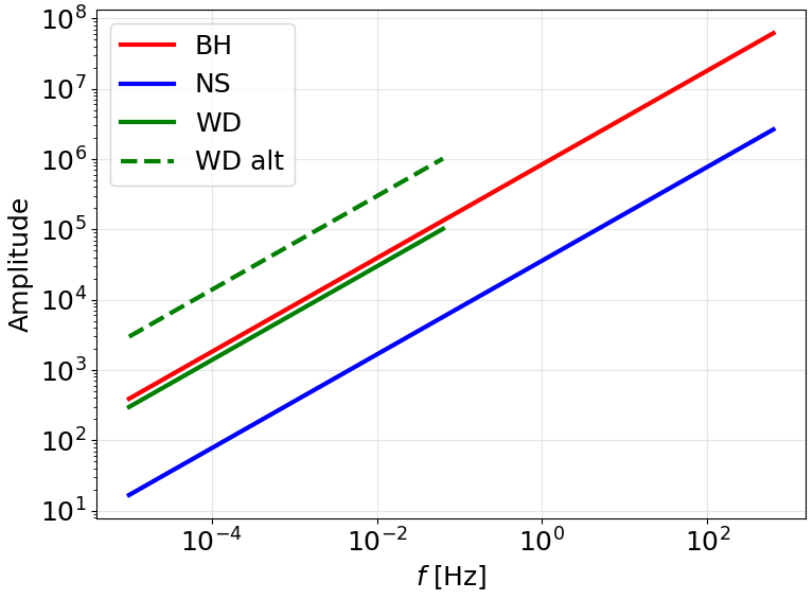

Figure 2.6: Order-of-magnitude estimates for the relative amplitude of Ω for the three different types of compact binaries. The lines are calculated based on the values in Table 2.1. The solid green line uses a merger rate for WD binaries equal to 10^8 yr^{-1}, and the dashed line uses 10^9 yr^{-1}.

2.4 The total background: a normalized approach

Motivated by the idea that binary WDs provide the dominant contribution to the GWB from coalescing compact binaries in the LISA frequency band, we now ask the following questions:

1. Does the WD contribution remain dominant if we change some of the parameters that go into the model?

2. Can we disentangle the different components that make up the total GWB sourced by compact coalescing binaries?

The first question has been partially investigated in [Farmer and Phinney, 2003] already, as they also considered alternative models and studied the resulting backgrounds. We will come back to their findings in Sec. 2.5, and look further into the influence of the cosmic star-formation history (SFH). The second question is an important one, as a negative answer implies that we cannot draw conclusions about one of the components, should we detect a background $\Omega \propto f^{2/3}$: in that case, we can only study the combined population of compact binaries. In the regime where all three components follow the $f^{2/3}$-behaviour exactly, they cannot be disentangled. Indeed, the amplitude is simply the sum of the amplitudes of the components.

However, this theoretical relation is not obeyed over the entire frequency range, as can be seen in Figure 2.2. Therefore, we first investigate whether the decay around 0.01 Hz and the transition to a steeper slope around 10^{-4} Hz fall within LISA detection limits. We employ a relatively simple construction of the background, which we normalize to the

value at 1 mHz found by [Farmer and Phinney, 2003], and investigate some toy models for the WD population and their redshift distribution. This helps us to get a better understanding of how these parameters influence the final result. Afterwards, we take a more sophisticated approach in Sec. 2.5, where we no longer renormalize the final result.

2.4.1 Construction of the background

In this first instance, we consider a collection of systems with given $\{\mathcal{M}, \nu_0, z\}$. For each of these systems, we can then calculate an $\Omega \propto f^{2/3}$ line from $2\nu_0$ up to some maximal frequency, and add all of these lines together to form the total background. It should be noted that this is an approximation to the actual background: systems with the same initial parameters, but currently emitting at a different frequency are formed at different times. Taking them all together in the $\Omega \propto f^{2/3}$ line implies that we assume a constant star-formation rate (SFR). Indeed, if the latter is not constant, the time of formation matters for the amplitude, and the background is not expected to follow the power-law behaviour exactly.

The maximal frequency is determined per system by taking the minimum of two limiting frequencies:

- On the one hand, we calculate $\nu_{\max,1}$ by solving (2.5) with $\Delta t = t - t_0$ set equal to the age of the Universe at redshift z. This equation does not have a solution when $\Delta t \gtrsim t_m(2\nu_0)$ as determined by (2.21). This limiting frequency thus arises from the requirement that the binary cannot have evolved for a time longer than the age of the Universe.

- On the other hand, we calculate $\nu_{\max,2}$ by using Kepler's law (2.1) for the minimum separation of the WD binary. This minimum separation is determined by the component masses and the mass-radius relation for WDs [Verbunt and Rappaport, 1988]

$$\frac{R}{R_\odot} = 0.0114 \left[\left(\frac{M}{M_{\rm ch}}\right)^{-2/3} - \left(\frac{M}{M_{\rm ch}}\right)^{2/3} \right]^{1/2} \times \left[1 + 3.5 \left(\frac{M}{M_{\rm p}}\right)^{-2/3} + \left(\frac{M}{M_{\rm p}}\right)^{-1} \right]^{-2/3} , \tag{2.29}$$

  where $M_{\rm ch} = 1.44 M_\odot$ is the Chandrasekhar mass and $M_{\rm p} = 0.00057 M_\odot$ is a constant. Furthermore, we also need the formula [Eggleton, 1983]

$$a_{\min} = \frac{R_1}{0.49} \left(0.6 + q^{2/3} \log\left(1 + q^{-1/3}\right)\right) \tag{2.30}$$

  for the minimal orbital separation before the onset of Roche-lobe overflow. In this expression, $q = M_2/M_1$, and we assume $q < 1$.

If we now receive a flux from a large number of systems, spread throughout the Universe, we can add all these contributions by introducing the specific luminosity density l_{f_e}, defined as $\mathrm{d}L_{f_e}(z) = l_{f_e}(z)\mathrm{d}V(z)$. The quantity l_{f_e} has units of J s^{-1} Hz^{-1} Mpc^{-3}, and $\mathrm{d}V(z)$ is the comoving volume element at redshift z. Using that $\mathrm{d}V(z) = 4\pi d_M(z)^2 \mathrm{d}\chi$, with $\chi(z)$ the proper motion distance, the specfic flux (2.26) is rewritten as

$$F_{f_r} = \int_{z=0}^{\infty} \frac{l_{f_e}(z)}{(1+z)^2} \left(\frac{\mathrm{d}f_e}{\mathrm{d}f_r}\right) \mathrm{d}\chi(z) \,, \tag{2.31}$$

We can discretize this integral over z, to find that

$$\Omega(f_r) \propto \sum_i \frac{1}{(1+z_i)^{4/3}} \mathcal{M}^{5/3} f_r^{2/3} \delta(f - (1+z) f_r) \Delta\chi(z_i) \,. \tag{2.32}$$

for a suitable set of $\{z_i\}$. So, the relative contribution to the total background of a binary at redshift z with chirp mass $\mathcal{M}$ is determined by the weight

$$w(\mathcal{M}, z) = \frac{1}{(1+z_i)^{4/3}} \mathcal{M}^{5/3} \Delta\chi(z_i) \,. \tag{2.33}$$

Once all the lines are added with their respective weight, the result is renormalized such that $\Omega(1 \text{ mHz}) = 3.57 \cdot 10^{-12}$. In practice, we will restrict to $z \leq 8$. We do so, as the SFR that we use in Sec. 2.5 is determined up to $z = 8$. Furthermore, we show in Sec. 2.5.3 that contributions from higher redshifts are negligible anyway.

2.4.2 Influence of the population

We start by considering some toy models for the WD population. In this first instance, we neglect any redshift distribution, and place all the binaries at redshift 0, in order to find what influence the chirp mass distribution has on the GWB.

If we only include 1 chirp mass and one birth frequency ν_0, we of course get a single line following $\Omega \propto f^{2/3}$, by construction. We choose $\mathcal{M} = 0.52$, corresponding to two WDs of $0.6 M_\odot$. The merger frequency as determined from Roche lobe overflow ($\nu_{\max,2}$ in our earlier explanation) is equal to $\nu_{\text{merge}} \approx 19$ mHz. Figure 2.7 shows what happens when we allow the birth frequency of the binaries - still all with the same chirp mass - to vary. We start with 10 birth frequencies distributed uniformly in $\log_{10} \nu$ between 10^{-5} Hz and $\nu_{0,\max} = 0.003$ Hz (which is chosen in order to suit the illustration). The background indeed becomes a sum of the different lines, and some properties become apparent. First of all, the merger frequency is clearly indicated by the drop around $\log_{10}(2\nu_{0,\max}/\text{ Hz}) \approx -1.4$. Furthermore, if the binary has $f_0 = 2\nu_0 \gtrsim 10^{-4}$ Hz, the binary merges within a Hubble time, i.e. the line extends to the merger frequency. However, the two lines corresponding to binaries born with lower frequencies only extend over a small frequency range: (2.5) does not allow them to merge within a Hubble time, and due to the strong ν-dependence of (2.2), the frequency of these binaries barely changes. This is therefore part of the static regime.

Increasing the sample of birth frequencies to 1000 values results in a smooth curve, shown in the bottom panel of Figure 2.7. On the one hand, this curve exhibits $\Omega \propto f^{2/3}$ between $\nu_{0,\max}$ and ν_{merge}, by construction. Furthermore, the indicative yellow line follows a power law $\Omega \propto f^{10/3}$, which was the prediction for the static regime. This shows that the background approximately shows this behaviour indeed. In between there is a transition region, where the exponent of the power law decreases.

We add a second type of binary, with masses $0.3 M_\odot, 0.9 M_\odot$ and therefore $\nu_{\text{merge}} \approx 42$ mHz. We allow it to have the same range of birth frequencies as the other, which leads to the background in Figure 2.8. The background is now the sum of both components.

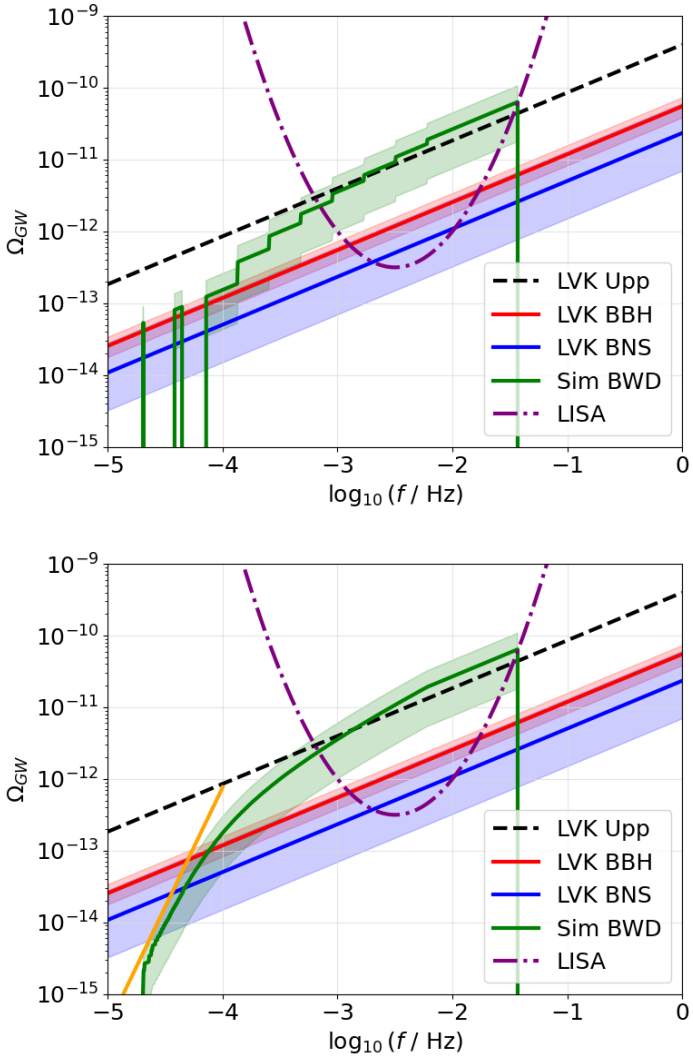

Figure 2.7: Influence of the number of birth frequencies on the GWB, for binaries conisting of two $0.6M_\odot$ WDs. *(top)* Ten samples for the birth frequency ν_0 uniformly distributed between 10^{-5} Hz and 3 mHz on a logarithmic scale. *(bottom)* The same interval for the birth frequency, but now with 1000 samples. The yellow line is a comparative $\Omega \propto f^{10/3}$ line. The LISA sensitivity curve and extrapolations based on LIGO data are shown as well.

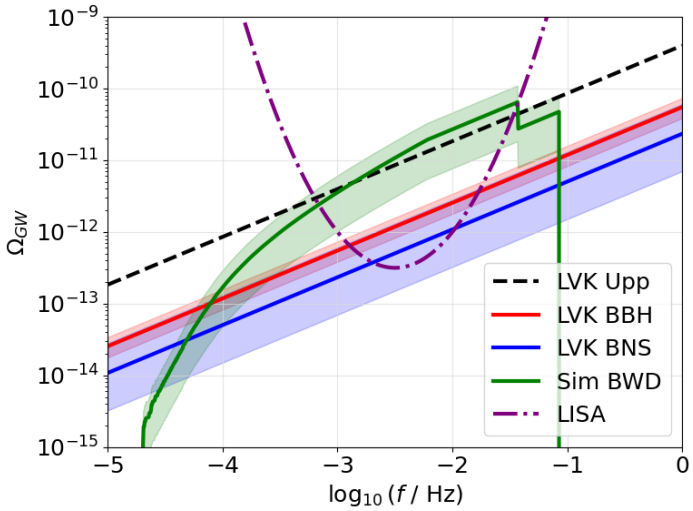

Figure 2.8: GWB resulting from two types of binaries, one with two $0.6M_\odot$ WDs, and one with $(0.3, 0.9)M_\odot$ components. The birth frequencies are uniformly distributed between 10^{-5} Hz and 3 mHz on a logarithmic scale. The LISA sensitivity curve and extrapolations based on LIGO data are shown as well.

This becomes apparent above the merger frequency of the original binary, where the curve displays a sharp drop due to all the binaries of the first type merging. The new type of binaries that we added has a larger merger frequency, corresponding to the second drop around 0.1 Hz. Therefore, adding more different types of binaries, all having different merger frequencies, will smoothen out the drop at the high-frequency end of the GWB. This can be seen in Figure 2.10 where we show the background resulting from a realistic population of WD binaries.

The population synthesis

In order to get a more realistic prediction, we use the results of a population synthesis (PS). The `SeBa` code [Nelemans et al., 2001, Portegies Zwart and Verbunt, 1996, Portegies Zwart and Yungelson, 1998, Toonen et al., 2012] uses fast recipes to evolve a large number $\sim 10^6$ binary systems. The stars are initialised as zero-age main sequence (ZAMS) stars, and are evolved for a Hubble time, taking into account effects of single and binary evolution. The results of the code are then the end products of all these initial binaries, which can be a binary or one or two single objects (i.e. the binary merges or detaches). Results for double WD have been discussed in [Nelemans et al., 2001] and [Toonen et al., 2012] and compared to observations to ensure they are not incompatible with them.

The results of the code have to be normalized: the initial binary population has to correspond to an amount of star formation that can create this initial population. As an example, [Toonen et al., 2012] found that the number of produced binaries per solar mass star formation is equal to $6.9 \cdot 10^{-3} M_\odot^{-1}$. The population that we use corresponds to $1.5 \cdot 10^6 M_\odot$ of star formation, and contains 14418 WD binaries. Therefore, the normalization constant for this file is $9.6 \cdot 10^{-3} M_\odot^{-1}$. The initial stellar binaries are evolved, and when they become WD binaries their component masses and separation are registered.

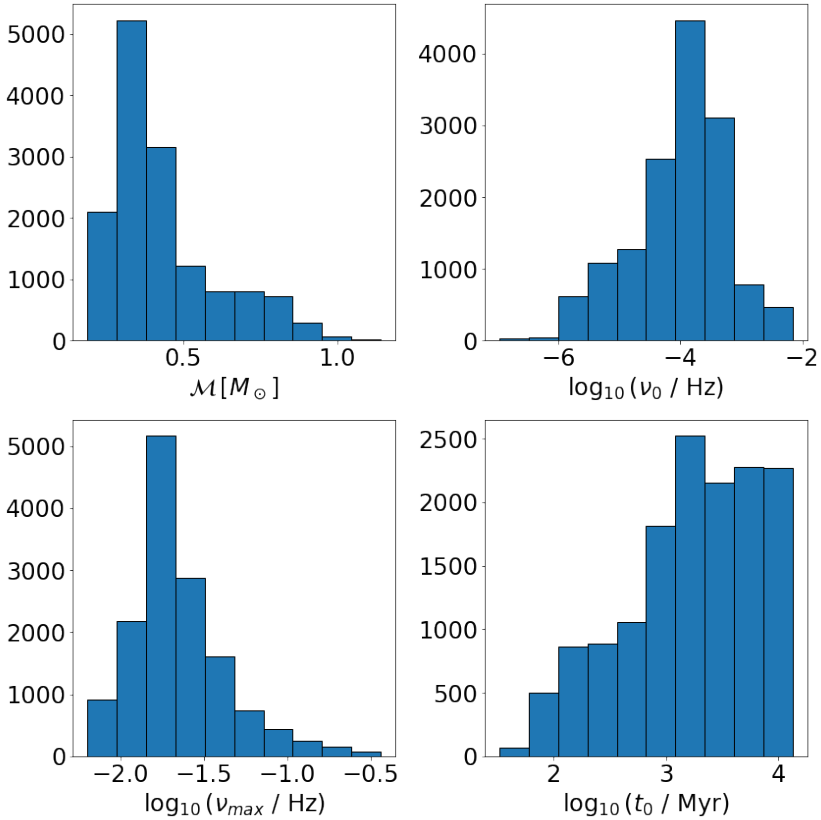

Figure 2.9: Summary of population synthesis results. *(top)* The chirp mass and birth frequency of the binary. *(bottom)* The merger frequency due to Roche-lobe contact and the time delay between the start of the simulation and the formation of the binary. Population obtained from prof. Nelemans, obtained with the `SeBa` code.

The time of the birth (i.e. the time since the start of the simulation) of the WD binary is registered as well, and the collection of all these parameters makes up our binary WD population. We convert the separation at birth to a frequency with (2.1), and we calculate the maximum orbital frequency before the onset of Roche-lobe overflow using (2.30). A histogram summarizing the population is shown in Figure 2.9.

The background obtained from this population, with all sources located at $z = 0$, can be seen in Figure 2.10. The drop at the high-frequency end is now smoothened out to a gradual decline, due to the different merger frequencies of all the binaries. The WD background only drops below that of the BHs above 0.1 Hz. Between $10^{-3} - 10^{-2}$ Hz, the background approximately follows $\Omega \propto f^{2/3}$.

2.4.3 Influence of the redshift

So far, we have assumed that all binaries are located at $z = 0$. However, we want to model the GWB from all extragalactic WD binaries, meaning that we need to include the contribution from all redshifts. Again, we consider some toy models before we move on to a more realistic setting.

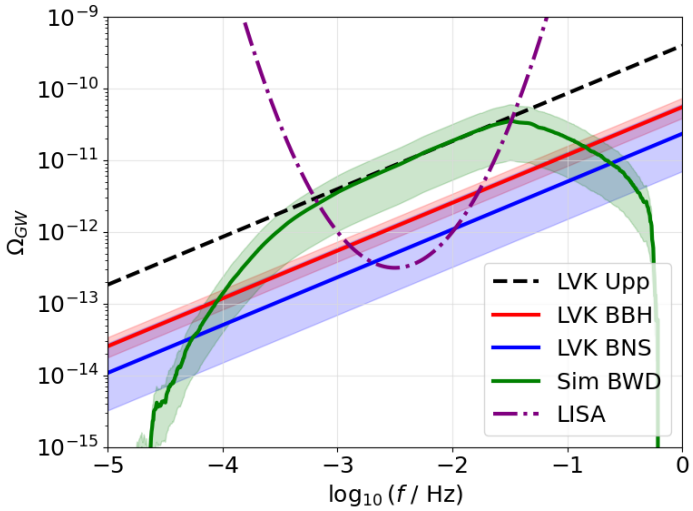

Figure 2.10: Background resulting from the PS results, all located at $z = 0$. The LISA sensitivity curve and extrapolations based on LIGO data are shown as well.

We start again with one type of binaries, a pair of 0.6 $M_\odot$ WDs ($\mathcal{M} = 0.52$), and birth frequency distributed uniformly in $\log_{10}\nu$ between 10^{-5} Hz and $\nu_{0,\max} = 0.003$ Hz. Contrary to Figure 2.7, we now place all the binaries at redshift $z = 3$, and the resulting background is shown in Figure 2.11. The merger frequency is ≈ 19 mHz, but due to the redshift the frequency at which the sharp drop occurs is $f_{r,\mathrm{merge}} = 2 \cdot 19$ mHz $/(1+3) \approx 0.01$ Hz. The result is that the entire background is shifted to lower frequencies, compared to Figure 2.7 - this is of course exactly the effect of redshift. The decrease in amplitude is due to the normalization at 1 mHz, though signals from larger redshifts reach us with a lower amplitude as well.

Moving now to a distribution in redshifts, we consider the same type of binaries, but all with birth frequency $\nu_0 = 0.5$ mHz. We assume a homogeneous distribution in the redshift interval $[0, 8]$. The results are shown in Figure 2.12, for 10 samples in the redshift interval, and 100 samples. The line resulting from the $z = 0$ contribution stretches between $f \sim 1$ mHz and $f \sim 40$ mHz. The top panel shows that summing over the redshift distribution corresponds to summing over the redshifted versions of this line. The bottom panel shows that, if our distribution is smoothened out, the effect of the redshift is to round of the drop in frequency at both ends. The $\Omega \propto f^{2/3}$ behaviour now extends between the original birth frequency, and maximally redshifted merger frequency[13].

Finally, Figure 2.13 shows the results of our code where we used the PS results, and assumed a homogeneous Universe for redshifts in the interval $[0, 8]$. We divided this redshift interval in 20 equal bins, and took the average redshift in each bin as a representative value. The bin then contributes according to (2.33). At each bin, we added the contribution of the entire population. The end result is then normalized to correspond to

[13]For the binaries that we considered in this toy example, the merger time is on the order of ~ 6 Myr. This is a factor 100 smaller than the age of the Universe at redshift 8, meaning that the merger frequency due to Roche-lobe overflow is always the relevant one, as opposed to $\nu_{\max,1}$.

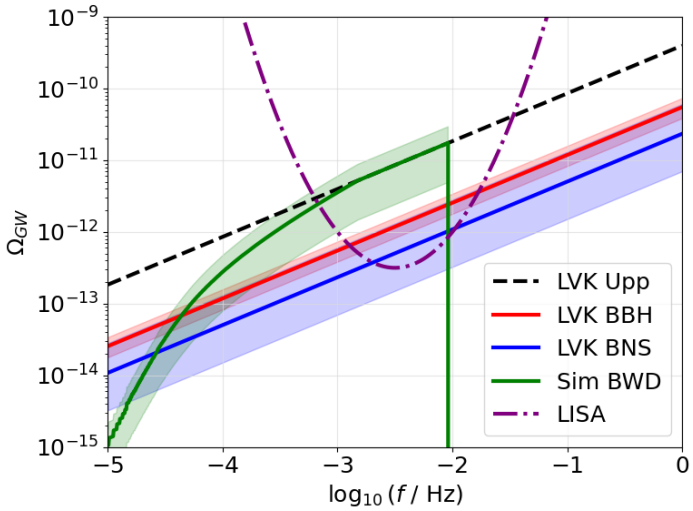

Figure 2.11: Background resulting from binaries with a pair of $0.6M_\odot$ WDs, with varying birth frequency ν_0 and all located at $z = 3$. The LISA sensitivity curve and extrapolations based on LIGO data are shown as well.

the value $\Omega(1\ \mathrm{mHz}) = 3.57 \cdot 10^{-12}$ [Farmer and Phinney, 2003]. This result can be compared to Figure 2.2. The qualitative features of both simulations are very similar: a peak around ~ 10 mHz, approximate $\Omega \propto f^{2/3}$ behaviour between ~ 1 and ~ 10 mHz, and a transition from the static to the inspiral regime around ~ 0.1 mHz. The decrease that we find at the high-frequency end is less severe than in Figure 2.2, however: they found, $\Omega(0.1\ \mathrm{Hz}) \approx \Omega(0.1\ \mathrm{mHz})$.

The bottom panel of Figure 2.13 shows the sum of the different GWBs originating from coalescing compact binaries. The error on this background is determined by standard error propagation. Throughout most of the frequency band where LISA is sensitive enough to detect the background, the latter approximately follows $\Omega \propto f^{2/3}$. Only at the high-frequency end, the drop due to merging WD binaries is visible. Therefore, this small region is the only regime where the influence of one of the components (the WDs) could be disentangled.

Of course, part of the agreement between our model and that of [Farmer and Phinney, 2003] is explained by the fact that we normalize our results to their value $\Omega(1\ \mathrm{mHz}) = 3.57 \cdot 10^{-12}$. In the next section, we want to provide an independent prediction for the background by taking all the constants and prefactors into account. Additionally, this more elaborate approach also takes the cosmic SFH correctly into account.

2.5 The total background: an unnormalized approach

In this final section, we construct a prediction for the GWB from extragalactic WD binaries *without normalizing the results* to the values found by [Farmer and Phinney, 2003]. We now also take the cosmic SFH into account, and change it in Sec. 2.5.4 to investigate its effect on the background and its amplitude. The SFR we start from is

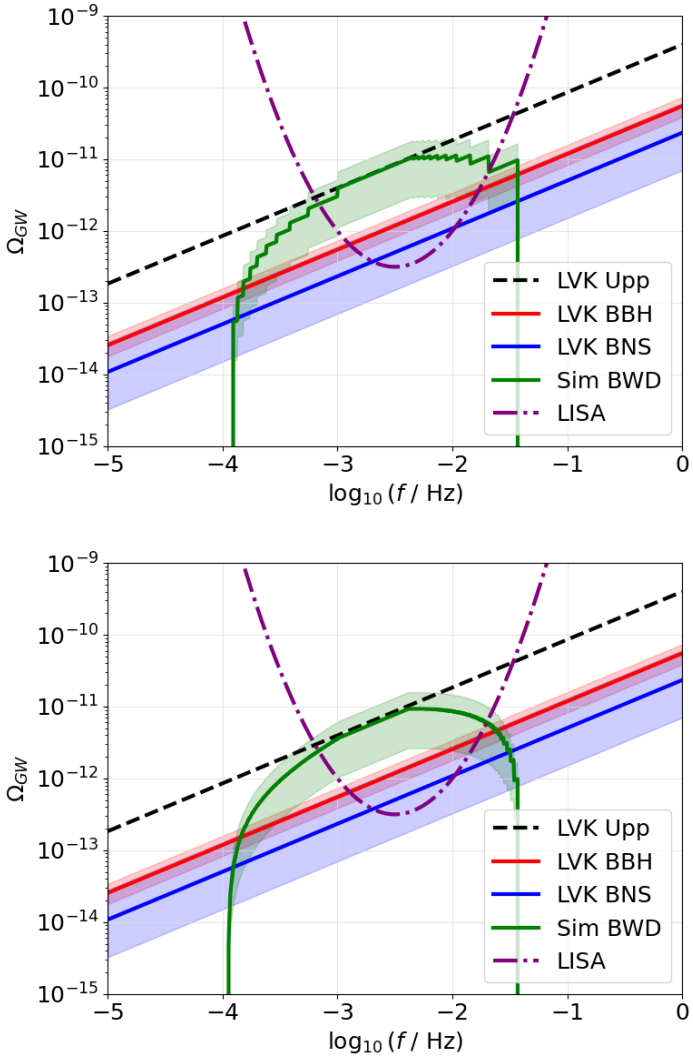

Figure 2.12: Influence of a redshift distribution on the GWB, for binaries conisting of two $0.6M_\odot$ WDs. *(top)* Ten samples for the redshift z uniformly distributed in [0,8]. *(bottom)* The same interval for the redshift, but now with 1000 samples. The LISA sensitivity curve and extrapolations based on LIGO data are shown as well.

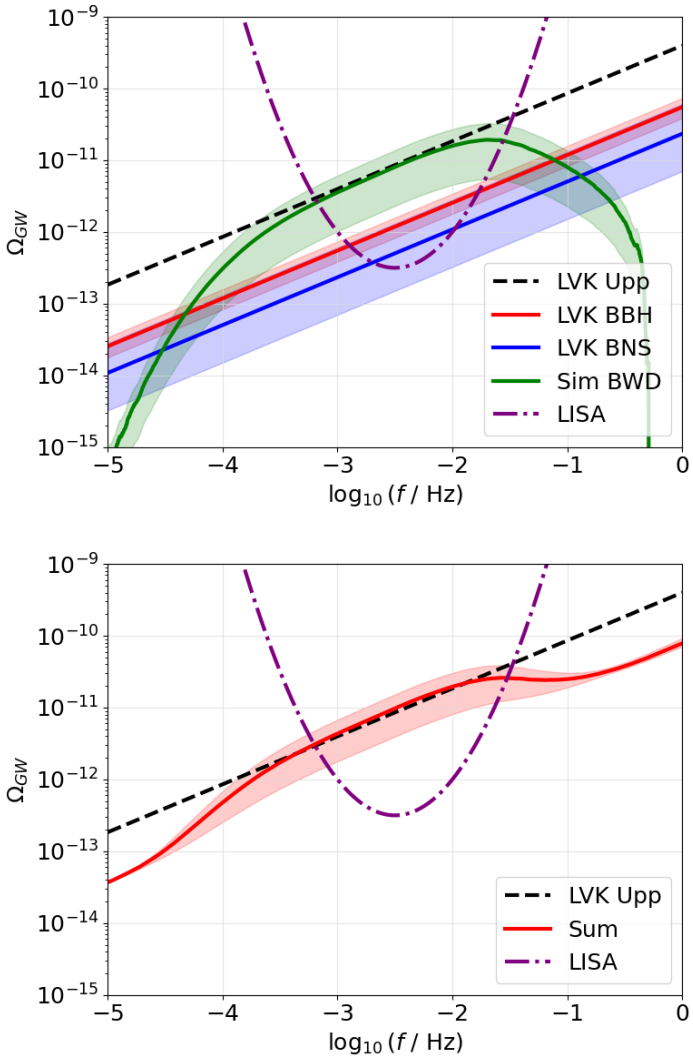

Figure 2.13: *(top)* GWB due to WD binaries generated from the population synthesis results, under the assumption of a homogeneous Universe in the redshfit interval $z \in [0, 8]$. The LISA sensitivity curve and extrapolations based on LIGO data are shown as well. *(bottom)* Total GWB arising as the sum of the three components in the upper panel.

given by [Madau and Dickinson, 2014]

$$\psi_1(z) = 0.015\frac{(1+z)^{2.7}}{1+[(1+z)/2.9]^{5.6}} \quad M_\odot \text{ yr}^{-1} \text{ Mpc}^{-3}\,. \tag{2.34}$$

This expression is plotted in Figure 2.18, and shows that the star-formation rate density peaked approximately 3.5 Gyr after the Big Bang, at $z \approx 1.9$.

2.5.1 Method

We base our method on Sec. 6 of [Farmer and Phinney, 2003]. From (2.31), a flux is obtained by integrating the specific flux over a frequency bin $[f_{r_1}, f_{r_2}]$, giving

$$F_{f_{r_1}\to f_{r_2}} = \int_{z=0}^{\infty}\int_{f_{r_1}(1+z)}^{f_{r_2}(1+z)} \frac{l_{f_e}}{(1+z)^2}\mathrm{d}f_e\mathrm{d}\chi(z)\,,$$

where the relation $f_e = f_r(1+z)$ is used. This expression essentially shows that we integrate over all the source frequencies that get redshifted to the correct observed frequency bin.

We can now break the specific luminosity density down into its contributions from different systems. We work with the results from the PS, described in Sec. 2.4.2. Using an index k to denote the systems, together with (2.27), we find that the flux is given by

$$F_{f_{r_1}\to f_{r_2}} = \sum_k \int_{z=0}^{\infty}\frac{\mathrm{d}\chi(z)}{(1+z)^2}\int_{f_{r_1}(1+z)}^{f_{r_2}(1+z)}\int_{\nu_0}^{\nu_{\text{merge}}} n_k(\nu,z)L_k(\nu)\delta(f_e-2\nu)\mathrm{d}f_e\mathrm{d}\nu\,.$$

where $n_k(\nu, z)$ is the specific number density at redshift z. We use the δ-distribution to get rid of the integral over f_e to find

$$F_{f_{r_1}\to f_{r_2}} = \sum_k \int_{z=0}^{\infty}\frac{\mathrm{d}\chi(z)}{(1+z)^2}\int_{\nu_{\text{min}}}^{\nu_{\text{max}}} n_k(\nu,z)L_k(\nu)\mathrm{d}\nu\,. \tag{2.35}$$

In this expression, $\nu_{\text{min}} = \max\{\nu_0, f_{r_1}(1+z)/2\}$ and $\nu_{\text{max}} = \min\{\nu_{\text{merge}}, f_{r_2}(1+z)/2\}$.

We already argued that $n(\nu) \propto \nu^{-11/3}$ in Sec. 2.3.2, and have an expression for $L_k(\nu)$ being (2.24). We can normalize the specific number density (with proportionality constant A) by demanding that

$$\int_{\nu_{\text{min}}}^{\nu_{\text{max}}} A\nu^{-11/3}\mathrm{d}\nu = n_{\text{bin}}\,, \tag{2.36}$$

where n_{bin} is the number density of systems with frequency between ν_{min} and ν_{max}. This can be estimated by multiplying the SFR with the time it takes for the system to traverse the frequency bin. Since the population synthesis results reflect the WD population for every $1.5 \cdot 10^6 M_\odot$, we find

$$n_{\text{bin}}(z) \approx \frac{\psi(z+z^*)}{1.5\cdot 10^6 M_\odot}\cdot \Delta t(k;\text{bin})\,. \tag{2.37}$$

The timespan Δt depends on the system through the chirp mass, and z^* is an increase in redshift to reflect the SFR when the system was born. Indeed, generally there is a time

delay between the birth of the system and the time where it enters the correct bin. We refer to this as the **generic case**, where $\nu_{\min} = f_{r_1}(1+z)/2$ and $\nu_{\max} = f_{r_2}(1+z)/2$. We find

$$A = \frac{8}{3}\frac{1}{\nu_{\min}^{-8/3} - \nu_{\max}^{-8/3}} \frac{\psi(z + z^*(\Delta t))}{1.5 \cdot 10^6 M_\odot} \cdot \Delta t(k; \text{bin}) \,, \tag{2.38}$$

or in the generic case

$$A \approx 0.42 \frac{(1+z)^{8/3}}{f_{r_1}^{-8/3} - f_{r_2}^{-8/3}} \frac{\psi(z + z^*(\Delta t))}{1.5 \cdot 10^6 M_\odot} \cdot \Delta t(k; \text{bin}) \,. \tag{2.39}$$

The integral over ν in (2.35) can be carried out as well, as we have $n_k(\nu, z) L_k(\nu) \propto \nu^{-1/3}$, and

$$\int_{\nu_{\min}}^{\nu_{\max}} \nu^{-1/3} \mathrm{d}\nu = \frac{3}{2}\left(\nu_{\max}^{2/3} - \nu_{\min}^{2/3}\right) \,.$$

Therefore, we find

$$F_{f_{r_1} \to f_{r_2}} = 8.8 \cdot 10^{38} \sum_k \left(\frac{\mathcal{M}_k}{M_\odot}\right)^{10/3} \int_{z=0}^{\infty} \frac{\nu_{\max}^{2/3} - \nu_{\min}^{2/3}}{\nu_{\min}^{-8/3} - \nu_{\max}^{-8/3}} \frac{\psi(z; k; \text{bin})}{1.5 \cdot 10^6 M_\odot} \Delta t(k; \text{bin}) \frac{\mathrm{d}\chi(z)}{(1+z)^2} \frac{\text{J Hz}^{-10/3}}{\text{s}} \,,$$

or in the generic case

$$F_{f_{r_1} \to f_{r_2}} = 8.7 \cdot 10^{37} \sum_k \left(\frac{\mathcal{M}_k}{M_\odot}\right)^{10/3} \int_{z=0}^{\infty} \frac{f_{r_2}^{2/3} - f_{r_1}^{2/3}}{f_{r_1}^{-8/3} - f_{r_2}^{-8/3}} \frac{\psi(k; \text{bin})}{1.5 \cdot 10^6 M_\odot} \Delta t(k; \text{bin}) \frac{\mathrm{d}\chi(z)}{(1+z)^{-4/3}} \frac{\text{J Hz}^{-10/3}}{\text{s}} \,.$$

Generic case

We focus first on the generic case for simplicity. In this case, the factor with frequencies can be taken out of the integral. We discretize this integral over z to find

$$\begin{aligned} F_{f_{r_1} \to f_{r_2}} =& 6.1 \cdot 10^{-14} \frac{f_{r_2}^{2/3} - f_{r_1}^{2/3}}{f_{r_1}^{-8/3} - f_{r_2}^{-8/3}} \\ &\times \sum_{k,i} \left(\frac{\mathcal{M}_k}{M_\odot}\right)^{10/3} (1+z_i)^{4/3} \frac{\psi(k; \text{bin}; z_i)}{M_\odot \text{ yr}^{-1} \text{ Mpc}^{-3}} \frac{\Delta t(k; \text{bin}; z_i)}{\text{yr}} \frac{\Delta\chi(z_i)}{\text{Mpc}} \frac{\text{kg}}{\text{s}^3} \,. \end{aligned} \tag{2.40}$$

In this expression, we now treat the frequencies as being dimensionless, i.e. divided by Hz. The change in prefactor is due to the conversion of Mpc^2 to m^2.

We focus now on the time interval Δt and the shift in redshift. The time interval Δt for the generic case is determined by

$$\Delta t(k; \text{bin}; z) \approx 2.4 \frac{(1+z)^{-8/3}}{K(\mathcal{M})} \left(f_{r_1}^{-8/3} - f_{r_2}^{-8/3}\right) \,, \tag{2.41}$$

which is found by solving (2.5). We will carry the $(1+z)^{-8/3}$ factor to the final result, and we see that the factor with frequencies drops out with respect to the prefactor of (2.40). Furthermore, we use (2.4) and convert seconds to years to find

$$\begin{aligned} F_{f_{r_1} \to f_{r_2}} =& 1.3 \cdot 10^{-15} \left(f_{r_2}^{2/3} - f_{r_1}^{2/3}\right) \\ &\times \sum_{k,i} \left(\frac{\mathcal{M}_k}{M_\odot}\right)^{5/3} (1+z_i)^{-4/3} \frac{\psi(k; \text{bin}; z_i)}{M_\odot \text{ yr}^{-1} \text{ Mpc}^{-3}} \frac{\Delta\chi(z_i)}{\text{Mpc}} \frac{\text{kg}}{\text{s}^3} \,. \end{aligned} \tag{2.42}$$

We also determine

$$\tau_k = \frac{3}{8K(\mathcal{M}_k)} \left(\nu_0^{-8/3} - (f_{r_1}(1+z)/2)^{-8/3} \right) , \tag{2.43}$$

i.e. the time the system takes to evolve from its birth frequency to the lower end of the redshifted frequency bin[14]. The PS results give us a time $t_{0,k}$ for each system, reflecting the delay between star formation and the formation of the WD binary at birth frequency ν_0. We determine z^* such that $z + z^*$ corresponds to a time $\tau_k + t_{0,k}$ before the time corresponding to z. In practice, we again restrict to $z \in [0, 8]$, as (2.34) was determined on this interval, and Sec. 2.5.3 shows that high-redshift contributions are negligible anyway. Therefore, we only include the contribution of system k if $\tau_k + t_{0,k} \leq \tau(z) - \tau(z = 8)$, where $\tau(z)$ is the age of the Universe at redshift z. The representative SFR is then $\psi(z + z^*)$.

Finally, this results in an expression for Ω. We use that

$$\Omega(f_r) \approx \frac{1}{\rho_c c^3} \frac{f_r F_{f_{r_1} \to f_{r_2}}}{f_{r_2} - f_{r_1}} \approx \frac{4.3}{\text{kg s}^{-3}} \frac{f_r F_{f_{r_1} \to f_{r_2}}}{f_{r_2} - f_{r_1}} , \tag{2.44}$$

which gives us that

$$\Omega(f_r) = 5.4 \cdot 10^{-15} f_r \frac{f_{r_2}^{2/3} - f_{r_1}^{2/3}}{f_{r_2} - f_{r_1}} \sum_{k,i} \left(\frac{\mathcal{M}_k}{M_\odot} \right)^{5/3} (1 + z_i)^{-4/3} \frac{\psi(z_i + z^*_{k,\text{bin}})}{M_\odot \text{ yr}^{-1} \text{ Mpc}^{-3}} \frac{\Delta\chi(z_i)}{\text{Mpc}} . \tag{2.45}$$

The frequencies f_r at which Ω is plotted are chosen such that there is 1 per bin, halfway the bin on a logarithmic scale.

Other cases

In general, we have that

$$\Delta t = \frac{3}{8K(\mathcal{M})} \left(\nu_{\text{min}}^{-8/3} - \nu_{\text{max}}^{-8/3} \right) , \tag{2.46}$$

which gives after discretizing the integral

$$\begin{aligned} F_{f_{r_1} \to f_{r_2}} = & 2.0 \cdot 10^{-15} \sum_{k,i} \left(\frac{\mathcal{M}_k}{M_\odot} \right)^{5/3} \\ & \times \left(\nu_{\text{max}}^{2/3} - \nu_{\text{min}}^{2/3} \right) (1 + z_i)^{-2} \frac{\psi(k; \text{bin}; z_i)}{M_\odot \text{ yr}^{-1} \text{ Mpc}^{-3}} \frac{\Delta\chi(z_i)}{\text{Mpc}} \frac{\text{kg}}{\text{s}^3} . \end{aligned} \tag{2.47}$$

This then leads to

$$\Omega(f_r) = 8.5 \cdot 10^{-15} f_r \sum_{k,i} \left(\frac{\mathcal{M}_k}{M_\odot} \right)^{5/3} \frac{\nu_{\text{max}}^{2/3} - \nu_{\text{min}}^{2/3}}{f_{r_2} - f_{r_1}} (1 + z_i)^{-2} \frac{\psi(k; \text{bin}; z_i)}{M_\odot \text{ yr}^{-1} \text{ Mpc}^{-3}} \frac{\Delta\chi(z_i)}{\text{Mpc}} . \tag{2.48}$$

Finally, we remark that

$$\tau_k = \frac{3}{8K(\mathcal{M})} \left(\nu_0^{-8/3} - \nu_{\text{min}}^{-8/3} \right) , \tag{2.49}$$

[14] Normally, $\Delta t(k; \text{bin}; z) \ll \tau_k$,such that it does not matter which frequency in the bin we choose for τ_k. This also means that we can assume the entire bin is populated, as we already assumed $f_{r_2}(1+z)/2 < \nu_{\text{max}}$.

which in the birth frequency bin is equal to 0, meaning that z^* is based on t_0 only. For the merger bin, both need to be taken into account again.

Computationally, we noted that mostly the calculation of z^* increased the computing time. The computation time could be lowered by performing an integration over cosmic time instead of redshift, as originally done in [Farmer and Phinney, 2003]. However, this then requires a calculation of $\psi(t)$, the SFR as a function of cosmic time t.

2.5.2 Results

First, we benchmark our code by reproducing simple results. We select one random binary system from our PS results,

$$(m_1, m_2, \nu_0, t_0) = (0.76M_\odot, 0.72M_\odot, 1.6 \cdot 10^{-4}\ \text{Hz}, 384\ \text{Myr})\,,$$

and run the code with $z = 0$ and constant star formation rate $\psi_1(0)$ to see if it reproduces $\Omega \propto f^{2/3}$ as expected, and Figure 2.14 shows that it does. Furthermore, the line indeed extends from $\log_{10}(2\nu_0) \approx -3.5$ to $\log_{10}(2\nu_{\text{max}}) \approx -1.3$, where the limiting frequency is determined by Roche-lobe overflow. This is appropriate, as the timescale for the binary to cross this frequency interval is on the order of ~ 0.1 Gyr. The amplitude[15] is multiplied with 14418 - the number of systems in the PS results - to give the same order of magnitude as the full results. The bottom panel in Figure 2.14 shows that including higher redshifts works as expected as well: we used 20 redshift bins in [0,8], and now the lowest frequency present in the background is at $\log_{10}(2\nu_0/9) \approx -4.4$. The highest frequency present is slightly smaller than the one in the top panel: this is due to the fact that the first redshift bin uses $z = 0.4$ as representative value, instead of $z = 0$ which is done in the upper panel.

We show the results of our program using the SFR (2.34) in Figure 2.15. This background is constructed using 50 frequency bins, logarithmically spaced in the interval $[10^{-5}, 1]$ Hz. Furthermore, we used 20 redshift bins in the interval [0,8]. We checked that the results of our code did not depend on the number of bins. The errors shown with this prediction correspond to the same relative errors given on the original prediction of [Farmer and Phinney, 2003], for comparison. Again, we find a peak around 10 mHz, and the other qualitative features of the curve seem similar to what we found in Sec. 2.4.

However, the amplitude of the GWB is higher than the predictions of [Farmer and Phinney, 2003]. We find $\Omega(1\ \text{mHz}) = 1.79 \cdot 10^{-11}$, which is roughly a factor 5 larger than what they found. A factor of this order can have several reasons. First of all, the SFH used in [Farmer and Phinney, 2003] is overall roughly a factor 2 smaller than (2.34), at least for the low redshifts that dominate the background (see Sec. 2.5.3). Secondly, they test their models for the WD population by using their PS code to obtain a representative Galactic population. Doing so, they find a local total space density of $9 \cdot 10^{-3}$ pc^{-3}. This can be compared to [Nelemans et al., 2001], where they find this density to be $19 \cdot 10^{-3}$ pc^{-3}.

[15] It would be good to benchmark the amplitude as well. This could for example be done by calculating (2.13) analytically for a relatively simple case, and implementing the same population in the code. We leave this for future work.

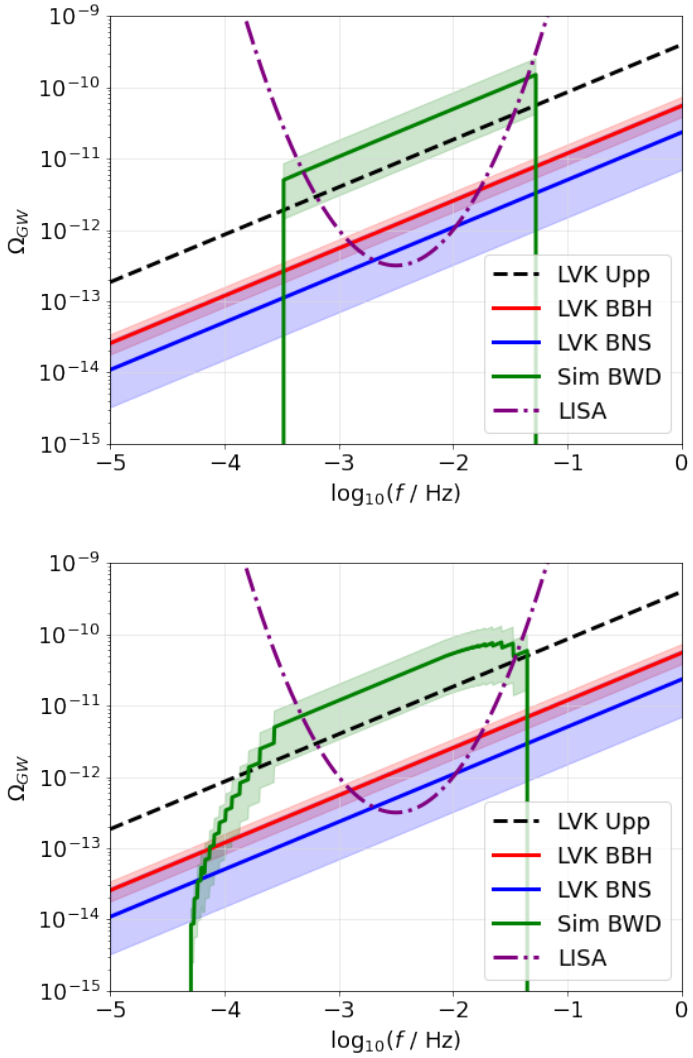

Figure 2.14: Benchmarking for the code described in Sec. 2.5.1. The top panel shows the expected $\Omega \propto f^{2/3}$ behaviour for a single type of binaries located at $z = 0$, and with constant SFR. The bottom panel shows the effect of adding redshift bins.

As the latter used the `SeBa` code that we take results from as well, this can also explain a factor $19/9 \approx 2.1$. Finally, we have already remarked on the need for a normalization in the code in Sec. 2.4.2. The different normalizations presented in that section could explain an additional factor $9.6/6.9 \approx 1.4$. Taking these arguments into account, we could expect to find a GWB that is a factor ~ 6 larger than what [Farmer and Phinney, 2003] found. It must be noted, however, that [Farmer and Phinney, 2003] also take harmonic contributions from eccentric orbits into account, which we neglected in our simulations.

Due to the larger amplitude, the total GWB covers a slightly larger frequency range in which LISA can detect it. Furthermore, the peak and subsequent decay are now more pronounced in the sensitivity region. The larger amplitude would imply an improved chance of detecting the background in this frequency range. Given that the decay at high frequencies is also more pronounced, this implies that the WD component could be more confidently identified as well, as it is the one deviating from $\Omega \propto f^{2/3}$ in the LISA band.

We also investigate the contribution of the birth and merger frequency bins to the total background. The reason is that excluding these allows us to only use the equations for the generic case in Sec. 2.5.1, which make the code a bit faster and simpler. The results are plotted in Figure 2.16. As expected, the contribution of birth frequency bins is at low frequencies, and that of merger bins at high frequencies. In both cases, the contribution is small in the LISA band $\sim 0.1 - 10$ mHz. Below $\lesssim 10^{-4}$ Hz and above $\gtrsim 0.1$ Hz, the contribution becomes significant, or even dominant. Increasing the number of frequency bins would decrease the contribution further - though it also increases the computation time.

2.5.3 Contribution of different redshifts

In practice, we will choose redshift bins in the interval $z \in [0, 8]$, since the SFR (2.34) is determined in this range [Madau and Dickinson, 2014]. At redshift 8, the Universe was about 600 Myr old. A priori, it could be necessary to include higher redshifts as well, because white dwarfs might have formed earlier. WDs have been found that are over 11 Gyr old [Kilic et al., 2012], and given that stars more massive than $\gtrsim 3.5 M_\odot$ have main-sequence lifetimes shorter than this (see (1.2)), perhaps even older WDs exist.

However, Figure 2.17 shows that large redshifts barely contribute to the total GWB. Indeed, $\gtrsim 90\%$ of the background is due to binaries with $z \lesssim 2.5$, in the case of SFR (2.34). This is due to the fact that the comoving volume related to high redshift bins is relatively small. Therefore, we do not need to include redshifts beyond $z = 8$, as they will contribute negligibly to the total GWB.

Furthermore, since we are interested in the background from extragalactic binaries, we should in principle exclude the Milky Way in our redshift binning. However, since the nearest galaxies are at redshifts close to zero, this effect will dissapear in our binning procedure.

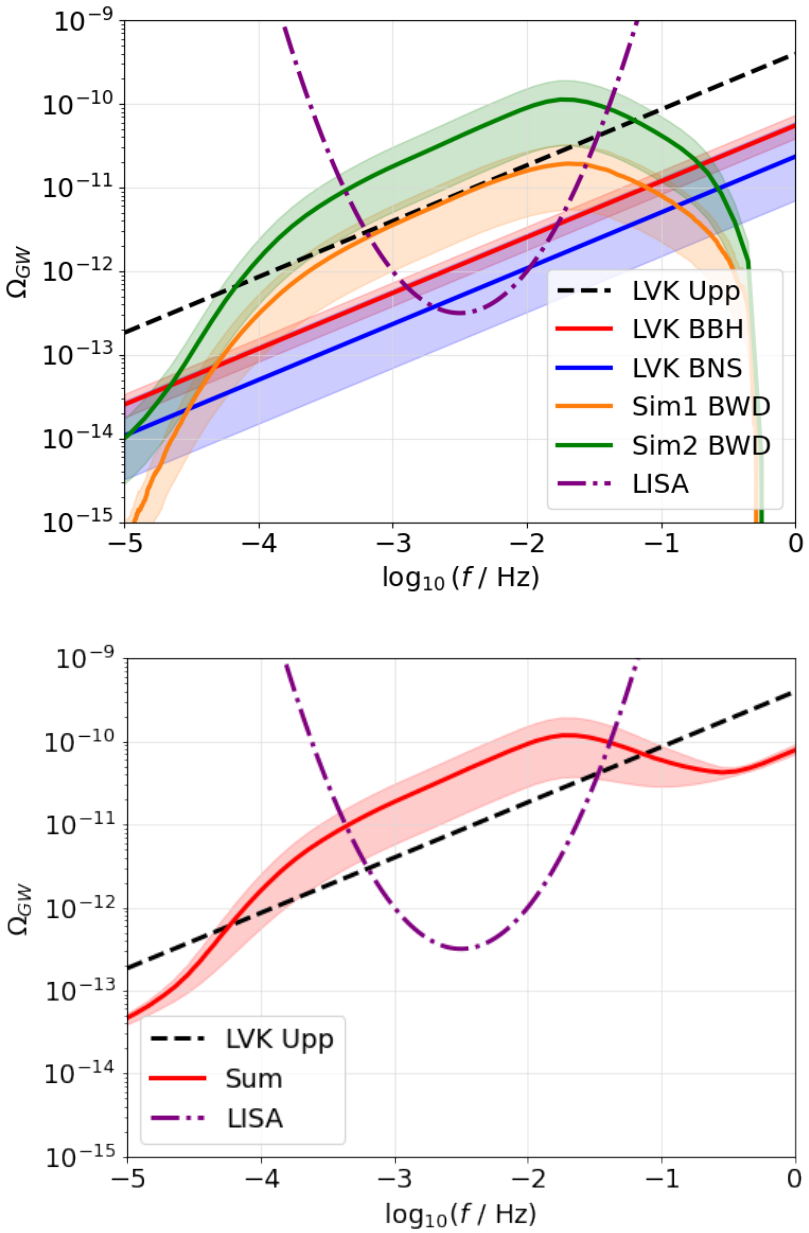

Figure 2.15: *(top)* Green: the predicted GWB from extragalactic WD binaries as determined by the cosmic star-formation history (2.34), based on the method in Sec. 2.5.1. The orange curve denotes the GWB that we found in Figure 2.13. The LISA sensitivity curve and extrapolations based on LIGO data are shown for comparison. *(bottom)* Total GWB arising as the sum of the three (green, blue, red) components in the upper panel.

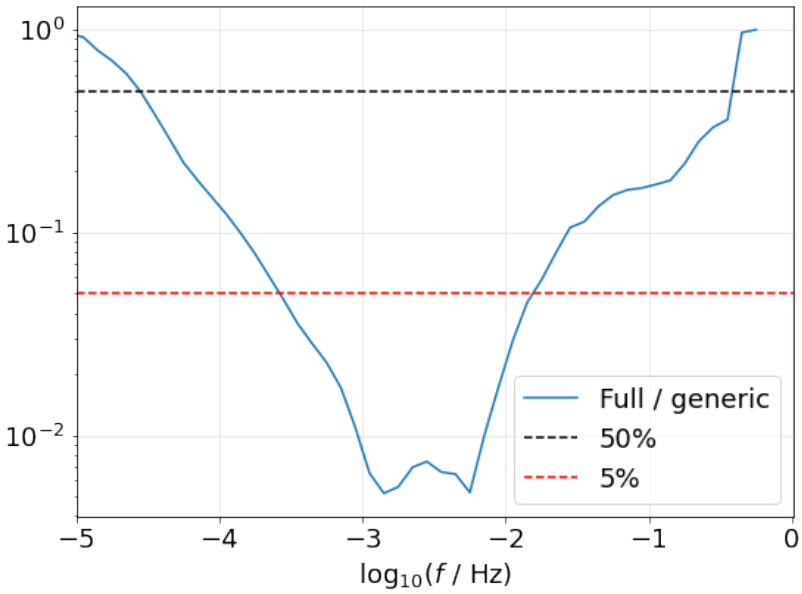

Figure 2.16: Contribution of the birth and merger frequency bins to the total background, in the case of 50 frequency bins. The line shows the ratio of the full background to the background that only considered contributions from the "generic" case, as defined in Sec. 2.5.1. The dashed lines mark a 50% and 5% contribution.

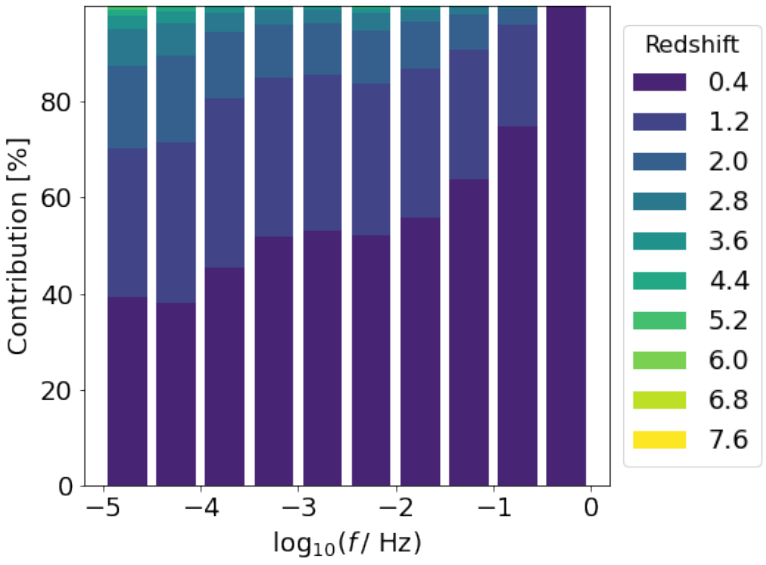

Figure 2.17: Contribution of the different redshift bins at different frequencies grouped in 10 frequency bins. The size of the rectangle represents the relative contribution. The indicative redshift indicated in the legend is in the middle of the bin, and all have width 0.8. This figure shows that $\gtrsim 90\%$ of the background is due to binaries with $z \lesssim 2.5$, in the case of SFH (2.34).

2.5.4 Influence of the star formation history

In this final section, we want to investigate what influence the SFH has on the background. To this end, we consider three alternative SFR functions, which are purely hypothetical, but highlight the ways the SFR could differ. These explorative models for the SFR are

$$\psi_2(z) = 0.074 \frac{(1+z)^{0.3}}{1+[(1+z)/2.9]^{3.2}} \quad M_\odot \text{ yr}^{-1} \text{ Mpc}^{-3}\,, \tag{2.50}$$

$$\psi_3(z) = 0.012 \frac{(1+z)^{2.7}}{1+[(1+z)/2.9]^{3}} \quad M_\odot \text{ yr}^{-1} \text{ Mpc}^{-3}\,, \tag{2.51}$$

$$\psi_4(z) = 0.0064 \frac{(1+z)^{2.7}}{1+[(1+z)/5]^{5.6}} \quad M_\odot \text{ yr}^{-1} \text{ Mpc}^{-3}\,. \tag{2.52}$$

The first one increases the SFR at lower redshifts, whereas the second one corresponds to a SFR that was much larger in the past. The final one shifts the peak of the SFR with respect to (2.34), and is now located around $z = 4$. These different functions, together with (2.34) are shown in Figure 2.18.

They are normalized such that the total mass (density) of stars ever formed (the time-integral of the SFR) is equal to the one given by (2.34). Following [Farmer and Phinney, 2003], we use $\Omega_{\star,\text{tot}}$ to denote this total. It is calculated as [Madau and Dickinson, 2014]

$$\Omega_{\star,\text{tot}} = (1-R)\int_0^{\tau_U} \psi(z)\frac{\mathrm{d}t}{\mathrm{d}z}\mathrm{d}z\,, \tag{2.53}$$

where $\tau_U \approx 13.8$ Gyr denotes the age of the Universe and R is the *return fraction*; the mass fraction of each generation of stars that is put back into the interstellar and intergalactic medium. The return fraction depends on the inital mass function (IMF) of the stellar population. We take the value $R = 0.27$, which corresponds to a Salpeter IMF, and is the one used in [Madau and Dickinson, 2014] to find (2.34). This gives us that $\Omega_{\star,\text{tot}} \approx 5.9{\cdot}10^8 M_\odot \text{ Mpc}^{-3}$. [Farmer and Phinney, 2003] found $\Omega_{\star,\text{tot}} = 5.0{\cdot}10^8 M_\odot \text{ Mpc}^{-3}$, using a different IMF with $R = 0.42$.

The GWBs that result from these different SFHs are shown in Figure 2.19, and representative values are given in Table 2.2. As we have seen in Figure 2.17, the majority of the background is determined by low redshifts. This conclusion does not change when we alter the SFH, as shown by the figures in Appendix B.1. Therefore, it is expected that the largest background is the one related to the SFH for which the SFR is the largest at low redshifts. Decreasing the low-redshift contribution results in the overall GWB being lower. Within the LISA sensitivity band, the background does not change significantly, except near the peak. At high frequencies, the SFH in which most stars formed at low redshift dominates, and the subsequent order is determined by the amplitude of the SFR at $z \approx 0$. At low frequencies, the order is reversed. It should be noted that the alternative SFHs that we explored are not the most realistic ones, and therefore the variation of the GWB for realistic SFHs is not expected to be very large. This conclusion was also drawn in [Farmer and Phinney, 2003].

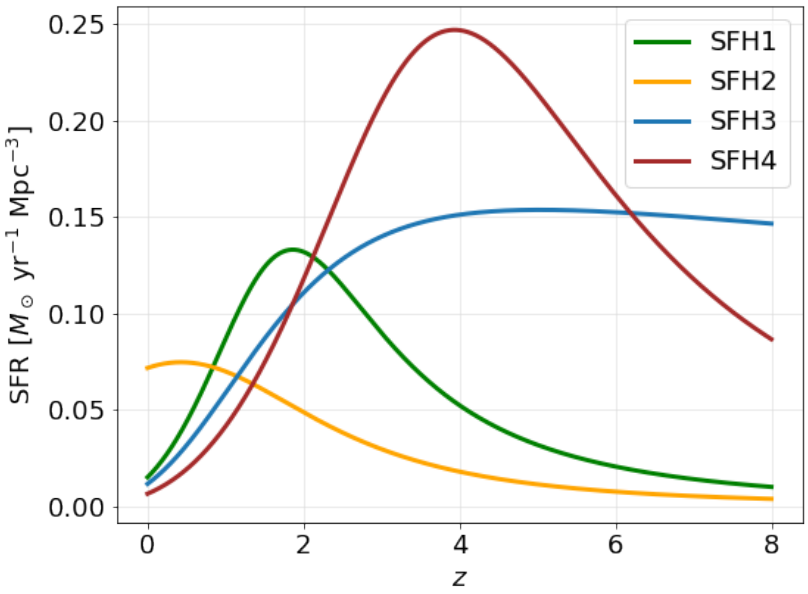

Figure 2.18: Different star formation histories considered for the models. SFH1 corresponds to (2.34), and is a realistic fit to observational data, obtained from [Madau and Dickinson, 2014]. The other three are explorative models, defined in (2.50) - (2.52). The normalization is chosen such that (2.53) is the same for all of them.

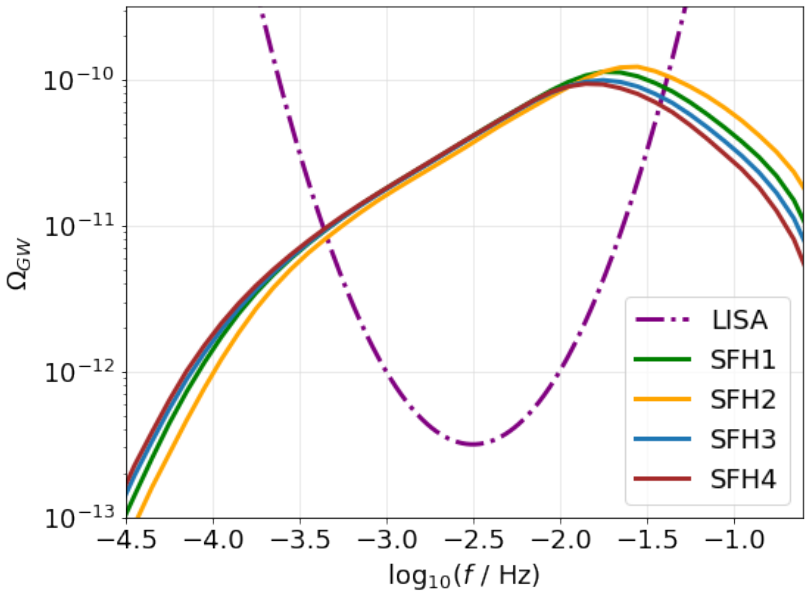

Figure 2.19: The GWB resulting from the different star-formation histories, as given by (2.34) and (2.50)-(2.52). The LISA sensitivity curve is shown, for comparison.

Table 2.2: Amplitude of the GWB at different frequencies, for the different SFHs that we have considered. The reference value of [Farmer and Phinney, 2003] is also given, in the bottom row. The largest value at each frequency is indicated in bold.

SFR	Ω(0.1 mHz)	Ω(1 mHz)	Ω(10 mHz)	Ω(0.1 Hz)
(2.34)	$1.41 \cdot 10^{-12}$	$1.79 \cdot 10^{-11}$	$\mathbf{8.97 \cdot 10^{-11}}$	$4.25 \cdot 10^{-11}$
(2.50)	$9.71 \cdot 10^{-13}$	$1.61 \cdot 10^{-11}$	$8.22 \cdot 10^{-11}$	$\mathbf{5.85 \cdot 10^{-11}}$
(2.51)	$1.61 \cdot 10^{-12}$	$1.77 \cdot 10^{-11}$	$8.54 \cdot 10^{-11}$	$3.41 \cdot 10^{-11}$
(2.52)	$\mathbf{1.79 \cdot 10^{-12}}$	$\mathbf{1.79 \cdot 10^{-11}}$	$8.56 \cdot 10^{-11}$	$2.77 \cdot 10^{-11}$
F&P	$\sim 10^{-13}$	$3.57 \cdot 10^{-12}$	$\sim 10^{-11}$	$\sim 10^{-13}$

Chapter 3

Hypercompact Stellar Clusters

In this chapter, we work around science objective 2 (Sec. 1.3): *"Trace the origin, growth and merger history of massive black holes across cosmic ages."* The formation history of SMBHs is still fairly uncertain, and we need observations to constrain it further. When SMBHs merge, they can receive a recoil kick in order to conserve the momentum that is carried away by the gravitational waves. The distribution of these kicks provides information on the merger history, as the kick velocity depends on the binary parameters. As a result of such a kick, a HCSC can form. However, these have not been observed yet, even though simulations predict hundreds of observable systems. In Sec. 3.1, we review the basics of the recoil kick and some structural relations for HCSCs. Subsequently, we review some observational predictions for these systems in Sec. 3.2. Furthermore, in Sec. 3.2.2 we motivate our choice to include smBHs in the models for HCSCs, which has not been done so far. Sec. 3.3 reviews earlier work on the modelling of these clusters, and we outline how we add smBHs in our method. Sec. 3.4 summarizes our overall findings, which we apply in Sec. 3.5 to model two candidate clusters. This enables us to delineate what parameter space could explain the observed properties of these systems.

3.1 Recoiling supermassive black holes

It is expected that the majority of galaxies harbor a SMBH in their nucleus. Therefore, the merger of two galaxies is likely to produce a SMBH binary where the nuclei of both galaxies collide. The heavy SMBHs sink to the center of the merging galaxies. Once they approach each other to (typically) within a few pc, they start kicking out stars on intersecting orbits via the gravitational slingshot effect [Merritt, 2006]. Therefore, the forming binary tends to lower the density of stars around it. If it completely depletes the reservoir of stars, the binary may stall at a separation which is not close enough for the gravitational radiation to drive the merger to its end. This is known as the *final parsec problem*, and in order to overcome it the reservoir of stars cannot be depleted. This is known as *loss-cone repopulation*, and we will come back to this in Sec. 3.1.1.

Once this hurdle is overcome, gravitational radiation drives the inspiral. It can be shown that the GWs carry away linear momentum, where the amount depends on the asymmetry in the binary masses or spins. The majority of the radiation is emitted close to the actual merger, and causes the remnant to experience a recoil kick in order to conserve momentum [Bekenstein, 1973]. These recoil kicks can be on the order of several 100-1000

km s^{-1}, with the most extreme velocites arising from rapidly spinng BHs on eccentric orbits [Campanelli et al., 2007, González et al., 2007]. As escape velocities of galaxies are typically $\lesssim 2000$ km s^{-1}, the largest kicks kan cause the remnant to be ejected from the galaxy. However, the more common case is that the kick does not exceed the escape velocity, and the remnant is temporarily displaced from the center of the galaxy. [Merritt et al., 2009]

The general idea in cosmology is that galaxies have formed hierarchically, meaning that galaxies grew through mergers and accretion. Therefore, many of these recoiled remnants should have formed over the age of the Universe. As the kick velocity depends on the initial binary parameters, a determination of the kick velocity distribution provides information about the properties of the SMBHs at merger. These properties are interesting, as for example the spin distribution of SMBHs provides information on their formation history [Berti and Volonteri, 2008]. Furthermore, the observation of a recoiled SMBH would provide direct confirmation that these objects indeed merge, which is a major assumption underlying the LISA space mission.

As SMBH mergers are expected to happen in the nuclei of (colliding) galaxies, the binary is surrounded by stars. Following the recoil kick, only the stars that are sufficiently close to the remnant will remain bound and follow the recoiling SMBH as it is displaced from the galactic center. The effects of this kick on the surrounding stellar population have been first studied in [Komossa and Merritt, 2008, Merritt et al., 2009, O'Leary and Loeb, 2012], and more recently in [Akiba and Madigan, 2023]. These are the main references for what follows.

When a SMBH of mass $M_\bullet$ is kicked out of the galactic center with a kick velocity V_k, most of the stars that remain bound lie within a radius

$$r_k \equiv \frac{GM_\bullet}{V_k^2} \approx 0.43 \left(\frac{M_\bullet}{10^8 M_\odot}\right) \left(\frac{V_k}{1000 \text{ km s}{-}1}\right)^{-2} \text{ pc}\,, \tag{3.1}$$

which is a good estimate of the initial extent of the HCSC. This shows that these clusters have initial sizes that can vary between $\sim 10^{-3}$ pc and several pc. The latter corresponds to the typical scale of a globular cluster (GC) [Mau et al., 2019].

The SMBH also has a so-called *influence radius*

$$r_{\text{infl}} \equiv \frac{GM_\bullet}{\sigma^2} \approx 10.8 \left(\frac{M_\bullet}{10^8 M_\odot}\right) \left(\frac{\sigma}{200 \text{ km s}{-}1}\right)^{-2} \text{ pc}\,. \tag{3.2}$$

The 1-dimensional velocity dispersion σ of the galactic bulge is related to the mass of the central SMBH. This is reflected in the empirically determined $M-\sigma$ relation[1] [McConnell and Ma, 2013]

$$\frac{M_\bullet}{10^8 M_\odot} = 2.1 \left(\frac{\sigma}{200 \text{ km s}^{-1}}\right)^{5.64}\,. \tag{3.3}$$

[1]Note that we used a more recent version of this relation than the one used in [Merritt et al., 2009], which was obtained in [Ferrarese and Ford, 2005]. Both versions of the $M-\sigma$ relation are obtained from mixed samples of spiral and elliptic galaxies.

In the case that the kick is large enough for the cluster to displaced from the galaxy core ($V_k \gtrsim 0.4V_{\rm esc}$, where the latter is the *escape velocity* of the galaxy [Gualandris and Merritt, 2008]), r_k is small compared to the influence radius. To this level of approximation, the stars essentially move in the point-mass potential of the SMBH, both before and after the kick. This allows us to calculate the post-kick distribution of stars from the distribution before the merger: moving to the SMBH frame of reference, the orbits of the stars are altered as if they receive an instantaneous kick V_k in the opposite direction of the recoiling SMBH. [Merritt et al., 2009]

3.1.1 Stellar distribution

Before the kick, the stellar population is assumed to have a power law density profile

$$\rho(r) = \rho(r_\bullet)\left(\frac{r}{r_\bullet}\right)^{-\gamma}, \tag{3.4}$$

where $r_\bullet$ is a normalization radius and the exponent is usually set to $\gamma = 1.75$. This is more commonly known as the Bahcall-Wolf cusp [Bahcall and Wolf, 1976], which describes the distribution of stars around a central SMBH. We will choose the normalization radius so that the total stellar mass contained within a sphere of this radius is equal to twice the mass of the central SMBH, i.e. $M(r < r_\bullet) = 2M_\bullet$. This radius is expected to be on the order of $r_{\rm infl}$.

After the recoil kick, the density profile is largely unchanged at radii $r \lesssim r_k$, but strongly truncated beyond this. It is well described by the Dehnen profile

$$\rho(r) = \frac{(3-\gamma)M_D}{4\pi r_D^3}\left(\frac{r}{r_D}\right)^{-\gamma}\left(1+\frac{r}{r_D}\right)^{\gamma-4} \tag{3.5}$$

for $1 \lesssim \gamma \lesssim 2$. Here M_D is the total stellar mass that is retained after the kick, and $r_D = 2r_k$. This density profile is shown in Figure 3.1.

We thus need to know what mass in stars remains bound after the kick. [Merritt et al., 2009] show that the bound mass M_b is given by

$$\frac{M_b}{M_\bullet} = F_1(\gamma)\left(\frac{r_k}{r_\bullet}\right)^{3-\gamma}, \tag{3.6}$$

where $F_1(\gamma)$ is a *form factor*, which can be well approximated by

$$F_1(\gamma) = 11.6\gamma^{-1.75}. \tag{3.7}$$

It is clear that $r_\bullet$ needs to be determined in order to use (3.6).

Determination of $r_\bullet$

We model some observational candidates in the Milky Way and its halo in Sec. 3.5. Therefore, we will focus on SMBHs with masses smaller than that of Sgr A*, which has

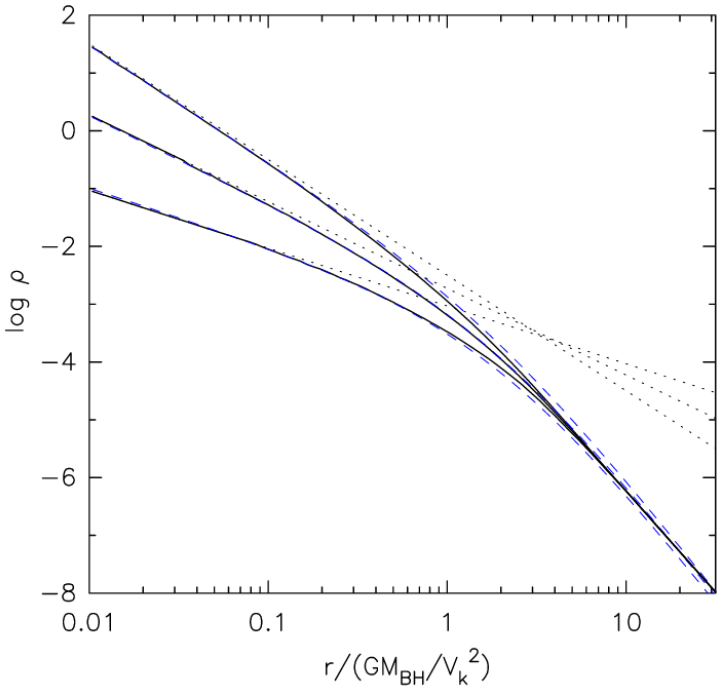

Figure 3.1: Steady-state, spherically symmetrized density profiles of the bound population after the kick for $\gamma = (1, 1.5, 2)$. The dotted lines show the pre-kick densities; the dashed blue lines are Dehnen model (3.5) fits. Figure taken from [Merritt et al., 2009].

a mass of $\sim 4 \cdot 10^6 M_\odot$ [Eckart and Genzel, 1997, et al., 2022, Ghez et al., 1998]. As mentioned above, some loss-cone repopulation mechanism is required to overcome the final parsec problem. For the SMBH mass range that we consider, *collisional loss-cone repopulation* is considered in [Merritt et al., 2009] to give an estimate for the scale radius $r_\bullet$. In this framework, depleted orbits can be repopulated by gravitational scattering between stars, as the two-body relaxation time in the pre-kick nucleus is sufficiently short for these SMBHs. They find that the pre-kick density can be approximated as

$$\rho(r) = \begin{cases} \rho_\bullet \left(\frac{r}{r_\bullet}\right)^{-7/4} & 0 \lesssim r \lesssim r_\bullet \\ \rho_\bullet & r_\bullet \lesssim r \lesssim r_{\rm infl} \end{cases} , \tag{3.8}$$

where $r_\bullet \approx 0.2 r_{\rm infl}$. If we now use (3.6), we find that

$$\begin{aligned} \frac{M_b}{M_\bullet} &\approx 1.3 \left(\frac{G M_\bullet}{r_{\rm infl} V_k^2}\right)^{5/4} \left(\frac{\rho_0 r_{\rm infl}^3}{M_\bullet}\right) \\ &\approx \left(\frac{\sigma}{V_k}\right)^{5/2} \left(\frac{M_{\rm core}}{M_\bullet}\right) , \end{aligned}$$

where we defined $M_{\rm core} \equiv \rho_0 r_{\rm infl}^3$. The ratio $M_{\rm core}/M_\bullet$ is of order unity[2], such that

$$\frac{M_b}{M_\bullet} \approx \left(\frac{\sigma}{V_k}\right)^{5/2} \approx 0.02 \left(\frac{\sigma}{200 \text{ km s}^{-1}}\right)^{5/2} \left(\frac{V_k}{1000 \text{ km s}^{-1}}\right)^{-5/2} , \tag{3.9}$$

[2]This statement is made in Merritt et al. [2009]. However, this can be calculated exactly given (3.8), and we find that the ratio is ≈ 33. This also leads to the prefactor in (3.9) being 0.58. We will, however, stick to the original prefactors, but it shows the approximate nature of these estimates.

Combining (3.3) and (3.9), we find

$$\frac{M_\bullet}{10^5 M_\odot} \approx 6.5 \left(\frac{V_k}{1000 \text{ km s}^{-1}}\right)^{1.73} \left(\frac{M_b}{1000 M_\odot}\right)^{0.69} , \tag{3.10}$$

which we will use in Sec. 3.5.

Post-kick evolution

Shortly after the kick, the stellar distribution is well described by the Dehnen density profile (3.5). The stellar population will now continue to evolve via two-body relaxation. Therefore, gravitational scattering will drive stars into the tidal distruption sphere of the SMBH, with radius

$$R_{\text{TDE}} = \left(\frac{M_\bullet}{M_*}\right)^{1/3} R_* . \tag{3.11}$$

However, - assuming the kick moved the HCSC out of the galactic nucleus - there is no reservoir of stars at the sphere of influence to replace those that are lost. This means that the density of stars in the HCSC will steadily drop. The rate at which this happens is determined by the rate of tidal distruption events. Significant loss of mass within 10^9 years is estimated to be only relevant when [Merritt et al., 2009]

$$\left(\frac{V_k}{1000 \text{ km s}^{-1}}\right)^{3/2} \gtrsim \frac{M_\bullet}{10^7 M_\odot} . \tag{3.12}$$

The two different cases are illustrated in Figure 3.2. These density profiles are obtained through a Fokker-Planck equation, to which we come back in Sec. 3.3.

3.2 Observational characteristics

Having described some of the basic properties of a HCSC, we now move on to the question: can we see these putative systems? So far, no definite detection has been made. We review some observational aspects of HCSCs in Sec. 3.2.1, and consider the addition of a smBH-component to the cluster in Sec. 3.2.2. We later focus on some specific candidates in Sec. 3.5.

3.2.1 Distinguishing HCSCs from other systems

We have already seen that the size of a HCSC is on the order of that of a GC or smaller. Furthermore, the luminosity is expected to be similar or smaller as well. Therefore, it is unclear at first how we can hope to distinguish these two different systems. Luckily, a major difference is expected in the velocity dispersion of the stars.

The Keplerian velocity of an object moving in the point-mass potential of the SMBH at radius r is given by

$$v_K = \sqrt{\frac{GM_\bullet}{r}} \approx 21 \left(\frac{M_\bullet}{10^5 M_\odot}\right)^{1/2} \left(\frac{r}{1 \text{ pc}}\right)^{-1/2} \text{ km s}^{-1} . \tag{3.13}$$

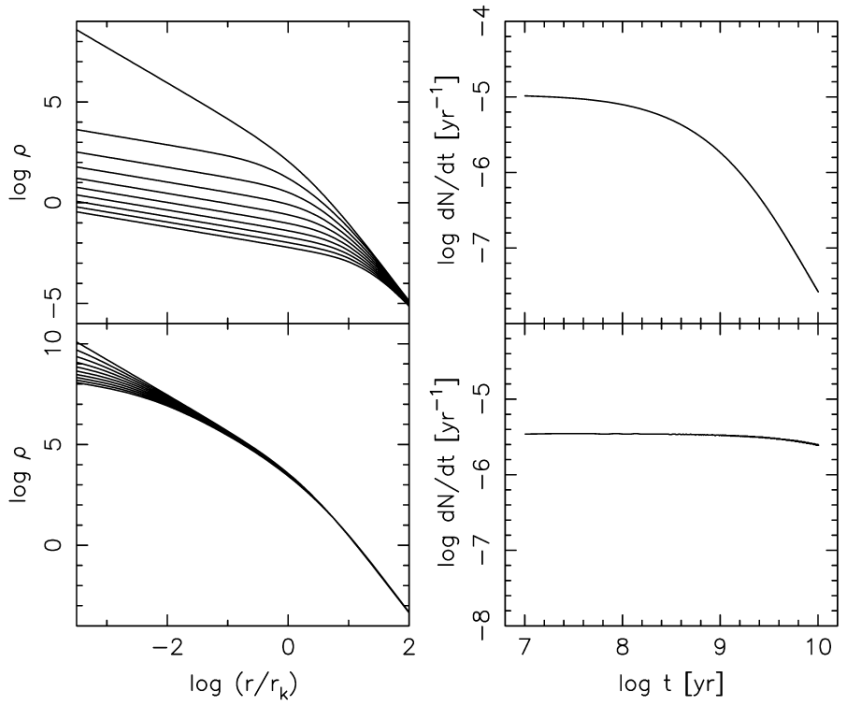

Figure 3.2: Evolution of the *(left)* density profile and *(right)* loss rate, for two different HCSCs. The top row shows $(M_\bullet, M_b) = (3 \cdot 10^6, 7 \cdot 10^3) M_\odot$, and the bottom row shows $(M_\bullet, M_b) = (3 \cdot 10^7, 1 \cdot 10^5) M_\odot$. In both cases, $V_k = 10^3$ km s^{-1}. The different lines correspond to time increments of 1 Gyr. [Merritt et al., 2009]

At r_k, this is simply equal to V_k, so that the characteristic speed of the stars scales as V_k. Therefore, we define a new form factor[3] $F_3(\gamma)$ such that

$$\sigma_{\rm obs} = F_3(\gamma) V_k \,, \tag{3.14}$$

where $\sigma_{\rm obs}$ is the measured velocity dispersion of the stellar population after the kick. This implies that, if γ is known - or the dependence of F_3 on γ is weak - the kick velocity can be extracted by measuring the velocity dispersion of the stars in the HCSC. This form factor is estimated in [Merritt et al., 2009] as

$$\ln F_3 = -2.17 + 0.56\gamma \,. \tag{3.15}$$

Therefore, assuming the Bahcall-Wolf cusp, we find that

$$\sigma_{\rm obs} \approx 0.30 V_k \,. \tag{3.16}$$

Therefore, we expect velocity dispersions of HCSCs to be on the order of $\mathcal{O}(10) - \mathcal{O}(10^2)$ km s^{-1} for typical systems and kicks. This is significantly higher than it is for GCs, where it is 1 or 2 orders of magnitudes lower.

There are more signatures that could signal a HCSC candidate. For example, they can have a large velocity offset with respect to other objects in their local environment. Additionally, TDE flares in star clusters [Komossa and Merritt, 2008] can indicate the presence

[3]This one is called F_3 for consistency with [Merritt et al., 2009], where another form factor F_2 is defined as well.

of a SMBH. Furthermore, gas can remain bound to the central SMBH as well. This gas can be accreted on the timescale of several million years, causing the recoiled SMBH to be seen as a short-lived active galactic nucleus (AGN) [O'Leary and Loeb, 2012]. Afterwards, the SMBH will only be visible if it passes through a gas-rich region. AGNs with a spatial offset from the center and / or Doppler-shifted broad emission lines have already been detected, which could indicate that the central SMBH has received a kick (e.g. [Hogg et al., 2021, Komossa et al., 2008]). However, the SMBH is not always accreting, and alternate explanations are difficult to rule out. [Akiba and Madigan, 2023]

Even though HCSCs may resemble GCs or ultra-compact dwarf galaxies (UCDs), they can be distinguished by either their larger velocity dispersion or greater compactness. Figure 3.3 shows the parameter space for HCSCs under the model we considered in Sec. 3.1.1 (blue hatched area), and compares it to GCs and UCDs. The effective radius $r_{\rm eff}$ is a measure of the scale of the HCSC, and is defined as the radius that contains one-half of the stellar mass in projection. The figure shows that, for a large part of the parameter space at least, HCSCs can be distinguished from these mimickers.

The colours of HCSCs have already been studied extensively as well [Lena et al., 2020, Merritt et al., 2009]. At a given time, the luminosity of the HCSC will be dominated by red giants, but due to the contribution of the main-sequence stars the overall colours of the cluster will be bluer than those of individual giants. Also, as the stars likely originated in the galactic center, the metallicity is likely to be larger than that of a typical low-metallicity GC. They also should appear redder than low-metallicity GCs with comparable ages $\gtrsim$ 1Gyr.

So, HCSCs show distinct features that allow for the identification of their nature. Estimates have been made of the number of systems that we should be able to see. Using over 1000 merger tree histories of the Milky Way, [O'Leary and Loeb, 2009] estimated that $\gtrsim$ 100 BHs with $M_\bullet \gtrsim 10^4 M_\odot$ should be in the halo today, surrounded by compact star clusters that are about 1% of the BH mass. Later, they performed performed a systematic search for candidates in the *Sloan Digital Sky Survey*, and identified $\sim$ 100 photometric candidates, that require follow-up spectroscopy to accurately determine their nature [O'Leary and Loeb, 2012]. However, an all-sky search of the Milky Way halo requires enormous amounts of observation time. Therefore, it may be advantageous to look for HCSCs in neighbouring galaxies. As an example, around 100 HCSCs should be observable in the Virgo cluster, of which only a few may be bright enough to confidently confirm their nature though [Merritt et al., 2009].

3.2.2 The addition of a smBH component

As outlined in the previous sections, there is a good idea of what these putative HCSCs should look like. However, so far all of this research is based on modelling of the stellar population and gas. We argue in this section that it could be essential to include a population of compact remnants in these models as well, as it can significantly alter the scale of the cluster. We specifically consider a population of smBHs, and describe models in Sec. 3.3 that we apply to some observational candidates in Sec. 3.5.

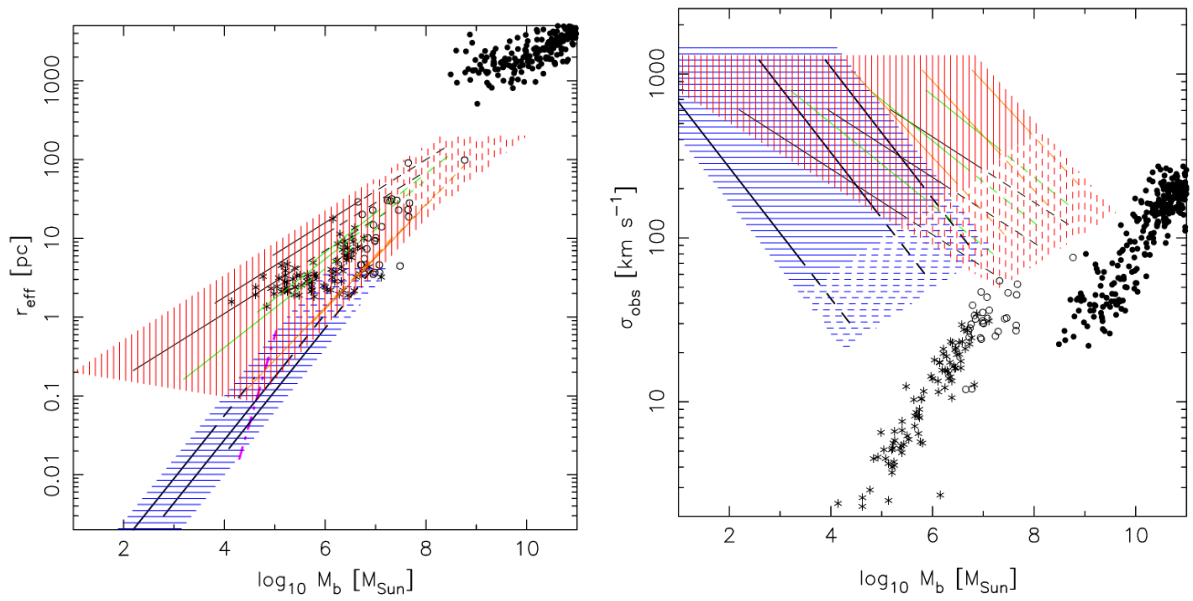

Figure 3.3: *(left)* Effective radius and *(right)* observed velocity dispersion against bound stellar mass for HCSCs. The blue hatched area shows the parameter space based on the collisional loss-cone repopulation model (as discussed in Sec. 3.1.1). Solid lines extend to a maximum $r_{\rm eff}$ based on the assumption that $V_k \geq 4.5\sigma$ (escape from the galaxy) while dashed lines correspond to the weaker condition $V_k \geq 2\sigma$ (escape from the galaxy core). HCSCs to the left of the dash-dotted (magenta) line are expected to expand appreciably over their lifetime (see (3.12)). Data points are from [Forbes et al., 2008]: filled circles correspond to elliptical galaxies, open circles to UCDs, and stars to GCs. The red hatched area corresponds to an alternative loss-cone repopulation model for $M_\bullet \gtrsim 10^7 M_\odot$. A treatment, as well as a description of the other lines in the figures, can be found in [Merritt et al., 2009].

Earlier work on GCs has shown that a population of smBHs can significantly increase the scale[4] of the cluster [Mackey et al., 2008, Merritt et al., 2004]. The orbits of the smBHs decay due to dynamical friction, so that they sink to the cluster center, heating the stellar population and turning a cusp into a core[5]. The simulations of [Mackey et al., 2008] show that core expansion is only induced when the smBH population in the cluster has accumulated in a sufficiently dense central subsystem that smBH binaries are created. These binaries are the catalyst for core expansion, as the interactions of the binaries lead to smBH scattering. The time of formation of the first smBH binaries is on the order of half a Gyr, but is very sensitive to the natal recoil kicks that the smBHs receive [Atri et al., 2019, Jonker and Nelemans, 2004]. Once binaries form and expansion begins, the rate is dependent on the number of smBHs. The rate of expansion is also expected to decrease with time, as the core expands and smBHs get ejected, resulting in a decreasing interaction rate.
The simulations of [Mackey et al., 2008] also show that this effect of core heating cannot be mimicked by a retained population of e.g. NSs. The presence of a smBH population can be observationally tested, as they may act as X-ray and / or GW sources. Furthermore, the smBHs should increase the velocity dispersion of the stars.

Observational support for this idea can be found in e.g. [Gieles et al., 2021]. The paper considers Palomar 5, one of the sparsest clusters in the Galactic Halo: it is unusually large, with a half-light radius on the order of 20 pc, and a mass on the order of $10^4 M_\odot$. Furthermore, the cluster shows tidal tails. With N-body simulations, the authors show that both features can be explained if there is a smBH population present[6], about 20% of the present-day cluster mass. It probably formed with a smaller smBH fraction of a few percent, but stars were lost at a higher rate than smBHs, increasing the fraction. Their best-fitting model had an initial mass of $\sim 10^5 M_\odot$ which means that the cluster has lost over 90% of its mass today. The present smBH population consists of 124 smBHs with an average mass of $17.2 M_\odot$. This corresponds to a BH fraction that is too large for what one would expect from a canonical stellar initial mass function, and is the result of an efficient loss of stars, while the smBHs are largely retained as they reside at the center. Their smBH hypothesis is further supported by the fact that the predicted and observed velocity dispersion agree (both on the order of ~ 550 m s^{-1}), and that their models without a smBH population require a large degree of fine-tuning.

So, it seems likely that a smBH population can accelerate the expansion of a GC. Therefore, we want to include smBHs in the simulations of HCSCs as well, and see if a similar effect is obtained. It should be noted that simulations show that a central intermediate-mass BH can already drive cluster expansion [Baumgardt et al., 2004], but we want to investigate whether the addition of a smBH population can drive the expansion to even higher rates. We show that this is indeed the case in Sec. 3.4. Figure 3.4 shows the effec-

[4] [Mackey et al., 2008] show that mass-loss due to rapid stellar evolution in a cluster which is mass-segregated or otherwise centrally concentrated can also drive expansion of a GC. This process operates only over the first ~ 100 yr of the cluster's life, after which the smBH heating takes over.

[5] A *cusp* means that the density steeply increases towards the center of a star / dark matter cluster, whereas a *core* refers to a nearly constant density at the center. Observations and computer simulations do not agree very well on whether e.g. dark matter is distributed along a core or cusp in the inner part of galaxies, which is known as the *core/cusp problem* (see e.g. [De Blok, 2010]).

[6] For clarity: the authors do *not* model a HCSC, i.e. they do not consider a central massive BH.

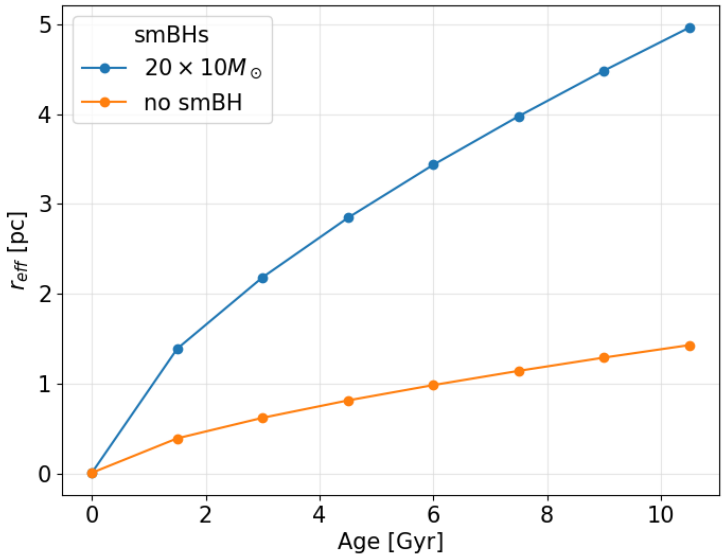

Figure 3.4: The influence of a smBH population on the half-light radius of a HCSC with $M_\bullet = 10^5 M_\odot$ and $M_b = 1000 M_\odot$, as function of time. The blue line corresponds to an added population of 20 smBHs of $10 M_\odot$, whereas the orange line does not include such a population. This shows that a smBH population can indeed accelerate the expansion of a HCSC.

tive radius, a measure of the scale of the cluster, as a function of time for a HCSC with $M_\bullet = 10^5 M_\odot$ and $M_b = 1000 M_\odot$, with and without the inclusion of a smBH population. We come back to this in more detail in Sec. 3.4.

Observational relevance

Over the recent years, a number of sparse, old, faint stellar clusters have been discovered, e.g. [Gieles et al., 2021, Hamren et al., 2013, Kim et al., 2016, Mau et al., 2019, 2020]. Their sizes are comparable to those of GCs, but their luminosities can be hundreds of times fainter. Estimates have been made for their evaporation timescales, i.e. the timescale over which star escape the system due to two-body relaxation [Koposov et al., 2007, Meylan and Heggie, 1997], and have found to be as low as $\sim$ 3 Gyr [Mau et al., 2020] or even $\sim$ 600 Myr [Kim et al., 2016]. These timescales are short compared to their ages, estimated as $\sim$ 10 Gyr, meaning that these clusters cannot have persisted in their current state throughout their lives.

A possible explanation would be that there is a large influx of these systems, but this is not observed. Currently, it is thought that a large portion of these faint clusters are accreted with merger events in the formation of the Milky Way [Massari et al., 2019].

However, the presence of a central SMBH can increase the evaporation timescale signifi-

cantly. Following [Bahcall and Wolf, 1976], the relaxation timescale of a HCSC is

$$t_R = \frac{3(2\pi\sigma^2)^{3/2}}{32\pi^2 G^2 m_*^2 n_* \ln\Lambda}\,, \tag{3.17}$$

which depends on the average stellar mass $m_\star$, the number density of stars n_* at $r_{\rm infl}$ and the so-called *Coulomb logarithm* $\ln\Lambda$, to which we come back in Sec. 3.3.2. As σ is expected to scale as the Keplerian velocity (3.13), we find that this relaxation time is expected to scale as $t_R \propto M_\bullet^{3/2}$, assuming the other parameters remain fixed. Assuming a SMBH mass of $M_\bullet = 10^5 M_\odot$, and taking some typical values $\sigma \sim 10$ km s^{-1}, $m_\star \sim 1 M_\odot$, $n_\star \sim 100$ pc^{-3} and $\ln\Lambda \sim 10$ (see Sec. 3.3.2 and 3.4), we find that that $t_R \sim 8$ Gyr, which is an order of magnitude larger than the values in the previous paragraph. The evaporation timescale is about 10-100 times this relaxation timescale, meaning that the former also increases by an order of magnitude.

The conclusion is that the presence of a central SMBH in these clusters could explain their observational properties, as it would allow for a longer evaporation timescale compared to the case where the SMBH is absent. However, the effective radius of HCSCs with a SMBH this massive normally does not become much larger than $\gtrsim 1$ pc, which does not agree with the observed sizes of these faint halo clusters. However, as Figure 3.4 shows, the addition of a smBH component can increase the expansion of the HCSC, such that its size *does* match observations. A smBH population therefore allows us to cover a much larger parameter space for HCSCs, which is now large enough that it could potentially provide a realistic model for some of these faint halo clusters.

A determination of the velocity dispersion of these faint halo clusters could shed a light on their nature, as GCs have expected velocity dispersions $\lesssim 1$ km s^{-1}, but as argued above HCSCs can have a velocity dispersion that is an order of magnitude larger.

3.3 Modelling

In this section, we briefly review N-body (Sec. 3.3.1) and Fokker-Planck (Sec. 3.3.2) simulations, the main two ways to model these clusters. Our simulation tool, `PhaseFlow`, is based on the latter, and is discussed in Sec. 3.3.3. We discuss in detail how we add the influence of a smBH population. The results are discussed in Sec. 3.4. Unless otherwise stated, most of the material in Sec. 3.3.1 and 3.3.2 can be found in [O'Leary and Loeb, 2012].

3.3.1 N-body simulations

Perhaps the most sensible thing to do when modelling a cluster is to keep track of the position and velocity of every single star, and use the equations of motion to determine the time evolution of the system. These are called N-body simulations, and have been used extensively to model GCs [Giersz and Heggie, 1996, Mackey et al., 2008] and HCSCs [Akiba and Madigan, 2023, Baumgardt et al., 2004, O'Leary and Loeb, 2012]. However, this requires keeping track of the gravitational forces between every pair of stars, meaning

that the computational costs increase quadratically with increasing number of stars.

The N-body simulations of [O'Leary and Loeb, 2012] considered a Bahcall-Wolf cusp around a $10^4 M_\odot$ SMBH. The number of stars considered was such that the total stellar mass in the cusp equals twice that of the SMBH. They considered models where all stars have the same mass, as well as models with more realistic mass functions. Using a kick velocity of ~ 100 km s^{-1}, they find that approximately 600 $M_\odot$ of stars remain bound to the SMBH immediately after the kick. This is comparable to what we find using (3.10). They find that the number of stars decreases according to $N_*(t) \propto t^{-1/2}$ after $\sim 10^7$ yr. Approximately 40% of the stars are ejected from the cluster and another 40% of the stars are tidally disrupted by the BH. The cluster also begins to expand: they find that radii that enclose a fixed number of stars scale as $r_N \propto t^{2/3}$.

After evolving their simulations for ~ 10 Gyr, they find that the distribution of stars is well described by a power-law density profile with $\gamma \lesssim 2.15$ (see Figure 3.5). Regular relaxation seems to determine the shape and the expansion of the cluster, whereas strong encounters between stars and tidal distruption event (TDE)s from resonant relaxation determine the final number of stars in the cluster. They argue that the effects of WDs and NSs should be comparable to those of stars, and therefore do not account for them separately. However, they point out that smBHs could have a significant influence on the evolution of the cluster, although they have not included them in their simulations.

More recently, [Akiba and Madigan, 2023] have used N-body simulations to derive post-kick surface density and velocity maps of HCSCs to highlight what influence the kick has on the star distribution around the recoiling SMBH.

3.3.2 Fokker-Planck equation

The disadvantage of N-body simulations is their enormous computational cost: for example, a typical simulation from [O'Leary and Loeb, 2012] took up to one month on a single core of the Odyssey Cluster at Harvard University. Their simulations focussed on a $10^4 M_\odot$ SMBH, but as increasing the BH mass would also increase the number of stars that remain bound, simulations for more massive BHs would take even longer. In order to overcome this problem, approximate methods have been developed as well.

One of the options is to consider the evolution of a *distribution function* $f(E)$ of stars, on which we can make some assumptions. Some of the simplifications that can be made are the assumption of isotropy, or averaging this distribution function over an orbit. [Bahcall and Wolf, 1976, 1977] derived a Fokker-Planck (FP) equation that describes the diffusion of stars by gravitational scattering in the gravitational well of a central SMBH:

$$\frac{\partial g(x,\tau)}{\partial \tau} = -x^{5/2}\frac{\partial}{\partial x}Q(x) - R_{\rm lc}(x)\,. \tag{3.18}$$

In this equation, x, τ are dimensionless quantities defined as $x = -E/(m_*\sigma^2)$, where m_* is the average stellar mass, E is the orbital energy and $\tau = t/t_R$ (with t_R the relaxation time (3.17) of the cluster). The function $g(x,\tau)$ is the dimensionless distribution function of stars, defined as $g(x,\tau) = [(2\pi\sigma^2)^{3/2} n_*^{-1}] f(E)$. $Q(x)$ is the rate at which stars flow to

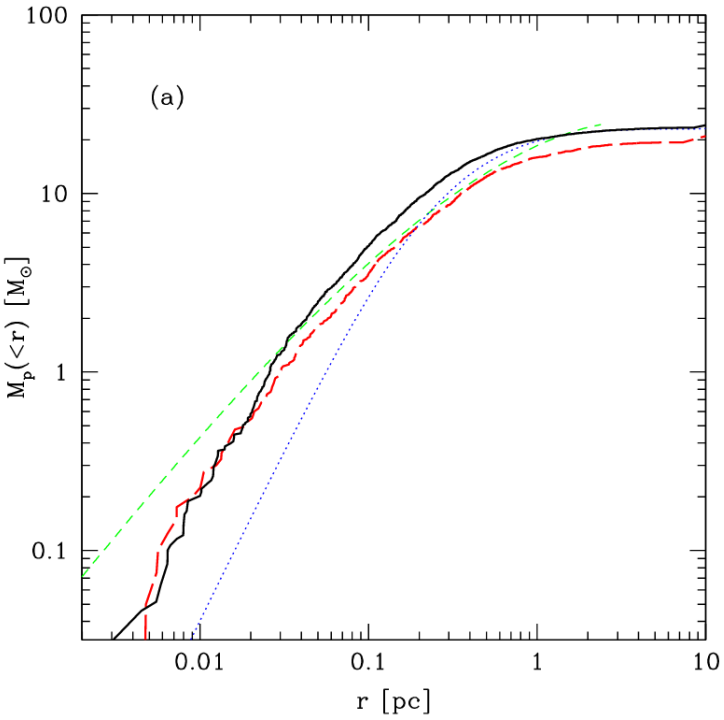

Figure 3.5: Total projected mass in stars within a distance r of a SMBH with $M_\bullet = 10^4 M_\odot$ after $\sim$ 10 Gyr. The long-dashed red line corresponds to a stellar population with a single mass, whereas the solid black line corresponds to a more realistic mass function. The short-dashed green line and dotted blue line correspond to results of Fokker-Planck simulations: the former does not include the sinks (3.24) and (3.25), and is rescaled to have the same half-mass radius as the N-body simulations, whereas the latter includes these sinks and is not rescaled. Figure taken from [O'Leary and Loeb, 2012]

higher energies, and $R_{\rm lc}(x)$ is the tidal disruption rate of stars that diffuse into the SMBH loss cone[7] via regular two-body relaxation. They are given by

$$Q(x) = \int_{-\infty}^{x_{\rm TDE}} {\rm d}y \, [\max(x,y)]^{-3/2} \left(g(x) \frac{\partial g(y)}{\partial y} - g(y) \frac{\partial g(x)}{\partial x} \right) , \tag{3.19}$$

$$R_{\rm lc}(x) \approx \frac{2g(x)^2}{\ln\left(x/x_{\rm TDE}\right)} , \tag{3.20}$$

where $x_{\rm TDE} \approx (M_\bullet/m_*)^{-1/3} r_{\rm infl}/R_*$ is the maximum specific energy of a star before tidal disruption.

Some assumptions are made to derive (3.18). First of all, it is assumed that the distribution of stars is adequately represented by a single-particle distribution function that is spherically symmetric in space and approximately isotropic in velocity space. Furthermore, the average stellar mass is assumed small compared to $M_\bullet$. Finally[8], it is assumed that the predominantly important collisions are due to small-angle scattering.

The Coulomb logarithm

One of the parameters in the FP equation (3.18) is the Coulomb logarithm $\ln\Lambda$, which enters through (3.17). This parameter is somewhat ambiguous, as it arises from a cutoff in an integral [Bahcall and Wolf, 1976]. At some point, in the calculation of the rate $R(E,t)$ at which stars are scattered into a region of energy greater than E by two-particle collisions, they find that

$$R(E,t) \propto \int \frac{{\rm d}E_a}{|E_a - E|} H(E_a) , \tag{3.21}$$

where E is minus the stellar energy per unit mass (and E_a is this quantity for star a) and H is a certain function. This integral formally diverges both when $E_a \to E$ and when $E_a \to \infty$. The solution is to introduce a cutoff for both cases, defining

$$\Delta_{\rm min} \equiv E_{a,{\rm min}} - E ,$$
$$\Delta_{\rm max} \equiv E_{a,{\rm max}} - E \approx E_{\rm max} .$$

These cutoffs must be so that all the physically relevant cases are included in the integral, but the divergences at the singularity and infinity are no longer included. The lower limit cutoff results from the requirement that the collision time at the maximum effective impact parameter, $b_{\rm max}$, is smaller than the orbital period of the bound star. The upper limit cutoff is chosen such that the small-angle approximation remains valid, and therefore corresponds to a minimum impact parameter $b_{\rm min}$. [Bahcall and Wolf, 1976] estimate that

$$\Delta_{\rm min} \sim \frac{m_*}{M_\bullet} E ,$$
$$E_{\rm max} \sim E ,$$

[7] The SMBH loss cone is roughly speaking the collection of orbits that end up in the capture sphere of the SMBH. See [Merritt, 2013] for a comprehensive explanation.

[8] We note that in the original paper [Bahcall and Wolf, 1976] it is also assumed that $M_\bullet$ is smalled compared to the cluster core mass. This does not seem to be fullfilled in the case of HCSCs: typically $M_b \ll M_\bullet$. Dr. Eugene Vasiliev has pointed out that this should not be a problem, and possible quantitative differences are accounted for in the `PhaseFlow` code that we use (see Sec. 3.3.3).

such that they can approximate the integral in (3.21) as

$$\int \frac{\mathrm{d}E_a}{|E_a - E|} H(E_a) \approx 2H(E) \ln \Lambda \,,$$

where

$$\ln \Lambda = \ln \left(\frac{M_\bullet}{m_*} \right) \tag{3.22}$$

is the so-called Coulomb logarithm.

The quantity (3.22) is called the Coulomb logarithm because it first appeared in a similar problem in plasma physics, concerning the scattering of charged particles under influence of mutual Coulomb forces. Similarly, one needs to approximate an integral over the impact parameter b of the form

$$\int \frac{\mathrm{d}b}{b} \approx \ln \Lambda \,,$$

where the cutoff on both sides is now determined by a minimal and maximal effective impact parameter. It is custom to take the lower cutoff to correspond to the impact parameter of a strong encounter that would lead to 90° deflection, and the maximal impact parameter on the order of the scale of the system. The maximum impact parameter is also often taken to be the Debye shielding radius [Krommes, 2019].

The Coulomb logarithm already appeared earlier in the modelling of GCs. In this case, it is usually taken of the form

$$\ln \Lambda \approx \ln \gamma N \,, \tag{3.23}$$

where $\gamma \approx 0.4$ for equal mass stars [Spitzer and Hart, 1971] and $\gamma \approx 0.02$ for a mass spectrum [Giersz and Heggie, 1996]. The same formula has also been used when modelling stars around a SMBH, in the case that the number of stars is on the order of $10^5 - 10^6$ [Vasiliev et al., 2015]. In this case, the formulae (3.22) and (3.23) give comparable results.

So, the Coulomb logarithm clearly reflects some of the assumptions that are made in the process, and is not precisely defined. This means that it is hard to confidently assign it a value. However, as the limiting cutoffs appear in a logarithm, the final value is not very sensitive to small changes in the cutoff. We will however use the formula (3.22) in what follows, as recent papers take this approach as well [O'Leary and Loeb, 2012, Vasiliev, 2017] and it is the one derived for the case of a central SMBH.

To take the smBH population into account, we extend (3.22) to represent the average mass of stars *and* smBHs, as the latter also partake in the gravitational scattering. It should be noted that changing the Coulomb logarithm affects the observables that we consider in the next sections (see Figure 3.11). For the models that we consider, $\ln \Lambda \sim 11$.

Two additional sink terms

Over the years, increasing layers of complexity have been added to the one-dimensional FP equation (3.18). [O'Leary and Loeb, 2012] complemented their N-body simulations

(discussed in Sec. 3.3.1) with FP simulations based on (3.18) with the addition of two more sink terms.

First of all, they include a sink related to the tidal disruption rate of stars that fall into the SMBH loss cone due to resonant relaxation, given by [Hopman and Alexander, 2006]

$$R_{\rm rr}(x) \approx \chi \frac{g(x)}{\tau_{\rm rr}(x)} \,. \tag{3.24}$$

Resonant relaxation is the efficient randomization of angular momenta of stars due to the coherent addition of torques between stars. This process can take place on a timescale much shorter than the regular relaxation time, and can lead to an enhanced rate of TDEs. The resonant relaxation timescale can be approximated as $\tau_{\rm rr}(x) \approx 0.0278 x^{3/2}$, and χ is an efficiency factor of order unity.

Secondly, they add the rate at which stars are ejected from the cluster owing to strong encounters

$$R_{\rm ss}(x) = \frac{3}{2\ln\Lambda} x^{5/2} \frac{g(x)}{(x-x_0)^2} \int \frac{g(y){\rm d}y}{(y+x-x_0)^{3/2}} \,, \tag{3.25}$$

based on [Lin and Tremaine, 1980]. In this expression, $x_0 \lesssim 0$ is the negative specific energy required to be ejected. Note that this expression is suppressed by the Coulomb logarithm with respect to the rest of the equation. As a consequence, this sink term turns out to be less important.

Without the additional sink $R_{\rm rr}$, [O'Leary and Loeb, 2012] find that the FP simulations give little mass loss, whereas their N-body simulations indicated that only $\sim 10\%$ of the stars remained bound. Regardless of the inclusion of these two terms, however, the simulations agree on the shape and slope of the density profile of the recoiled clusters. The most suitable parameter value for χ is found to be 0.8. The density profile that results from the FP simulations is also shown in Figure 3.5, both for the case where they include resonant relaxation and the case where they exclude it. It should be noted that the FP simulation does not reproduce the density, as found with the N-body simulations, at the smallest radii very well. They cannot take anisotropy into account, or the preference to deplete eccentric orbits near the SMBH.

Owing to the computational advantages of the FP simulations, [O'Leary and Loeb, 2012] use them to extend the results to more massive SMBHs. The number of stars as a function of time is shown in Figure 3.6, which shows that for heavier SMBHs the mass loss is less significant. Finally, they note that setting the parameter $\chi \gtrsim 5$ greatly increases mass loss, and note that this could represent a cluster with a high concentration of smBHs.

3.3.3 Our models

We base our simulations on the FP equation as described in the previous section. However, we will use an adapted version, as derived in [Vasiliev, 2017]. The argument of the distribution function is changed to be the phase volume, instead of the energy: this is the *volume in phase space enclosed by the energy hypersurface*. There are advantages to this

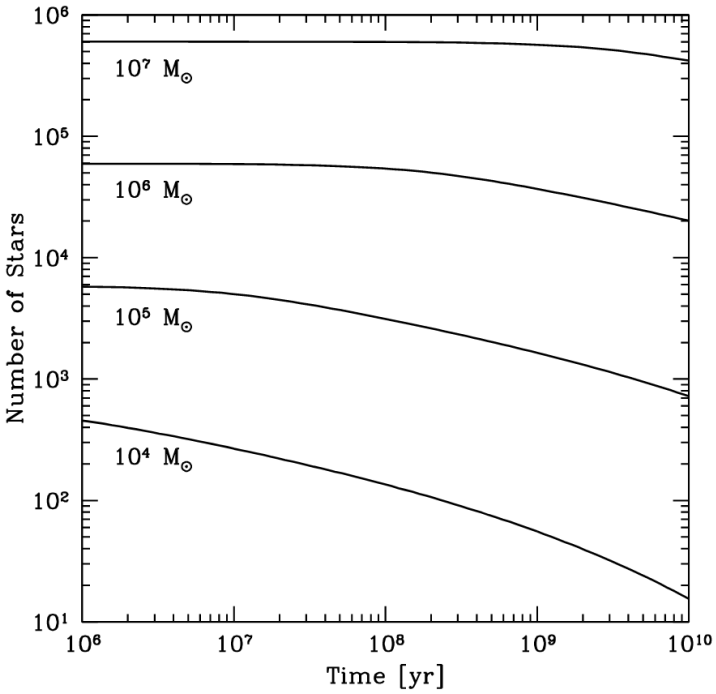

Figure 3.6: Number of stars in a HCSC as a function of time, for different values of $M_\bullet$. The results are obtained with the FP equation (3.18) including the additional sink terms (3.24) and (3.25). Figure taken from [O'Leary and Loeb, 2012]

approach, such as a simplified recomputation of the gravitational potential. The implementation is made public in the `PhaseFlow` code, included in the larger `AGAMA` library for galaxy modelling [Vasiliev, 2019].

The `PhaseFlow` code is capable of handling multiple-component system, a central black hole, loss-cone effects and star formation. However, it does not include a sink term for resonant relaxation (3.24) or strong encounters (3.25). The latter is left out as it seems that the effect is small, e.g. because it is suppressed by the Coulomb logarithm (i.e. by a factor of $\sim 10\%$). Absence of the former is puzzling at first, especially because [O'Leary and Loeb, 2012] found that it needs to be included in order to match their N-body simulations. However, recent works seem to suggest that resonant relaxation is counteracted by relativistic precession of orbits [Alexander, 2017]. At the moment, it is unclear whether this sink term should be included or not[9]: it is not present in the current of `PhaseFlow`, however.

The model we ended up using is the following. We model a SMBH surrounded by a population of stars, according to the post-kick results from [Merritt et al., 2009]. We fix 2 quantities out of $\{M_\bullet, V_k, M_b\}$, and use (3.10) to determine the third one. We then model the stellar population as a population of $M_b/M_\odot$ stars of equal mass $m_* = 1M_\odot$,

[9]Relativistic precession is included in the N-body simulations of [O'Leary and Loeb, 2012], and did not seem to make a big difference. Therefore, it was not included in their FP simulations either. Overall, it remains an open question whether resonant relaxation should be included or not. We thank dr. Eugene Vasiliev and dr. Nicholas Stone for their input and opinion on this matter.

distributed along a Dehnen profile (3.5), with $\gamma = 1.75$, as expected for the Bahcall-Wolf cusp. The scale radius for the Dehnen profile is fixed as $r_D = 2r_k$, and the tidal radius (3.11) is used as the radius at which a star is captured[10] by the central SMBH. We then include different models for a population of smBHs, and evolve this initial setup for ~ 10 Gyr to see the effects of the smBH population.

To model the smBH component, we need to specify similar parameters as we did for the stellar component. We also assign a Dehnen profile to the smBH component, and investigate the influence of the exponent: perhaps the heavier smBH population has already partially segregated towards the center, with possibly a steeper distribution. This is expected when the population is already relatively old before the kick. Similarly, we also investigate the influence of the scale radius of the Dehnen profile, as this could potentially be smaller for the smBH component than it is for the stellar component. Contrary to the stellar component, the capture radius used in the program is

$$\frac{8GM_\bullet}{c^2} \approx 3.8 \cdot 10^{-8} \left(\frac{M_\bullet}{10^5 M_\odot}\right) \text{ pc} \tag{3.26}$$

for black holes. Aside from these parameters, we mostly focus on the influence of changing the number and mass of the smBHs.

Note that we made the crude approximation that all the stars have mass equal to $1M_\odot$. This is because we will evolve the cluster on a timescale that is longer than the lifetime of more massive stars. Therefore, we assume that very massive stars have already exploded, giving rise to the smBH population. Stars that don't give rise to BHs form WDs or NSs, which are also on the order of $\sim 1M_\odot$. The reason for this long evolution time is that we expect HCSCs in the Milky Way to be old, given the fact that major mergers in its formation happened $\gtrsim 8$ Gyr ago [Sotillo-Ramos et al., 2022]. Of course, this is still an approximation, and a detailed simulation would include stars of all masses, and track their evolution.

3.4 Results

In this section, we summarize some general results obtained for a fiducial HCSC, by exploring the possible parameter space for the smBH population. Afterwards, we discuss specific models with the goal of resembling some specific observational candidates in Sec. 3.5. In this first treatment, we are mostly interested in the projected half-light radius (pHLR) of the final stellar distribution and the number of stars remaining, because these can be compared to existing measurements.

The output of `PhaseFlow` gives us the enclosed mass as function of the radius. We can thus extract the radius within which half of the total mass is contained, which is approximately equal to the half-light radius as all the stars have the same mass. However, to make

[10] When a star is captured by the SMBH, 1% of its mass is added to the SMBH mass. Naively, tidal disruption events would contribute about 50% of the stellar mass to the SMBH. We have checked that changing this parameter does not influence the final resutls significantly.

contact with observations in the next section, we would like to know the *projected half-light radius*: this is the radius of the circle on the sky that contains half the light. This means we need to project the resulting mass distribution onto two dimensions. Denote the projected radius with R, and the spherical radius with r. The contained mass as function of the spherical radius is denoted with $M_3(r)$, and the projected mass as $M_2(R)$. Now, the projected mass within a radius R is equal to the sum of the mass within a sphere of radius $r = R$ and the contributions from higher spherical radii that are "in front of" and "behind" this sphere. So, we find that

$$M_2(< R) = M_3(< R) + \int_R^\infty \frac{\mathrm{d}M}{\mathrm{d}r} \cdot \frac{\Omega(r)}{4\pi} \mathrm{d}r \,.$$

In this expression, $\Omega(r)$ denotes the solid angle corresponding to the part of the sphere with radius r that is either in front of or behind the sphere with radius R. Taking $\theta = 0$ to point in our direction, some trigonometry tells us that

$$\Omega(r) = 2 \cdot 2\pi \int_0^{\theta^*(r)} \sin\theta \mathrm{d}\theta \,, \tag{3.27}$$

where $\sin\theta^*(r) = \frac{R}{r}$, and the factor 2π comes from the azimuthal angle ϕ. Working out the integral gives us the result

$$M_2(< R) = M_3(< R) + \int_R^\infty \frac{\mathrm{d}M}{\mathrm{d}r} \cdot \left(1 - \sqrt{1 - \left(\frac{R}{r}\right)^2}\right) \mathrm{d}r \,. \tag{3.28}$$

In practice, we discretize the second integral and use the output of `PhaseFlow`. It is clear that the pHLR will always be smaller than the spherical half-light radius. In all of the cases we considered, they are of the same order of magnitude, however. In what follows, we work with the pHLR, which we denote with r_{eff}.

We start from a recoiling SMBH with $M_\bullet = 10^5 M_\odot$ and $V_k = 325$ km s^{-1}. According to (3.1), this implies $r_k = 4.1 \cdot 10^{-3}$ pc. Furthermore, equations (3.3) and (3.16) give $\sigma \approx 51.5$ km s^{-1} and $\sigma_{\mathrm{obs}} \approx 100$ km/s. The bound mass is determined by (3.10), and gives us about 1000 stars of $1M_\odot$. The Coulomb logarithm (3.22) is $\ln\Lambda \approx 11.4$. With respect to the smBH component, we take as a starting point a population of 20 BHs of mass $10M_\odot$ each, distributed along a Dehnen profile with $\gamma = 1.75$ and $r_D = 10^{-3}$ pc.

Note that this is the model used to create the blue track in Figure 3.4. After 10.5 Gyr we have $r_{\mathrm{eff}} \approx 5$ pc. For comparison, the deprojected half-light radius is ≈ 6.3 pc. The orange track uses the same parameters for the SMBH and the stellar population, but does not include smBHs. Recall that the driving force behind the additional expansion were smBH binaries, as stated in Sec. 3.2.2. However, the one-dimensional FP equation cannot account for binaries, meaning that it is interesting to see that we still find this expansion. Clearly, there is a phase of rapid expansion in the first ~ 1 Gyr. We find that $r_{\mathrm{eff}} \propto t^{2/3}$, which agrees with the results of the N-body simulations in [O'Leary and Loeb, 2012], as discussed in Sec. 3.3.1. Figure B.4 in the Appendix shows this explicitly.

We start by looking at the density and enclosed mass profile, shown in Figure 3.7. The blue line represents the initial conditions, and indeed displays the Dehnen profile (3.5). After the first Gyr, the density profile seems to have flattened within radii $\sim r_{\text{eff}}$, beyond which the density decreases steeply. Comparing this to Figure 3.2, we also find that the density at small radii decreases with time. However, for radii $\gtrsim 0.1$ pc, we find a density that is increased with respect to the starting time. The bottom panel in Figure 3.7 is our version of Figure 3.5. Note that our models experience much less star loss thant the results of [O'Leary and Loeb, 2012] predict (e.g. Figure 3.6). This is due to the absence of the sink term (3.24), as discussed in Sec. 3.3.2. We come back to this at the end of this section as well. All together, this shows that the HCSC has undergone significant expansion, which was already clear from Figure 3.4.

We can compare this to the profiles of the smBH population (shown in Figure B.5 in the Appendix). Figure 3.8 shows the density profile at the beginning and at the end of the simulation, for both components. At $t = 0$ Gyr, we see that the density profiles have the same slopes, though different scale radii: these are of course the initial conditions that we set. Interestingly, after 10.5 Gyr, the density profiles don't have the same slope anymore. The density of smBHs is seen to decrease more rapidly. This suggests that the populations indeed segregate, with the heavier BH population sinking to the center. However, in terms of the enclosed mass, the difference is not so extreme, as can be seen in Figure B.6.

Now that we have investigated some results of this base model, we discuss what happens when changing the parameters. First of all, we start by noting that changing the exponent of the smBH Dehnen distribution does not significantly influence the outcome. Figure 3.9 shows that the number of stars after 10.5 Gyr is approximately independent of the exact value of γ. The variation in r_{eff} is negligible. Therefore, in what follows we will just assume that $\gamma = 1.75$ for the smBH component; the same as for the stellar component.

Secondly, we note that the scale radius of this population does influence the pHLR to some extent. This can be seen in Figure 3.10. We already mentioned before that we expect the scale radius to be similar to or smaller than that of the stellar population, but we investigate the influence of larger scale radii as well. We see that there seems to be an optimal value for the scale radius, that best enhances the growth of the HCSC. This appears to be when the scale radius of both populations is similar. A possible explanation could be that a configuration where both populations have a similar scale radius implies that the heavier component can transfer a lot of orbital energy to the lighter component in an efficient way. This could then boost the expansion in a maximal way. In what follows, we therefore set both scale radii equal.

We mentioned in Sec. 3.3.2 that the Coulomb logarithm influences the end result as well. This is expected, as (3.18) works with the dimensionless time $\tau = t/t_R$, where t_R is the relaxation time (3.17), which is inversely proportional to $\ln \Lambda$. Therefore, increasing $\ln \Lambda$ forces the system to evolve faster. The effect of changing the Coulomb logarithm is shown in Figure 3.11, for two arbitrarily chosen values of $\ln \Lambda$ in addition to the reference value (3.22).

We now turn to the influence of the number and mass of the smBHs. By exploring this

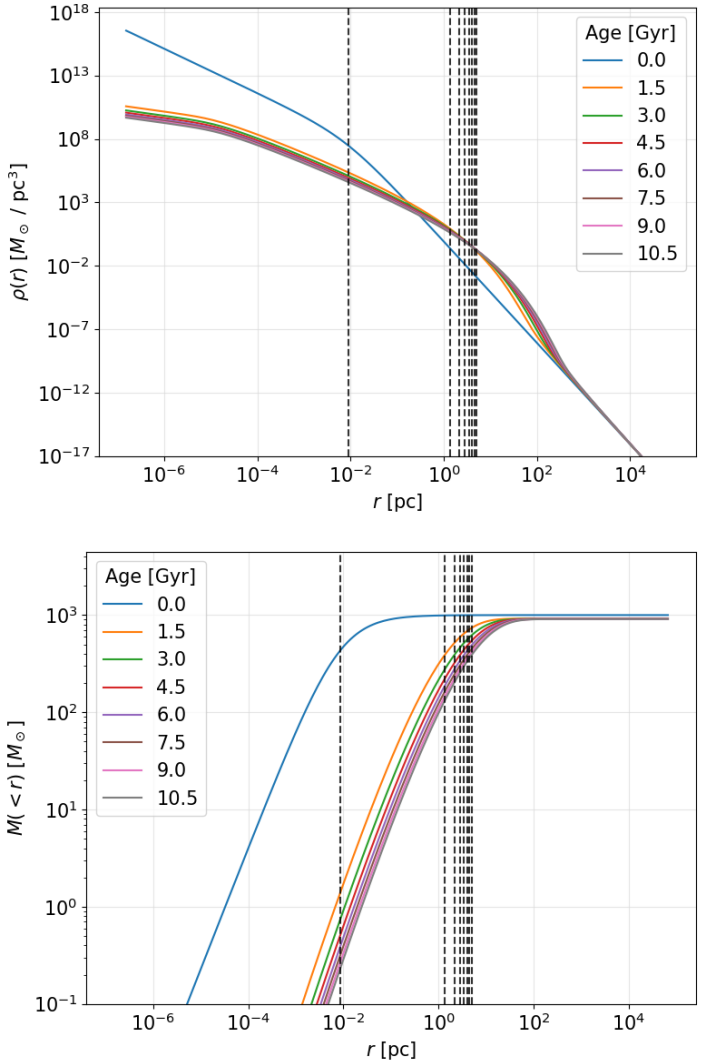

Figure 3.7: Density and enclosed mass profile of the stellar population at different times, for $M_\bullet = 10^5 M_\odot$, $V_k = 325$ km s^{-1} and a population of 20 smBHs of $10 M_\odot$ each. The dashed vertical lines correspond to $r_{\rm eff}$ at the different timesteps, with increasing values for increasing time (see Figure 3.4).

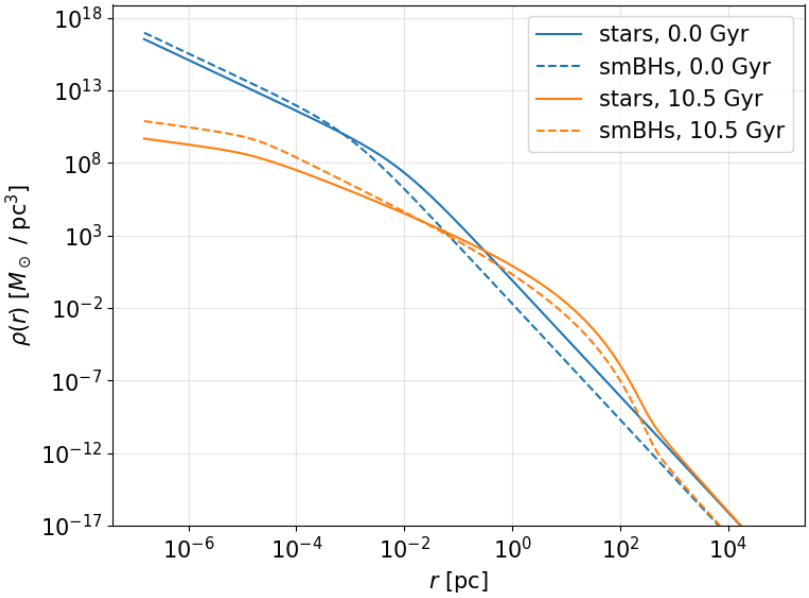

Figure 3.8: Comparison of the density profile of the stellar and smBH populations, at the start and at the end of the simulation. Initially, they both display the Dehnen profile, as set by the initial conditions. After 10.5 Gyr, the smBHs are concentrated more towards the center, relative to the stellar population. This is caused by gravitational settling.

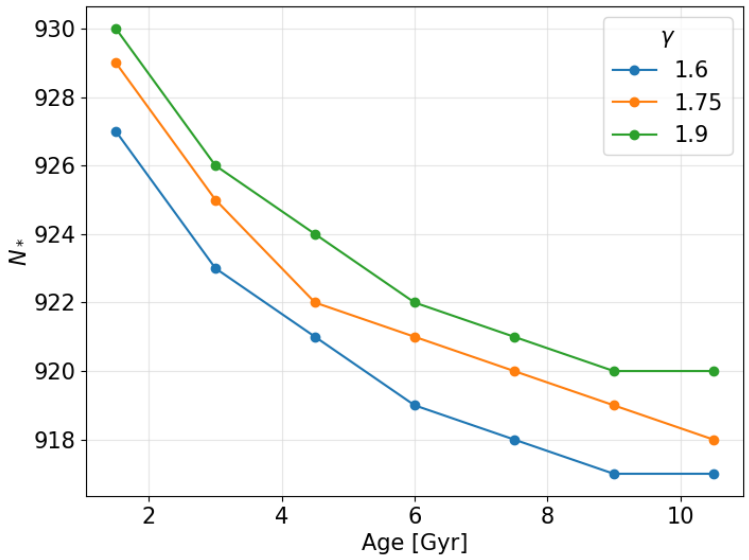

Figure 3.9: Number of stars remaining in a HCSC with $M_\bullet = 10^5 M_\odot, V_k = 325$ km s^{-1}, an inital stellar population of 1000 solar-mass stars and an initial smBH population of $20 \times 10 M_\odot$. The first timestep, at $t = 0$ Gyr, is not shown: $N = 1000$ for all three models and the difference between them is more clear on this scale. The number is determined by rounding of the total mass in the cluster, to obtain an integer. The exponent γ of the Dehnen profile of the smBH population is seen to have very little influence.

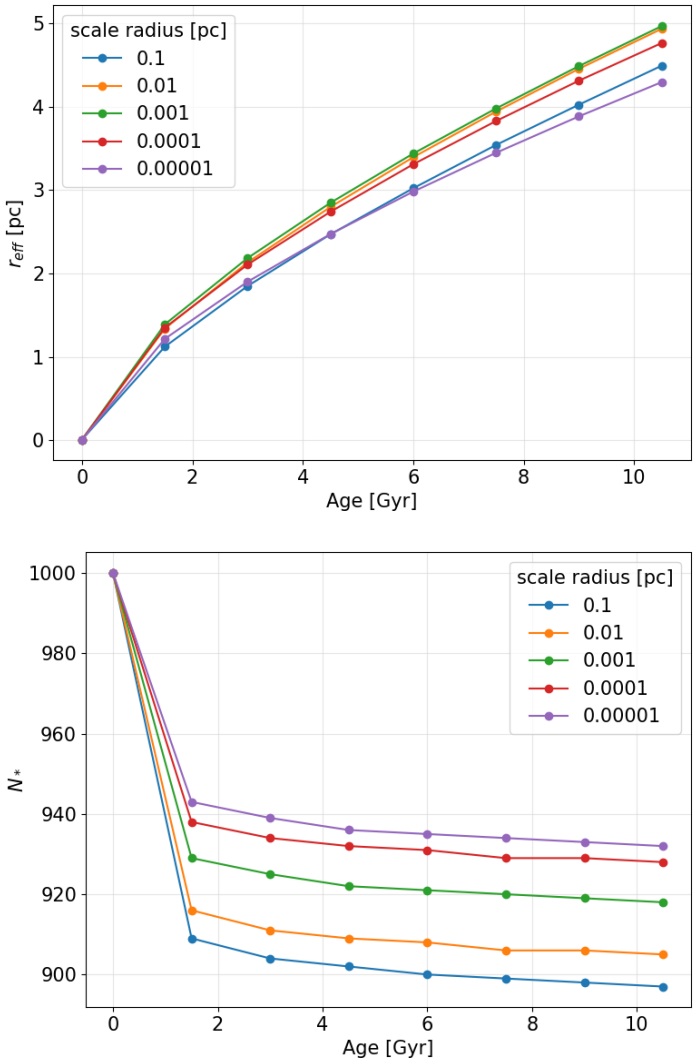

Figure 3.10: Influence of the scale radius in the Dehnen profile of the smBH component on r_{eff} and the number of stars. The scale radius of the stellar population is $\sim 8.2 \cdot 10^{-3}$ pc, and we do not expect the scale radius of the smBH distribution to be much larger.

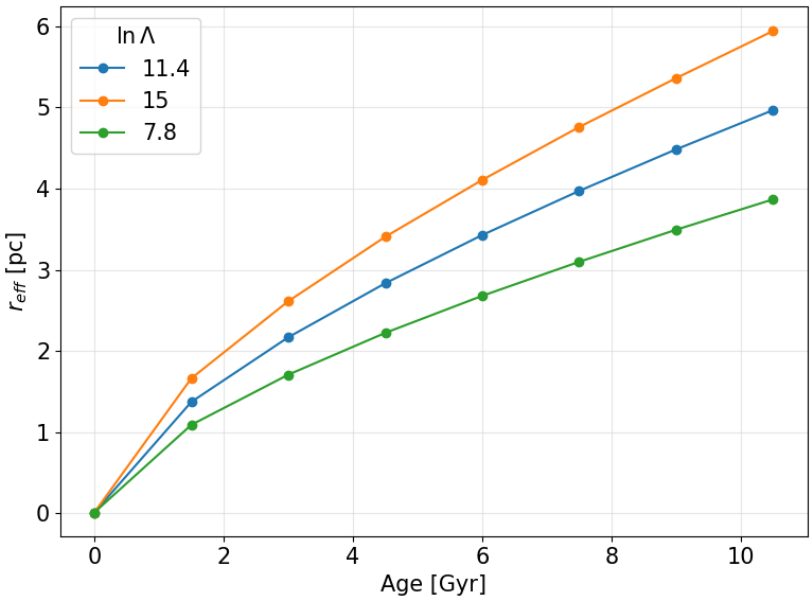

Figure 3.11: Influence of changing the Coulomb logarithm on the effective radius of a HCSC, for our base model. The reference value given by (3.22) is $\ln \Lambda \approx 11.4$.

parameter space (see Figure 3.12), we find an approximate scaling relation:

$$\log r_{\rm eff} \approx \beta_0 + \beta_N \log N_{\rm smBH} + \beta_M \log M_{\rm smBH} \,. \tag{3.29}$$

Exploring the parameter space, we restrict ourselves to $M_{\rm smBH} \gtrsim 5 M_\odot$, as observations of BHs with lower mass remain absent [Casares and Jonker, 2014, Collaboration et al., 2022]. Furthermore, we also take $N_{\rm smBH} \geq 2$, to at least have multiple smBHs. We perform an ordinary least squares (OLS) fit[11] of this hyperplane in the 3-dimensional log-parameter space and find that after evolving the system[12] for 10.5 Gyr

$$\begin{aligned} \boldsymbol{\beta} &\equiv (\beta_0, \beta_N, \beta_M) \\ &= (-0.66 \pm 0.02, 0.321 \pm 0.008, 0.952 \pm 0.013) \,. \end{aligned} \tag{3.30}$$

The (adjusted) R^2 of the fit is 0.993 (0.992), indicating a very good fit. All the fit parameters are significantly different from zero. This means that, at least locally,

$$r_{\rm eff} \approx 5.1 \left(\frac{N_{\rm smBH}}{20}\right)^{0.321} \left(\frac{M_{\rm smBH}}{10}\right)^{0.95} \text{pc} \,. \tag{3.31}$$

Figure (3.13) shows an illustration of the fit.

[11] We have also performed an orthogonal distance regression (ODR) to fit the hyperplane, which gave results that are fully consistent. ODR minimizes the orthogonal distance between the points and the hyperplane, whereas an OLS fit minimizes the distance along one axis. For illustration, the ODR counterpart of (3.30) is $\boldsymbol{\beta} = (-0.66 \pm 0.02, 0.322 \pm 0.008, 0.955 \pm 0.013)$.

[12] The values of the constants depend on time, since the pHLR does as well. However, since we found that $r_{\rm eff} \propto t^{2/3}$, we expect only the constant β_0 to depend on time. This is indeed the case, but the other constants still depend on the rest of the model: indeed, we find different values for these constants in Sec. 3.5. We focus on the scaling relation at the end of our simulation.

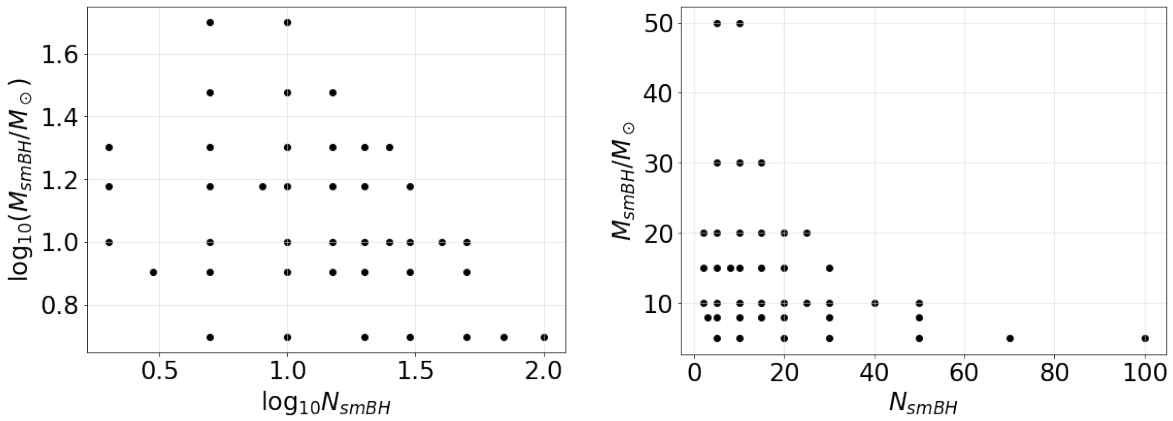

Figure 3.12: Parameter space for the hyperplane (3.29) fit with results (3.30) on a *(left)* logartihmic and *(right)* linear scale. The parameter space contains points such that the total mass of the smBH population is between $\sim 20M_\odot$ and $\sim 500M_\odot$.

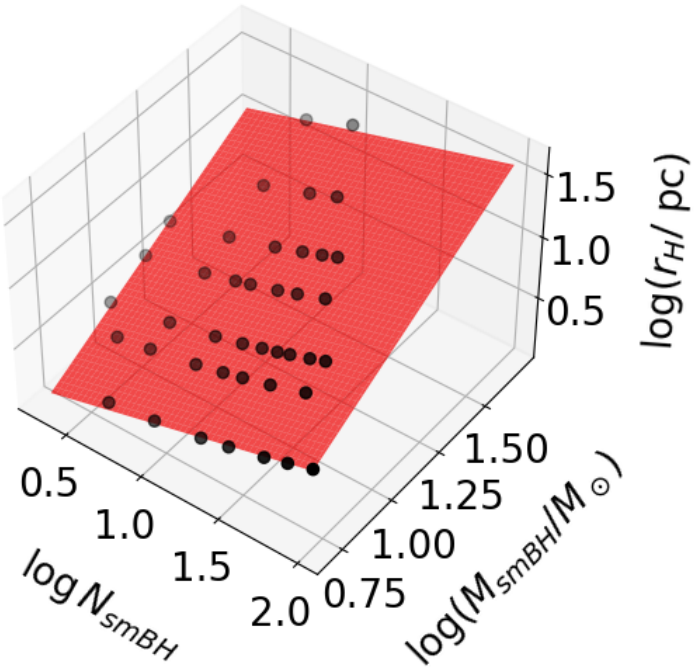

Figure 3.13: Illustration of the hyperplane (3.29) with parameters (3.30) in the logarithmic parameter space. The black dots are the points in the parameter space used to determine the fit (see Figure 3.12).

Finally, we have a look at the velocity dispersion. For our base model, the velocity dispersion at the start of the simulation is $\mathcal{O}(100)$ km s^{-1}, as expected from (3.16). However, at the end of the simulation, the three-dimensional velocity dispersion[13] at the pHLR is ~ 5 km s^{-1}, which is the order of magnitude that is expected from (2.1). This shows however that, after the significant expansion that results from ~ 10 Gyr of evolution, the velocity dispersion decreases significantly. This velocity dispersion could be increased if we find a model with a more massive SMBH, such that the Keplerian velocity is increased at ~ 5 pc. We leave this for future work.

Revisiting the extra sink terms

As mentioned in 3.3.2, [O'Leary and Loeb, 2012] found that the resonant relaxation (3.24) significantly influenced the outcome of their simulations. This term is not included in `PhaseFlow`, however. To assess its importance, we take an alternative approach[14]. Resonant relaxation drives the TDE rate up, and to mimick this effect we increase the tidal radius (3.11). The tidal radius for a $10^5 M_\odot$ SMBH and a Sun-like star is $\sim 10^{-6}$ pc. The pHLR of the stellar population is only mildly influenced if we increase the tidal radius: see Figure 3.14. On the other hand, the number of stars is significantly lowered, which is to be expected if we increase the tidal radius. However, if we now also multiply the smBH capture radius (3.26) by the same factors[15], we find that the pHLR is lowered by a larger factor. It also further decreases the number of surviving stars, but not as much as the increase of the tidal radius. While increasing these capture radii, we effectively increase the loss-cone in order to mimick the enhanced TDE rate that the resonant relaxation sink would bring. We leave it to future work to figure out what factor would mimick this sink well, in order to assess the importance of the latter. Note that, even when multiplying the capture radii with a factor 100, the mass loss is not as severe as [O'Leary and Loeb, 2012] found (see Figure 3.6.)

3.5 Modelling observational candidates

The previous section presented some general results based on an arbitrarily chosen model. In this section, we have a look at some faint stellar clusters that according to the argument in Sec. 3.2.2 could potentially be these elusive HCSCs. We look for a models that agree with observations, and explore what part of the parameter space the smBH population could cover using the scaling relation (3.29), with parameters that correspond to the new models. As we are considering satellites of the Milky Way, we will restrict to recoil kicks below its escape velocity, which is on the order of 600 km s^{-1} [Kafle et al., 2014]. Furthermore, Sgr A*, the SMBH at the center of the Galaxy, has a mass on the order of $10^6 M_\odot$. We don't expect the SMBHs in HCSCs to be more massive than this - as hierarchical formation suggests that the final remnant SMBH at the center of the Galaxy is one of the

[13] `PhaseFlow` also returns the two-dimensional projected velocity dispersion. This is of the same order of magnitude as the three-dimensional velocity dispersion, and we focus on the latter for now.

[14] We thank dr. Eugene Vasiliev for this suggestion.

[15] Note that smBHs don't get tidally disrupted by the SMBH, but rather captured as a whole. To mimick the effect of an increased loss cone, it makes sense to multiply the capture radii of both components with the same factor.

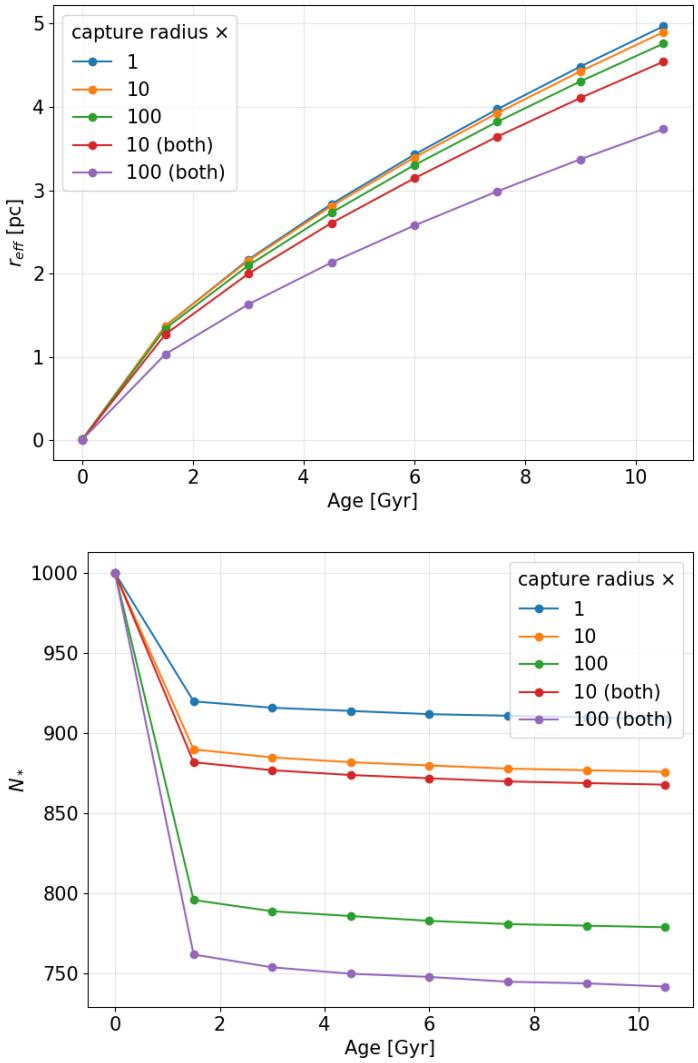

Figure 3.14: Influence of changing the capture radii on *(top)* $r_{\rm eff}$ and *(bottom)* the number of stars $N_\star$. The blue line corresponds to our base model, and the orange and green lines to the same model with the tidal radius (3.11) multiplied with a factor 10 and 100, respectively. The red and purple lines also multiply the smBH capture radius (3.26) with the same factor. Increasing the capture radii is a way to increase the loss cone, in order to mimick the effect of an additional sink term, like the one due to resonant relaxation (3.24).

heaviest formed - and will therefore restrict to masses below this.

It should be noted that the results we obtain in this section should be considered as order-of-magnitude predictions, as many assumptions go into the relations that we use. However, this section should give a good idea of the kind of HCSCs that we could expect, if these faint halo clusters turn out to be the consequence of recoiling SMBHs.

3.5.1 DELVE 1

The first HCSC target that we consider is DELVE 1 [Mau et al., 2020]. It has an effective radius $r_{\rm eff} = 5.4^{+1.5}_{-1.1}$ pc and an estimated total stellar mass $M_\star = 144^{+24}_{-27} M_\odot$. This mass estimate is based on fitting an isochrone to the observed color-magnitude diagram of the cluster, which in combination with an initial-mass function (IMF) gives an estimate of the total stellar mass, including the portion that we don't see. This method is of course subject to uncertainties, as the errors on the estimate indicate. The cluster is estimated to have an age equal to $\tau = 12.5^{+1.0}_{-0.7}$ Gyr.

We model this system with the aim to get the correct pHLR and stellar mass - recall that our models assume all stars have mass $1M_\odot$ - after 12.5 Gyr. We consider different possible values for the recoil velocity, and use[16] (3.10) to estimate $M_\bullet$. This relation contains the initial bound mass M_b, which we take above the target stellar mass. In the end, we then check that the remaining number of stars is as desired.

Kick $V_k = 400$ km s^{-1}

Starting from a kick velocity of 400 km s^{-1}, a SMBH of mass $4 \cdot 10^4 M_\odot$ leads to $M_b \approx 159 M_\odot$. We explore a parameter space for $N_{\rm smBH} \gtrsim 2$ and $M_{\rm smBH} \gtrsim 5M_\odot$ such that the total mass in smBHs is smaller than M_*. We fit the hyperplane (3.29) to find

$$\boldsymbol{\beta} = (-0.735 \pm 0.016, 0.439 \pm 0.009, 1.095 \pm 0.011)\,. \tag{3.32}$$

The fit has $R^2 = 0.997$, indicating once again a very good fit. For every model that we explored in this parameter space, the remaining number of stars is between 136 and 140. This is perfectly acceptable, given the target M_*.

We use this hyperplane to determine the parameter space for the smBH population that give rises to a pHLR within the observational bounds. This region can be seen in Figure 3.15, and should give a rough idea of what we can expect for the smBH population *if* DELVE 1 is a HCSC with kick velocity on the order of 400 km s^{-1}.

To estimate the velocity dispersion at the pHLR, we take a model with 10 smBHs of $9M_\odot$, which according to (3.32) has the desired pHLR. The predicted three-dimensional velocity dispersion at the pHLR is ~ 2.9 km s^{-1}. We have checked that this value is the same if we take a model in a different part of the parameter space.[17]

[16] Recall that we made a comment in footnote 2, saying we obtained a different factor for (3.9) and (3.10). It turns out that using these new factors, we don't find models in the desired parameter space of kicks and SMBH masses.

[17] We have checked $25 \times 6M_\odot$ and $5 \times 12M_\odot$ smBHs.

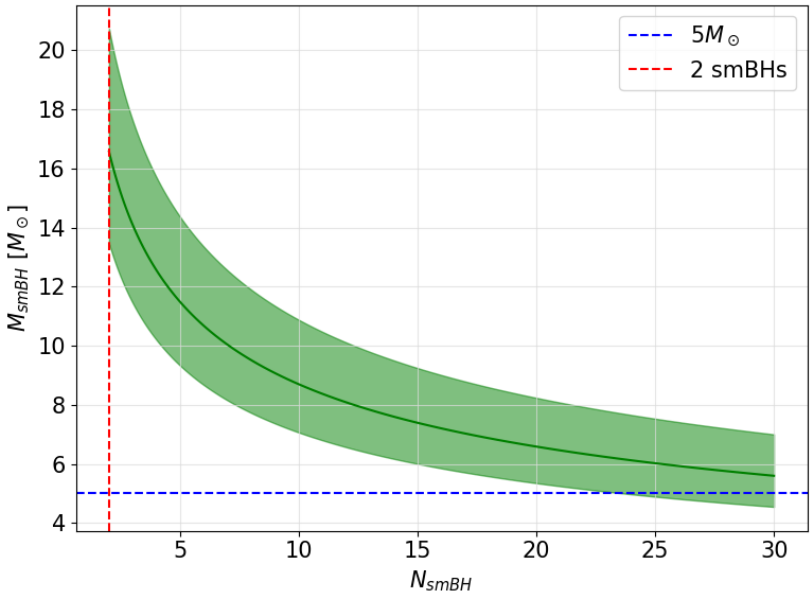

Figure 3.15: Part of the parameter space for the smBH population around a $4 \cdot 10^4 M_\odot$ SMBH with $V_k = 400$ km s^{-1} that has a pHLR within the observational bounds of DELVE 1, i.e. $r_{\text{eff}} = 5.4^{+1.5}_{-1.1}$ pc. All models have been evolved for 12.5 Gyr, and have a final number of stars that falls within the observational bounds as well. The dashed lines indicate "limits of plausibility", i.e. we want multiple smBHs, with masses above $\sim 5M_\odot$.

Kick $V_k = 500$ km/s

We repeat this analysis for a kick velocity of 500 km s^{-1}. A SMBH of mass $5.8 \cdot 10^4 M_\odot$ leads to $M_b \approx 155 M_\odot$. The fit of the hyperplane (3.29) now corresponds to

$$\boldsymbol{\beta} = (-0.893 \pm 0.017, 0.439 \pm 0.008, 1.094 \pm 0.012)\,, \tag{3.33}$$

and the fit has $R^2 = 0.998$. Note how the constants β_N, β_M in (3.32) and (3.33) agree, whereas the values for β_0 differ.

In all cases considered, the remaining number of stars is between 132 and 136, which is acceptable, though a bit on the low end. However, this can be attributed to the fact that we started with 4 stars less as well, compared to the $V_k = 400$ km s^{-1} case. The region of the parameter space corresponding to the target pHLR can be seen in Figure 3.16.

The estimated three-dimensional velocity dispersion is $\sigma \approx 3.5$ km s^{-1}, based on a model with $15 \times 10 M_\odot$ smBHs.

Lower kick velocities

For lower kick velocities to retain a similar amount of stars, the SMBH mass needs to be smaller as well. Therefore, we could make more plots similar to Figures 3.15 and 3.16, where the parameter space would get more restricted to the lower left corner (smaller total smBH masses) as the kick velocity decreases. At some point, smBHs would be redundant in order to obtain the target pHLR. As an example, a SMBH with $M_\bullet \approx 900 M_\odot$ and

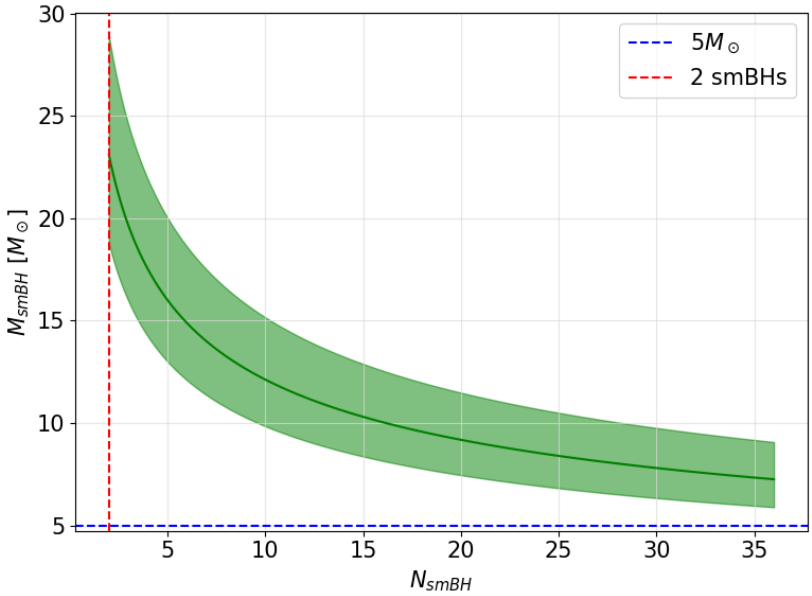

Figure 3.16: Similar to Figure 3.15, but with $M_\bullet = 5.8 \cdot 10^4 M_\odot$ and $V_k = 500$ km s^{-1}. The region is seen to extend towards larger $N_{\rm smBH}$. The green line crosses the horizontal dashed line at $N_{\rm smBH} \sim 100$. However, we choose to not extend it further, as it falls outside the parameter region that we explored, and is therefore an extrapolation of our fit. Furthermore, this extended region would correspond to the population of smBHs having more mass in total than the stellar population. This is not impossible, but falls beyond the scope of this research.

a kick velocity on the order of 160 km s^{-1} result in a HCSC that, after 12.5 Gyr, has $r_{\text{eff}} \sim 5$ pc and about 150 $M_\odot$ in stars remaining, without any smBH component. This model predicts a three-dimensional velocity dispersion $\sigma \approx 1.4$ km s^{-1}.

Conclusion

We see that we can explain the observational properties of DELVE 1 with a variety of models that differ in SMBH mass, recoil kick velocity and smBH population. The different models predict different values for the velocity dispersion. Therefore, a measurement of the latter could possibly rule out a subset of these models. Furthermore, a GC with these observed properties is expected to have a velocity dispersion $\lesssim 0.2$ km s^{-1}, meaning that if the velocity dispersion can be observed to an accuracy of ~ 1 km s^{-1} we could rule out one of the possible natures of this cluster. A proposal has been submitted by prof. Jonker to measure this velocity dispersion, though this assumed that a less accurate measurement was needed, since $\sigma \approx 13$ km s^{-1} was assumed.

3.5.2 AM4

We repeat the analysis for the cluster AM4 [Hamren et al., 2013, Muñoz et al., 2018]. It is larger than DELVE 1, with $r_{\text{eff}} = 7.3 \pm 1.4$ pc. The age of this cluster is estimated to be > 13 Gyr. However, no extrapolated mass estimate is given for this cluster. The authors do assemble a color-magnitude diagram with 435 stars, however. As the age of the cluster is longer than the main-sequence lifetime of the Sun, all the stars that remain should have masses $\lesssim 1 M_\odot$. We will therefore use a stellar mass of $435 M_\odot$ as target stellar mass, which likely underestimates the true mass though.

We only illustrate the parameter space for a recoil kick $V_k = 500$ km s^{-1}. We have $M_\bullet = 1.3 \cdot 10^5 M_\odot$ and $M_b = 498 M_\odot$. The fit of the hyperplane (3.29) gives parameters

$$\boldsymbol{\beta} = (-1.232 \pm 0.016, 0.487 \pm 0.005, 1.153 \pm 0.008)\,, \tag{3.34}$$

and the (adjusted) R^2 is 0.999. The remaining number of stars for all models is between 440 and 450, which is a bit higher than our target. This is not a problem, as we likely underestimated the stellar mass. The region of the parameter space corresponding to the target pHLR can be seen in Figure 3.17.

The estimated three-dimensional velocity dispersion is $\sigma \approx 4.5$ km s^{-1}, which is higher than what we found for DELVE 1, due to the more massive SMBH.

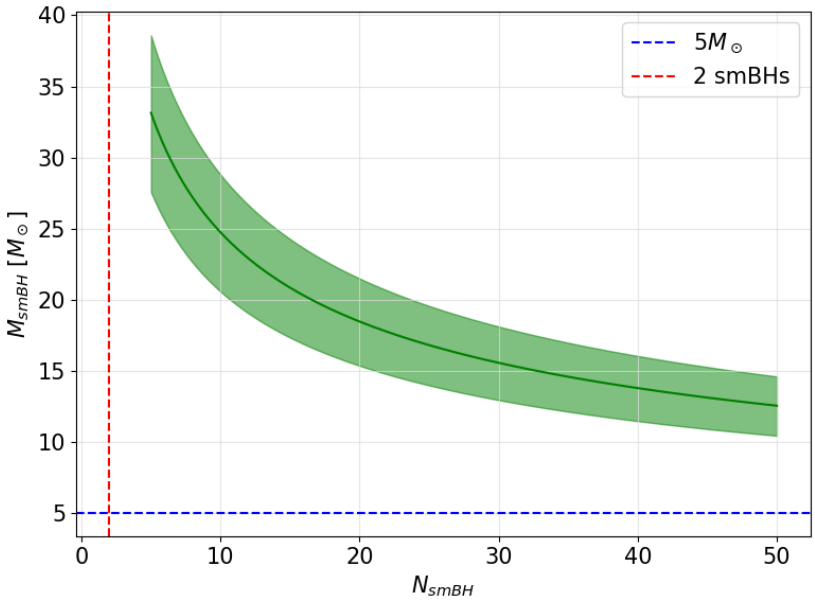

Figure 3.17: Part of the parameter space for the smBH population around a $1.3 \cdot 10^5 M_\odot$ SMBH with $V_k = 500$ km s^{-1} that has a pHLR within the observational bounds of AM4, i.e. $r_{\rm eff} = 7.3 \pm 1.4$ pc. All models have been evolved for 13 Gyr, and have a final number of stars that falls within the observational bounds as well. The dashed lines indicate "limits of plausibility", i.e. we want multiple smBHs, with masses above $\sim 5M_\odot$. The allowed parameter space could be extended even further to larger numbers of black holes, but we did not explore this parameter space for the fittin procedure, as the total smBH mass would get much larger than the stellar mass. This is not impossible, but beyond the scope of this work.

Chapter 4

Conclusion and Outlook

The future space-based gravitational-wave detector LISA will provide scientists with a cornucopia of data that will enable breakthroughs in different fields. The goals of the LISA mission are summarized in 8 different science objectives, and in this thesis we have explored two topics that relate to these objectives. The first topic covered the gravitational-wave background due to extragalactic white dwarf binaries, which falls under the aim of detecting an astrophysical background. One of the other science objectives aims to reproduce the formation history of supermassive black holes, and we have looked into the putative hypercompact stellar clusters that should form as a consequence of their mergers. Below, we summarize our main findings, and provide possible future lines of work.

The gravitational-wave background from extragalactic white-dwarf binaries

We have revisited earlier work by [Farmer and Phinney, 2003], who modelled the gravitational-wave background sourced by extragalactic white-dwarf binaries. We have compared their results to the extrapolated current best estimates for the background from coalescing black hole and neutron star binaries, obtained by the LVK collaboration in the high-frequency regime [LIGO Scientific Collaboration, Virgo Collaboration, and KAGRA Collaboration et al., 2021]. The conclusion is that the WD component is likely dominant over the other ones. We have discussed a few other works that put forward a similar hypothesis, and supported it further with a rough order-of-magnitude argument. This poses a problem, as the different components are hard to disentangle. For all of them, the dimensionless energy density Ω follows the same frequency dependence, $\Omega \propto f^{2/3}$, throughout most of the LISA band.

We have taken two approaches to model the background, one of which we normalized to the results of [Farmer and Phinney, 2003]. Our second approach provided our own independent prediction for the amplitude of the GWB, which is about a factor 5 larger at 1 mHz than the latter.

The main features of our GWB are in agreement with what [Farmer and Phinney, 2003] found. Below ~ 0.1 mHz, Ω is steeply increasing according to a power law with exponent $\approx 10/3$. Following this steep decrease, there is a transition region before the background starts to follow the expected $\Omega \propto f^{2/3}$ power law. This is the case until the peak, at

around ~ 10 mHz, after which Ω decreases again due to the merging of the binaries. The background that we simulated exhibited a slower decay after the peak, compared to the results of [Farmer and Phinney, 2003].

We have considered explorative alternative models for the cosmic star formation history, to investigate its influence on the total background. We found that the variation in the LISA band was very mild (see Table 2.2 and Figure 2.19), in agreement with the findings of [Farmer and Phinney, 2003]. However, given the larger amplitude of our background, we found that disentangling the WD component in the LISA band could be feasible, as the peak is now better visible in the LISA band. This peak must be due to the WD component, as the other components are expected to follow $\Omega \propto f^{2/3}$ until the LVK frequency band.

Some parts of our work here can still be improved on. For now, we have just based the error on our prediction on the relative error found in [Farmer and Phinney, 2003]. However, a more accurate estimate of the error could be made by considering realistic alternative WD populations, as done in the original source. Furthermore, an error due to the uncertainty on the SFH could be estimated by considering variations of the SFH within observational bounds, although we don't expect that this will impact the GWB a lot. Finally, it could be interesting to investigate whether data analysis pipelines for the GWB could actually extract the peak due to WD mergers around 10 mHz from data, i.e. whether the peak is actually detectable. This would provide good insight on how realistic it is to disentangle the WD component from the others.

Hypercompact stellar clusters

We went over existing literature to construct initial conditions for HCSCs, which we then evolved using the Fokker-Planck solver `PhaseFlow`. We have investigated the influence of a smBH population on the cluster's properties after a Hubble time. For a fixed SMBH mass and stellar population, the addition of a smBH component causes the cluster to reach larger sizes, which we characterized by the half-light radius. We looked at the importance of the different parameters of the smBH population, and found the approximate scaling relation (3.29).

The additional expansion caused by a smBH population means that some faint clusters in the Milky Way halo are actually feasible candidates for these (so far) undetected systems. We modelled two of these candidates, DELVE 1 and AM4, and used our scaling relation (3.29) to delineate a part in the parameter space of smBH mass and number that agrees with observational properties of the candidates. Depending on the kick velocity that we used as input for the model, we found different predictions for the velocity dispersion of these clusters. Measuring this velocity dispersion, for which proposals are submitted, could then distinguish between different models from the collection that we constructed. Furthermore, as these velocity dispersions are larger than the typical values for globular clusters of similar size, an accurate measurement of the velocity dispersion could provide conclusive evidence for the nature of these faint clusters.

One possible line of research that this work could benefit from, is to provide further clar-

ity on whether resonant relaxation (3.24) should be included in the model or not. As explained, it is thought that relativistic precession counteracts this effect. However, it is not fully clear yet why the inclusion of this sink term was necessary to match the results of the N-body and Fokker-Planck simulations performed in [O'Leary and Loeb, 2012]. This has a large effect on the mass loss that the cluster experiences, which alters the models significantly.

Additionally, it would be interesting to perform full N-body simulations of recoiling SMBHs, with both a stellar population and smBH population bound to them. This could also provide further insights on the amount of mass loss that the stellar population actually experiences. Finally, we note that it could be fruitful to estimate realistic values of the recoil velocity for the faint halo clusters, based on their position in the halo. This would further constrain the models, since we now considered a wide range of possible kick velocities.

Bibliography

R. Abbott, T. Abbott, F. Acernese, K. Ackley, C. Adams, N. Adhikari, R. Adhikari, V. Adya, C. Affeldt, D. Agarwal, et al. Gwtc-3: compact binary coalescences observed by ligo and virgo during the second part of the third observing run. *arXiv preprint arXiv:2111.03606*, 2021.

M. R. Adams and N. J. Cornish. Detecting a stochastic gravitational wave background in the presence of a galactic foreground and instrument noise. *Physical Review D*, 89 (2):022001, 2014.

W. S. Adams. AN A-TYPE STAR OF VERY LOW LUMINOSITY. *Publications of the Astronomical Society of the Pacific*, 26(155):198–198, Oct. 1914. ISSN 0004-6280, 1538-3873. doi: 10.1086/122337. URL https://iopscience.iop.org/article/10.1086/122337.

C. Aerts. Stellar structure & evolution, September 2021. Course notes in the Master of Astronomy and Astrophyiscs at Katholieke Universiteit Leuven.

T. Akiba and A.-M. Madigan. Anisotropic Star Clusters around Recoiling Supermassive Black Holes, May 2023. URL http://arxiv.org/abs/2305.03054. arXiv:2305.03054 [astro-ph].

T. Alexander. EMRIs and the relativistic loss-cone: The curious case of the fortunate coincidence. *Journal of Physics: Conference Series*, 840:012019, May 2017. ISSN 1742-6588, 1742-6596. doi: 10.1088/1742-6596/840/1/012019. URL http://arxiv.org/abs/1702.00597. arXiv:1702.00597 [astro-ph].

B. Allen and J. D. Romano. The Hellings and Downs correlation of an arbitrary set of pulsars. 2022. doi: 10.48550/ARXIV.2208.07230. URL https://arxiv.org/abs/2208.07230. Publisher: arXiv Version Number: 5.

P. Amaro-Seoane et al. Laser Interferometer Space Antenna, Feb. 2017. URL http://arxiv.org/abs/1702.00786. arXiv:1702.00786 [astro-ph].

P. Atri, J. C. A. Miller-Jones, A. Bahramian, R. M. Plotkin, P. G. Jonker, G. Nelemans, T. J. Maccarone, G. R. Sivakoff, A. T. Deller, S. Chaty, M. A. P. Torres, S. Horiuchi, J. McCallum, T. Natusch, C. J. Phillips, J. Stevens, and S. Weston. Potential kick velocity distribution of black hole X-ray binaries and implications for natal kicks. *Monthly Notices of the Royal Astronomical Society*, 489:3116–3134, Nov. 2019. ISSN 0035-8711. doi: 10.1093/mnras/stz2335. URL https://ui.adsabs.harvard.edu/abs/2019MNRAS.489.3116A. ADS Bibcode: 2019MNRAS.489.3116A.

F. Bacchini, D. R. Mayerson, B. Ripperda, J. Davelaar, H. Olivares, T. Hertog, and B. Vercnocke. Fuzzball Shadows: Emergent Horizons from Microstructure. *Physical Review Letters*, 127(17):171601, Oct. 2021. ISSN 0031-9007, 1079-7114. doi: 10.1103/PhysRevLett.127.171601. URL https://link.aps.org/doi/10.1103/PhysRevLett.127.171601.

J. N. Bahcall and R. A. Wolf. Star distribution around a massive black hole in a globular cluster. *The Astrophysical Journal*, 209:214–232, Oct. 1976. ISSN 0004-637X. doi: 10.1086/154711. URL https://ui.adsabs.harvard.edu/abs/1976ApJ...209..214B. ADS Bibcode: 1976ApJ...209..214B.

J. N. Bahcall and R. A. Wolf. The star distribution around a massive black hole in a globular cluster. II. Unequal star masses. *The Astrophysical Journal*, 216:883–907, Sept. 1977. ISSN 0004-637X. doi: 10.1086/155534. URL https://ui.adsabs.harvard.edu/abs/1977ApJ...216..883B. ADS Bibcode: 1977ApJ...216..883B.

H. Baumgardt, J. Makino, and T. Ebisuzaki. Massive Black Holes in Star Clusters. II. Realistic Cluster Models. *The Astrophysical Journal*, 613(2):1143–1156, Oct. 2004. ISSN 0004-637X, 1538-4357. doi: 10.1086/423299. URL https://iopscience.iop.org/article/10.1086/423299.

J. D. Bekenstein. Gravitational-Radiation Recoil and Runaway Black Holes. *The Astrophysical Journal*, 183:657–664, July 1973. ISSN 0004-637X. doi: 10.1086/152255. URL https://ui.adsabs.harvard.edu/abs/1973ApJ...183..657B. ADS Bibcode: 1973ApJ...183..657B.

E. Berti and M. Volonteri. Cosmological Black Hole Spin Evolution by Mergers and Accretion. *The Astrophysical Journal*, 684(2):822–828, Sept. 2008. ISSN 0004-637X, 1538-4357. doi: 10.1086/590379. URL https://iopscience.iop.org/article/10.1086/590379.

G. Boileau, A. C. Jenkins, M. Sakellariadou, R. Meyer, and N. Christensen. Ability of lisa to detect a gravitational-wave background of cosmological origin: The cosmic string case. *Physical Review D*, 105(2):023510, 2022.

C. T. Bolton. Identification of Cygnus X-1 with HDE 226868. *Nature*, 235(5336):271–273, Feb. 1972. ISSN 0028-0836, 1476-4687. doi: 10.1038/235271b0. URL https://www.nature.com/articles/235271b0.

H. Bondi, M. G. J. van der Burg, and A. W. K. Metzner. Gravitational Waves in General Relativity. VII. Waves from Axi-Symmetric Isolated Systems. *Proceedings of the Royal Society of London Series A*, 269:21–52, Aug. 1962. ISSN 0080-46301364-5021. doi: 10.1098/rspa.1962.0161. URL https://ui.adsabs.harvard.edu/abs/1962RSPSA.269..21B. ADS Bibcode: 1962RSPSA.269...21B.

G. Burgio, H.-J. Schulze, I. Vidaña, and J.-B. Wei. Neutron stars and the nuclear equation of state. *Progress in Particle and Nuclear Physics*, 120:103879, Sept. 2021. ISSN 01466410. doi: 10.1016/j.ppnp.2021.103879. URL https://linkinghub.elsevier.com/retrieve/pii/S0146641021000338.

M. Campanelli, C. O. Lousto, Y. Zlochower, and D. Merritt. Maximum Gravitational Recoil. *Physical Review Letters*, 98(23):231102, June 2007. ISSN 0031-9007, 1079-7114. doi: 10.1103/PhysRevLett.98.231102. URL https://link.aps.org/doi/10.1103/PhysRevLett.98.231102.

V. Cardoso and P. Pani. Testing the nature of dark compact objects: a status report. *Living Reviews in Relativity*, 22(1):4, Dec. 2019. ISSN 2367-3613, 1433-8351. doi: 10.1007/s41114-019-0020-4. URL http://link.springer.com/10.1007/s41114-019-0020-4.

S. M. Carroll. *Spacetime and geometry*. Cambridge University Press, 2019.

J. Casares and P. G. Jonker. Mass Measurements of Stellar and Intermediate-Mass Black Holes. *Space Science Reviews*, 183(1-4):223–252, Sept. 2014. ISSN 0038-6308, 1572-9672. doi: 10.1007/s11214-013-0030-6. URL http://link.springer.com/10.1007/s11214-013-0030-6.

T. L. S. Collaboration, the Virgo Collaboration, et al. Population Properties of Compact Objects from the Second LIGO-Virgo Gravitational-Wave Transient Catalog. *The Astrophysical Journal Letters*, 913(1):L7, May 2021. ISSN 2041-8205, 2041-8213. doi: 10.3847/2041-8213/abe949. URL http://arxiv.org/abs/2010.14533. arXiv:2010.14533 [astro-ph, physics:gr-qc].

T. L. S. Collaboration, the Virgo Collaboration, and the KAGRA Collaboration et al. The population of merging compact binaries inferred using gravitational waves through GWTC-3, Feb. 2022. URL http://arxiv.org/abs/2111.03634. arXiv:2111.03634 [astro-ph, physics:gr-qc].

C. J. Conselice, A. Wilkinson, K. Duncan, and A. Mortlock. THE EVOLUTION OF GALAXY NUMBER DENSITY AT $z < 8$ AND ITS IMPLICATIONS. *The Astrophysical Journal*, 830(2):83, Oct. 2016. ISSN 1538-4357. doi: 10.3847/0004-637X/830/2/83. URL https://iopscience.iop.org/article/10.3847/0004-637X/830/2/83.

A. Cooray. Gravitational-wave background of neutron star–white dwarf binaries. *Monthly Notices of the Royal Astronomical Society*, 354(1):25–30, 2004.

W. J. G. De Blok. The Core-Cusp Problem. *Advances in Astronomy*, 2010:1–14, 2010. ISSN 1687-7969, 1687-7977. doi: 10.1155/2010/789293. URL http://www.hindawi.com/journals/aa/2010/789293/.

W. DeRocco and J. A. Dror. Searching For Stochastic Gravitational Waves Below a Nanohertz. 2023. doi: 10.48550/ARXIV.2304.13042. URL https://arxiv.org/abs/2304.13042. Publisher: arXiv Version Number: 1.

A. Eckart and R. Genzel. Stellar proper motions in the central 0.1 pc of the Galaxy. *Monthly Notices of the Royal Astronomical Society*, 284(3):576–598, Jan. 1997. ISSN 0035-8711, 1365-2966. doi: 10.1093/mnras/284.3.576. URL https://academic.oup.com/mnras/article-lookup/doi/10.1093/mnras/284.3.576.

P. P. Eggleton. Approximations to the radii of Roche lobes. *The Astrophysical Journal*, 268:368, May 1983. ISSN 0004-637X, 1538-4357. doi: 10.1086/160960. URL http://adsabs.harvard.edu/doi/10.1086/160960.

D. J. Eisenstein, J. Liebert, H. C. Harris, S. J. Kleinman, A. Nitta, N. Silvestri, S. A. Anderson, J. C. Barentine, H. J. Brewington, J. Brinkmann, M. Harvanek, J. Krzesiński, E. H. Neilsen, Jr., D. Long, D. P. Schneider, and S. A. Snedden. A Catalog of Spectroscopically Confirmed White Dwarfs from the Sloan Digital Sky Survey Data Release 4. *The Astrophysical Journal Supplement Series*, 167:40–58, Nov. 2006. ISSN 0067-0049. doi: 10.1086/507110. URL https://ui.adsabs.harvard.edu/abs/2006ApJS..167...40E. ADS Bibcode: 2006ApJS..167...40E.

L. et a;. GW190521: A Binary Black Hole Merger with a Total Mass of 150 M $M_{\odot}$. *Physical Review Letters*, 125(10):101102, Sept. 2020. ISSN 0031-9007, 1079-7114. doi: 10.1103/PhysRevLett.125.101102. URL https://link.aps.org/doi/10.1103/PhysRevLett.125.101102.

E. et al. First M87 Event Horizon Telescope Results. I. The Shadow of the Supermassive Black Hole. *The Astrophysical Journal*, 875:L1, Apr. 2019. ISSN 0004-637X. doi: 10.3847/2041-8213/ab0ec7. URL https://ui.adsabs.harvard.edu/abs/2019ApJ...875L...1E. ADS Bibcode: 2019ApJ...875L...1E.

E. et al. First Sagittarius A* Event Horizon Telescope Results. I. The Shadow of the Supermassive Black Hole in the Center of the Milky Way. *The Astrophysical Journal*, 930:L12, May 2022. ISSN 0004-637X. doi: 10.3847/2041-8213/ac6674. URL https://ui.adsabs.harvard.edu/abs/2022ApJ...930L..12E. ADS Bibcode: 2022ApJ...930L..12E.

L. et al. Observation of Gravitational Waves from a Binary Black Hole Merger. *Physical Review Letters*, 116(6):061102, Feb. 2016. ISSN 0031-9007, 1079-7114. doi: 10.1103/PhysRevLett.116.061102. URL https://link.aps.org/doi/10.1103/PhysRevLett.116.061102.

L. et al. GW170814: A Three-Detector Observation of Gravitational Waves from a Binary Black Hole Coalescence. *Physical Review Letters*, 119(14):141101, Oct. 2017. ISSN 0031-9007, 1079-7114. doi: 10.1103/PhysRevLett.119.141101. URL https://link.aps.org/doi/10.1103/PhysRevLett.119.141101.

A. J. Farmer and E. S. Phinney. The gravitational wave background from cosmological compact binaries. *Monthly Notices of the Royal Astronomical Society*, 346(4):1197–1214, 2003.

L. Ferrarese and H. Ford. Supermassive Black Holes in Galactic Nuclei: Past, Present and Future Research. *Space Science Reviews*, 116(3-4):523–624, Feb. 2005. ISSN 0038-6308, 1572-9672. doi: 10.1007/s11214-005-3947-6. URL http://link.springer.com/10.1007/s11214-005-3947-6.

C. Flammarion. The Companion of Sirius. *Astronomical register*, 15:186–189, Jan. 1877. URL https://ui.adsabs.harvard.edu/abs/1877AReg...15..186F. ADS Bibcode: 1877AReg...15..186F.

R. Flauger, N. Karnesis, G. Nardini, M. Pieroni, A. Ricciardone, and J. Torrado. Improved reconstruction of a stochastic gravitational wave background with lisa. *Journal of Cosmology and Astroparticle Physics*, 2021(01):059, 2021.

D. A. Forbes, P. Lasky, A. W. Graham, and L. Spitler. Uniting old stellar systems: from globular clusters to giant ellipticals: Uniting old stellar systems. *Monthly Notices of the Royal Astronomical Society*, 389(4):1924–1936, Oct. 2008. ISSN 00358711. doi: 10.1111/j.1365-2966.2008.13739.x. URL https://academic.oup.com/mnras/article-lookup/doi/10.1111/j.1365-2966.2008.13739.x.

N. P. Gentile Fusillo, P.-E. Tremblay, E. Cukanovaite, A. Vorontseva, R. Lallement, M. Hollands, B. T. Gänsicke, K. B. Burdge, J. McCleery, and S. Jordan. A catalogue of white dwarfs in *Gaia* EDR3. *Monthly Notices of the Royal Astronomical Society*, 508 (3):3877–3896, Oct. 2021. ISSN 0035-8711, 1365-2966. doi: 10.1093/mnras/stab2672. URL https://academic.oup.com/mnras/article/508/3/3877/6373953.

A. M. Ghez, B. L. Klein, M. Morris, and E. E. Becklin. High Proper-Motion Stars in the Vicinity of Sagittarius A*: Evidence for a Supermassive Black Hole at the Center of Our Galaxy. *The Astrophysical Journal*, 509(2):678–686, Dec. 1998. ISSN 0004-637X, 1538-4357. doi: 10.1086/306528. URL https://iopscience.iop.org/article/10.1086/306528.

M. Gieles, D. Erkal, F. Antonini, E. Balbinot, and J. Peñarrubia. A supra-massive population of stellar-mass black holes in the globular cluster Palomar 5. *Nature Astronomy*, 5(9):957–966, July 2021. ISSN 2397-3366. doi: 10.1038/s41550-021-01392-2. URL https://www.nature.com/articles/s41550-021-01392-2.

M. Giersz and D. C. Heggie. Statistics of N-body simulations – III. Unequal masses. *Monthly Notices of the Royal Astronomical Society*, 279(3):1037–1056, Apr. 1996. ISSN 0035-8711, 1365-2966. doi: 10.1093/mnras/279.3.1037. URL https://academic.oup.com/mnras/article-lookup/doi/10.1093/mnras/279.3.1037.

J. A. González, U. Sperhake, B. Brügmann, M. Hannam, and S. Husa. Maximum Kick from Nonspinning Black-Hole Binary Inspiral. *Physical Review Letters*, 98(9):091101, Feb. 2007. ISSN 0031-9007, 1079-7114. doi: 10.1103/PhysRevLett.98.091101. URL https://link.aps.org/doi/10.1103/PhysRevLett.98.091101.

A. Gualandris and D. Merritt. Ejection of Supermassive Black Holes from Galaxy Cores. *The Astrophysical Journal*, 678(2):780–797, May 2008. ISSN 0004-637X, 1538-4357. doi: 10.1086/586877. URL https://iopscience.iop.org/article/10.1086/586877.

H.-K. Guo, K. Sinha, and C. Sun. Probing boson stars with extreme mass ratio inspirals. *Journal of Cosmology and Astroparticle Physics*, 2019(09):032–032, Sept. 2019. ISSN 1475-7516. doi: 10.1088/1475-7516/2019/09/032. URL https://iopscience.iop.org/article/10.1088/1475-7516/2019/09/032.

Y. Hagihara, N. Era, D. Iikawa, A. Nishizawa, and H. Asada. Constraining extra gravitational wave polarizations with Advanced LIGO, Advanced Virgo, and KAGRA and upper bounds from GW170817. *Physical Review D*, 100(6):064010, Sept. 2019. ISSN 2470-0010, 2470-0029. doi: 10.1103/PhysRevD.100.064010. URL https://link.aps.org/doi/10.1103/PhysRevD.100.064010.

K. M. Hamren, G. H. Smith, P. Guhathakurta, A. E. Dolphin, D. R. Weisz, A. Rajan, and C. J. Grillmair. *HST* /WFC3 OBSERVATIONS OF LOW-MASS GLOBULAR CLUSTERS AM 4 AND PALOMAR 13: PHYSICAL PROPERTIES AND

IMPLICATIONS FOR MASS LOSS. *The Astronomical Journal*, 146(5):116, Oct. 2013. ISSN 0004-6256, 1538-3881. doi: 10.1088/0004-6256/146/5/116. URL https://iopscience.iop.org/article/10.1088/0004-6256/146/5/116.

J. B. Hartle. Gravity: an introduction to Einstein's general relativity, 2003.

S. W. Hawking and W. Israel. *Three hundred years of gravitation*. Cambridge University Press, 1989.

A. Hewish, S. J. Bell, J. D. H. Pilkington, P. F. Scott, and R. A. Collins. Observation of a Rapidly Pulsating Radio Source. *Nature*, 217:709–713, Feb. 1968. ISSN 0028-0836. doi: 10.1038/217709a0. URL https://ui.adsabs.harvard.edu/abs/1968Natur.217..709H. ADS Bibcode: 1968Natur.217..709H.

J. D. Hogg, L. Blecha, C. S. Reynolds, K. L. Smith, and L. M. Winter. 2MASX J00423991 + 3017515: an offset active galactic nucleus in an interacting system. *Monthly Notices of the Royal Astronomical Society*, 503(2):1688–1702, Mar. 2021. ISSN 0035-8711, 1365-2966. doi: 10.1093/mnras/stab576. URL https://academic.oup.com/mnras/article/503/2/1688/6166760.

C. Hopman and T. Alexander. Resonant Relaxation near a Massive Black Hole: The Stellar Distribution and Gravitational Wave Sources. *The Astrophysical Journal*, 645 (2):1152–1163, July 2006. ISSN 0004-637X, 1538-4357. doi: 10.1086/504400. URL https://iopscience.iop.org/article/10.1086/504400.

F. A. Jenet and J. D. Romano. Understanding the gravitational-wave Hellings and Downs curve for pulsar timing arrays in terms of sound and electromagnetic waves. 2014. doi: 10.48550/ARXIV.1412.1142. URL https://arxiv.org/abs/1412.1142. Publisher: arXiv Version Number: 2.

P. G. Jonker and G. Nelemans. The distances to Galactic low-mass X-ray binaries: consequences for black hole luminosities and kicks. *Monthly Notices of the Royal Astronomical Society*, 354:355–366, Oct. 2004. ISSN 0035-8711. doi: 10.1111/j.1365-2966.2004.08193.x. URL https://ui.adsabs.harvard.edu/abs/2004MNRAS.354..355J. ADS Bibcode: 2004MNRAS.354..355J.

P. R. Kafle, S. Sharma, G. F. Lewis, and J. Bland-Hawthorn. On the Shoulders of Giants: Properties of the Stellar Halo and the Milky Way Mass Distribution. *The Astrophysical Journal*, 794:59, Oct. 2014. ISSN 0004-637X. doi: 10.1088/0004-637X/794/1/59. URL https://ui.adsabs.harvard.edu/abs/2014ApJ...794...59K. ADS Bibcode: 2014ApJ...794...59K.

M. Kamionkowski, A. Kosowsky, and A. Stebbins. A Probe of Primordial Gravity Waves and Vorticity. *Physical Review Letters*, 78(11):2058–2061, Mar. 1997. ISSN 0031-9007, 1079-7114. doi: 10.1103/PhysRevLett.78.2058. URL https://link.aps.org/doi/10.1103/PhysRevLett.78.2058.

M. Kilic, J. R. Thorstensen, P. M. Kowalski, and J. Andrews. 11-12 Gyr old white dwarfs 30 pc away: 11-12 Gyr old WDs. *Monthly Notices of the Royal Astronomical Society: Letters*, 423(1):L132–L136, June 2012. ISSN 17453925. doi: 10.1111/j.

1745-3933.2012.01271.x. URL https://academic.oup.com/mnrasl/article/423/1/L132-L136/1074102.

D. Kim, H. Jerjen, D. Mackey, G. S. Da Costa, and A. P. Milone. KIM 3: AN ULTRA-FAINT STAR CLUSTER IN THE CONSTELLATION OF CENTAURUS. *The Astrophysical Journal*, 820(2):119, Mar. 2016. ISSN 1538-4357. doi: 10.3847/0004-637X/820/2/119. URL https://iopscience.iop.org/article/10.3847/0004-637X/820/2/119.

S. Komossa and D. Merritt. Tidal Disruption Flares from Recoiling Supermassive Black Holes. *The Astrophysical Journal*, 683(1):L21–L24, Aug. 2008. ISSN 0004-637X, 1538-4357. doi: 10.1086/591420. URL https://iopscience.iop.org/article/10.1086/591420.

S. Komossa, H. Zhou, and H. Lu. A Recoiling Supermassive Black Hole in the Quasar SDSS J092712.65+294344.0? *The Astrophysical Journal*, 678(2):L81–L84, May 2008. ISSN 0004-637X, 1538-4357. doi: 10.1086/588656. URL https://iopscience.iop.org/article/10.1086/588656.

R. A. Konoplya and A. Zhidenko. Quasinormal modes of black holes: From astrophysics to string theory. *Reviews of Modern Physics*, 83(3):793–836, July 2011. ISSN 0034-6861, 1539-0756. doi: 10.1103/RevModPhys.83.793. URL https://link.aps.org/doi/10.1103/RevModPhys.83.793.

S. Koposov, J. T. A. de Jong, V. Belokurov, H. W. Rix, D. B. Zucker, N. W. Evans, G. Gilmore, M. J. Irwin, and E. F. Bell. The Discovery of Two Extremely Low Luminosity Milky Way Globular Clusters. *The Astrophysical Journal*, 669:337–342, Nov. 2007. ISSN 0004-637X. doi: 10.1086/521422. URL https://ui.adsabs.harvard.edu/abs/2007ApJ...669..337K. ADS Bibcode: 2007ApJ...669..337K.

J. A. Krommes. An introduction to the physics of the Coulomb logarithm, with emphasis on quantum-mechanical effects. *Journal of Plasma Physics*, 85(1):925850101, Feb. 2019. ISSN 0022-3778, 1469-7807. doi: 10.1017/S0022377818001319. URL https://www.cambridge.org/core/product/identifier/S0022377818001319/type/journal_article.

T. R. Lauer, M. Postman, H. A. Weaver, J. R. Spencer, S. A. Stern, M. W. Buie, D. D. Durda, C. M. Lisse, A. R. Poppe, R. P. Binzel, D. T. Britt, B. J. Buratti, A. F. Cheng, W. M. Grundy, M. Horányi, J. J. Kavelaars, I. R. Linscott, W. B. McKinnon, J. M. Moore, J. I. Núñez, C. B. Olkin, J. W. Parker, S. B. Porter, D. C. Reuter, S. J. Robbins, P. Schenk, M. R. Showalter, K. N. Singer, A. J. Verbiscer, and L. A. Young. New Horizons Observations of the Cosmic Optical Background. *The Astrophysical Journal*, 906(2):77, Jan. 2021. ISSN 0004-637X, 1538-4357. doi: 10.3847/1538-4357/abc881. URL https://iopscience.iop.org/article/10.3847/1538-4357/abc881.

D. Lena, P. G. Jonker, J. P. Rauer, S. Hernandez, and Z. Kostrzewa-Rutkowska. Hypercompact stellar clusters: morphological renditions and spectrophotometric models. *Monthly Notices of the Royal Astronomical Society*, 495(2):1771–1787, June 2020. ISSN 0035-8711, 1365-2966. doi: 10.1093/mnras/staa1174. URL https://academic.oup.com/mnras/article/495/2/1771/5831081.

Z.-C. Liang, Y.-M. Hu, Y. Jiang, J. Cheng, J.-d. Zhang, J. Mei, et al. Science with the tianqin observatory: Preliminary results on stochastic gravitational-wave background. *Physical Review D*, 105(2):022001, 2022.

LIGO Scientific Collaboration, Virgo Collaboration, and KAGRA Collaboration et al. Upper limits on the isotropic gravitational-wave background from Advanced LIGO and Advanced Virgo's third observing run. *Physical Review D*, 104(2):022004, July 2021. ISSN 2470-0010, 2470-0029. doi: 10.1103/PhysRevD.104.022004. URL https://link.aps.org/doi/10.1103/PhysRevD.104.022004.

LIGO Scientific Collaboration, Virgo Collaboration, and KAGRA Collaboration and others. Search for anisotropic gravitational-wave backgrounds using data from Advanced LIGO and Advanced Virgo's first three observing runs. *Physical Review D*, 104(2): 022005, July 2021. ISSN 2470-0010, 2470-0029. doi: 10.1103/PhysRevD.104.022005. URL https://link.aps.org/doi/10.1103/PhysRevD.104.022005.

D. N. C. Lin and S. Tremaine. A reinvestigation of the standard model for the dynamics of a massive black hole in a globular cluster. *The Astrophysical Journal*, 242:789–798, Dec. 1980. ISSN 0004-637X. doi: 10.1086/158513. URL https://ui.adsabs.harvard.edu/abs/1980ApJ...242..789L. ADS Bibcode: 1980ApJ...242..789L.

A. D. Mackey, M. I. Wilkinson, M. B. Davies, and G. F. Gilmore. Black holes and core expansion in massive star clusters. *Monthly Notices of the Royal Astronomical Society*, 386(1):65–95, May 2008. ISSN 00358711, 13652966. doi: 10.1111/j.1365-2966.2008.13052.x. URL https://academic.oup.com/mnras/article-lookup/doi/10.1111/j.1365-2966.2008.13052.x.

P. Madau and M. Dickinson. Cosmic Star-Formation History. *Annual Review of Astronomy and Astrophysics*, 52(1):415–486, 2014. doi: 10.1146/annurev-astro-081811-125615. URL https://doi.org/10.1146/annurev-astro-081811-125615. _eprint: https://doi.org/10.1146/annurev-astro-081811-125615.

D. Massari, H. H. Koppelman, and A. Helmi. Origin of the system of globular clusters in the Milky Way. *Astronomy and Astrophysics*, 630:L4, Oct. 2019. ISSN 0004-6361. doi: 10.1051/0004-6361/201936135. URL https://ui.adsabs.harvard.edu/abs/2019A&A...630L...4M. ADS Bibcode: 2019A&A...630L...4M.

S. D. Mathur. The information paradox: a pedagogical introduction. *Classical and Quantum Gravity*, 26(22):224001, Nov. 2009. ISSN 0264-9381, 1361-6382. doi: 10.1088/0264-9381/26/22/224001. URL https://iopscience.iop.org/article/10.1088/0264-9381/26/22/224001.

S. Mau, A. Drlica-Wagner, K. Bechtol, A. B. Pace, T. Li, M. Soares-Santos, N. Kuropatkin, S. Allam, D. Tucker, L. Santana-Silva, B. Yanny, P. Jethwa, A. Palmese, K. Vivas, C. Burgad, H.-Y. Chen, and (BLISS Collaboration). A Faint Halo Star Cluster Discovered in the Blanco Imaging of the Southern Sky Survey. *The Astrophysical Journal*, 875(2):154, Apr. 2019. ISSN 1538-4357. doi: 10.3847/1538-4357/ab0bb8. URL https://iopscience.iop.org/article/10.3847/1538-4357/ab0bb8.

S. Mau et al. Two Ultra-faint Milky Way Stellar Systems Discovered in Early Data from the DECam Local Volume Exploration Survey. *The Astrophysical Journal*, 890 (2):136, Feb. 2020. ISSN 1538-4357. doi: 10.3847/1538-4357/ab6c67. URL https://iopscience.iop.org/article/10.3847/1538-4357/ab6c67.

D. R. Mayerson, A. M. Charles, and J. E. Golec. *Relativity: A Journey Through Warped Space and Time*. Springer International Publishing, Cham, 2019. ISBN 978-3-030-18913-6 978-3-030-18914-3. doi: 10.1007/978-3-030-18914-3. URL http://link.springer.com/10.1007/978-3-030-18914-3.

N. J. McConnell and C.-P. Ma. REVISITING THE SCALING RELATIONS OF BLACK HOLE MASSES AND HOST GALAXY PROPERTIES. *The Astrophysical Journal*, 764(2):184, Feb. 2013. ISSN 0004-637X, 1538-4357. doi: 10.1088/0004-637X/764/2/184. URL https://iopscience.iop.org/article/10.1088/0004-637X/764/2/184.

D. Merritt. Mass Deficits, Stalling Radii, and the Merger Histories of Elliptical Galaxies. *The Astrophysical Journal*, 648:976–986, Sept. 2006. ISSN 0004-637X. doi: 10.1086/506139. URL https://ui.adsabs.harvard.edu/abs/2006ApJ...648..976M. ADS Bibcode: 2006ApJ...648..976M.

D. Merritt. Loss Cone Dynamics. *Classical and Quantum Gravity*, 30(24):244005, Dec. 2013. ISSN 0264-9381, 1361-6382. doi: 10.1088/0264-9381/30/24/244005. URL http://arxiv.org/abs/1307.3268. arXiv:1307.3268 [astro-ph].

D. Merritt, S. Piatek, S. P. Zwart, and M. Hemsendorf. Core Formation by a Population of Massive Remnants. *The Astrophysical Journal*, 608(1):L25–L28, June 2004. ISSN 0004-637X, 1538-4357. doi: 10.1086/422252. URL https://iopscience.iop.org/article/10.1086/422252.

D. Merritt, J. D. Schnittman, and S. Komossa. HYPERCOMPACT STELLAR SYSTEMS AROUND RECOILING SUPERMASSIVE BLACK HOLES. *The Astrophysical Journal*, 699(2):1690–1710, July 2009. ISSN 0004-637X, 1538-4357. doi: 10.1088/0004-637X/699/2/1690. URL https://iopscience.iop.org/article/10.1088/0004-637X/699/2/1690.

G. Meylan and D. C. Heggie. Internal dynamics of globular clusters. *Astronomy and Astrophysics Review*, 8:1–143, Jan. 1997. ISSN 0935-4956. doi: 10.1007/s001590050008. URL https://ui.adsabs.harvard.edu/abs/1997A&ARv...8....1M. ADS Bibcode: 1997A&ARv...8....1M.

R. R. Muñoz, P. Côté, F. A. Santana, M. Geha, J. D. Simon, G. A. Oyarzún, P. B. Stetson, and S. G. Djorgovski. A MegaCam Survey of Outer Halo Satellites. III. Photometric and Structural Parameters. *The Astrophysical Journal*, 860(1):66, June 2018. ISSN 1538-4357. doi: 10.3847/1538-4357/aac16b. URL https://iopscience.iop.org/article/10.3847/1538-4357/aac16b.

G. Nelemans, L. R. Yungelson, S. F. Portegies Zwart, and F. Verbunt. Population synthesis for double white dwarfs: I. Close detached systems. *Astronomy & Astrophysics*, 365 (3):491–507, Jan. 2001. ISSN 0004-6361, 1432-0746. doi: 10.1051/0004-6361:20000147. URL http://www.aanda.org/10.1051/0004-6361:20000147.

E. Newman and R. Penrose. An Approach to Gravitational Radiation by a Method of Spin Coefficients. *Journal of Mathematical Physics*, 3(3):566–578, May 1962. ISSN 0022-2488, 1089-7658. doi: 10.1063/1.1724257. URL https://pubs.aip.org/aip/jmp/article/3/3/566-578/387969.

R. M. O'Leary and A. Loeb. Star clusters around recoiled black holes in the Milky Way halo. *Monthly Notices of the Royal Astronomical Society*, 395(2): 781–786, May 2009. ISSN 00358711, 13652966. doi: 10.1111/j.1365-2966.2009.14611.x. URL https://academic.oup.com/mnras/article-lookup/doi/10.1111/j.1365-2966.2009.14611.x.

R. M. O'Leary and A. Loeb. Recoiled star clusters in the Milky Way halo: N-body simulations and a candidate search through SDSS. *Monthly Notices of the Royal Astronomical Society*, 421(4):2737–2750, Apr. 2012. ISSN 00358711. doi: 10.1111/j.1365-2966.2011.20078.x. URL http://arxiv.org/abs/1102.3695. arXiv:1102.3695 [astro-ph, physics:gr-qc].

P. C. Peters and J. Mathews. Gravitational Radiation from Point Masses in a Keplerian Orbit. *Physical Review*, 131(1):435–440, July 1963. ISSN 0031-899X. doi: 10.1103/PhysRev.131.435. URL https://link.aps.org/doi/10.1103/PhysRev.131.435.

E. Phinney. A practical theorem on gravitational wave backgrounds. *arXiv preprint astro-ph/0108028*, 2001.

Planck Collaboration et al. *Planck* 2018 results: VI. Cosmological parameters. *Astronomy & Astrophysics*, 641:A6, Sept. 2020. ISSN 0004-6361, 1432-0746. doi: 10.1051/0004-6361/201833910. URL https://www.aanda.org/10.1051/0004-6361/201833910.

S. F. Portegies Zwart and F. Verbunt. Population synthesis of high-mass binaries. *Astronomy and Astrophysics*, 309:179–196, May 1996. ISSN 0004-6361. URL https://ui.adsabs.harvard.edu/abs/1996A&A...309..179P. ADS Bibcode: 1996A&A...309..179P.

S. F. Portegies Zwart and L. R. Yungelson. Formation and evolution of binary neutron stars. *Astronomy and Astrophysics*, 332:173–188, Apr. 1998. ISSN 0004-6361. doi: 10.48550/arXiv.astro-ph/9710347. URL https://ui.adsabs.harvard.edu/abs/1998A&A...332..173P. ADS Bibcode: 1998A&A...332..173P.

T. Regimbau. The astrophysical gravitational wave stochastic background. *Research in Astronomy and Astrophysics*, 11(4):369–390, Apr. 2011. ISSN 1674-4527. doi: 10.1088/1674-4527/11/4/001. URL https://iopscience.iop.org/article/10.1088/1674-4527/11/4/001.

A. I. Renzini, B. Goncharov, A. C. Jenkins, and P. M. Meyers. Stochastic gravitational-wave backgrounds: Current detection efforts and future prospects. *Galaxies*, 10(1):34, 2022.

P. A. Rosado. Gravitational wave background from binary systems. *Physical Review D*, 84(8):084004, 2011.

R. K. Sachs. Gravitational Waves in General Relativity. VIII. Waves in Asymptotically Flat Space-Time. *Proceedings of the Royal Society of London Series A*, 270:103–126, Oct. 1962. ISSN 0080-46301364-5021. doi: 10.1098/rspa.1962.0206. URL https://ui.adsabs.harvard.edu/abs/1962RSPSA.270..103S. ADS Bibcode: 1962RSPSA.270..103S.

H. Sana, S. E. De Mink, A. De Koter, N. Langer, C. J. Evans, M. Gieles, E. Gosset, R. G. Izzard, J.-B. Le Bouquin, and F. R. N. Schneider. Binary Interaction Dominates the Evolution of Massive Stars. *Science*, 337(6093):444–446, July 2012. ISSN 0036-8075, 1095-9203. doi: 10.1126/science.1223344. URL https://www.science.org/doi/10.1126/science.1223344.

R. Schneider, V. Ferrari, S. Matarrese, and S. F. Portegies Zwart. Low-frequency gravitational waves from cosmological compact binaries. *Monthly Notices of the Royal Astronomical Society*, 324(4):797–810, 2001.

D. Sotillo-Ramos, A. Pillepich, M. Donnari, D. Nelson, L. Eisert, V. Rodriguez-Gomez, G. Joshi, M. Vogelsberger, and L. Hernquist. The merger and assembly histories of Milky Way- and M31-like galaxies with TNG50: disc survival through mergers. *Monthly Notices of the Royal Astronomical Society*, 516(4):5404–5427, Sept. 2022. ISSN 0035-8711, 1365-2966. doi: 10.1093/mnras/stac2586. URL https://academic.oup.com/mnras/article/516/4/5404/6702434.

L. Spitzer, Jr. and M. H. Hart. Random Gravitational Encounters and the Evolution of Spherical Systems. I. Method. *The Astrophysical Journal*, 164:399, Mar. 1971. ISSN 0004-637X, 1538-4357. doi: 10.1086/150855. URL http://adsabs.harvard.edu/doi/10.1086/150855.

S. Staelens, D. R. Mayerson, F. Bacchini, B. Ripperda, and L. Küchler. Black hole photon rings beyond general relativity, 2023.

J. H. Taylor, L. A. Fowler, and P. M. McCulloch. Measurements of general relativistic effects in the binary pulsar PSR1913 + 16. *Nature*, 277(5696):437–440, Feb. 1979. ISSN 0028-0836, 1476-4687. doi: 10.1038/277437a0. URL https://www.nature.com/articles/277437a0.

S. Toonen, G. Nelemans, and S. Portegies Zwart. Supernova Type Ia progenitors from merging double white dwarfs: Using a new population synthesis model. *Astronomy & Astrophysics*, 546:A70, Oct. 2012. ISSN 0004-6361, 1432-0746. doi: 10.1051/0004-6361/201218966. URL http://www.aanda.org/10.1051/0004-6361/201218966.

S. Torres, A. Rebassa-Mansergas, M. E. Camisassa, and R. Raddi. The Gaia DR2 halo white dwarf population: the luminosity function, mass distribution and its star formation history. *Monthly Notices of the Royal Astronomical Society*, 502(2):1753–1767, Feb. 2021. ISSN 0035-8711, 1365-2966. doi: 10.1093/mnras/stab079. URL http://arxiv.org/abs/2101.03341. arXiv:2101.03341 [astro-ph].

P.-E. Tremblay, J. Cummings, J. S. Kalirai, B. T. Gänsicke, N. Gentile-Fusillo, and R. Raddi. The field white dwarf mass distribution. *Monthly Notices of the Royal Astronomical Society*, 461(2):2100–2114, Sept. 2016. ISSN 0035-8711, 1365-2966. doi:

10.1093/mnras/stw1447. URL https://academic.oup.com/mnras/article-lookup/doi/10.1093/mnras/stw1447.

A. Van Maanen. TWO FAINT STARS WITH LARGE PROPER MOTION. *Publications of the Astronomical Society of the Pacific*, 29(172):258–258, Dec. 1917. ISSN 0004-6280, 1538-3873. doi: 10.1086/122654. URL https://iopscience.iop.org/article/10.1086/122654.

E. Vasiliev. A New Fokker–Planck Approach for the Relaxation-driven Evolution of Galactic Nuclei. *The Astrophysical Journal*, 848(1):10, Oct. 2017. ISSN 1538-4357. doi: 10.3847/1538-4357/aa8cc8. URL https://iopscience.iop.org/article/10.3847/1538-4357/aa8cc8.

E. Vasiliev. AGAMA: action-based galaxy modelling architecture. *Monthly Notices of the Royal Astronomical Society*, 482(2):1525–1544, Jan. 2019. ISSN 0035-8711, 1365-2966. doi: 10.1093/mnras/sty2672. URL https://academic.oup.com/mnras/article/482/2/1525/5114593.

E. Vasiliev, F. Antonini, and D. Merritt. THE FINAL-PARSEC PROBLEM IN THE COLLISIONLESS LIMIT. *The Astrophysical Journal*, 810(1):49, Aug. 2015. ISSN 1538-4357. doi: 10.1088/0004-637X/810/1/49. URL https://iopscience.iop.org/article/10.1088/0004-637X/810/1/49.

F. Verbunt and S. Rappaport. Mass transfer instabilities due to angular momentum flows in close binaries. *The Astrophysical Journal*, 332:193, Sept. 1988. ISSN 0004-637X, 1538-4357. doi: 10.1086/166645. URL http://adsabs.harvard.edu/doi/10.1086/166645.

M. Volonteri. Formation of supermassive black holes. *The Astronomy and Astrophysics Review*, 18(3):279–315, July 2010. ISSN 0935-4956, 1432-0754. doi: 10.1007/s00159-010-0029-x. URL http://link.springer.com/10.1007/s00159-010-0029-x.

F. Wang, J. Yang, X. Fan, J. F. Hennawi, A. J. Barth, E. Banados, F. Bian, K. Boutsia, T. Connor, F. B. Davies, R. Decarli, A.-C. Eilers, E. P. Farina, R. Green, L. Jiang, J.-T. Li, C. Mazzucchelli, R. Nanni, J.-T. Schindler, B. Venemans, F. Walter, X.-B. Wu, and M. Yue. A Luminous Quasar at Redshift 7.642. *The Astrophysical Journal Letters*, 907(1):L1, Jan. 2021. ISSN 2041-8205, 2041-8213. doi: 10.3847/2041-8213/abd8c6. URL https://iopscience.iop.org/article/10.3847/2041-8213/abd8c6.

B. L. Webster and P. Murdin. Cygnus X-1—a Spectroscopic Binary with a Heavy Companion ? *Nature*, 235(5332):37–38, Jan. 1972. ISSN 0028-0836, 1476-4687. doi: 10.1038/235037a0. URL https://www.nature.com/articles/235037a0.

N. Yunes and X. Siemens. Gravitational-Wave Tests of General Relativity with Ground-Based Detectors and Pulsar-Timing Arrays. *Living Reviews in Relativity*, 16(1):9, Dec. 2013. ISSN 2367-3613, 1433-8351. doi: 10.12942/lrr-2013-9. URL http://link.springer.com/10.12942/lrr-2013-9.

Appendices

Appendix A

General Relativity

This Appendix provides a bit of background on general relativity and the Einstein equations (A.4). Readers who are not very familiar with Einstein's theory should consult a complete and more pedagogical introduction, e.g. [Carroll, 2019, Hartle, 2003, Mayerson et al., 2019]. This section does not treat the beautiful physics behind special relativity and the equivalence principle, nor does it provide a full explanation of tensor calculus; it simply presents the necessary formulas. The majority of this section is based on [Carroll, 2019].

We are used to thinking of space and time as separate concepts. One of the essential conceptual steps in understanding GR is to drop this point of view, and to start thinking of space and time together: **spacetime** is a four-dimensional construct that encompasses both, and puts them on a more equal footing.

The central object of interest in GR is the **metric tensor** $g_{\mu\nu}$, which describes the spacetime of interest. Through this coupling of space and time, infinitely many spacetimes are possible, each with distinct properties and uses. Among these possibilities are the black hole metrics, which are most relevant for this project. However, many other spacetimes exist, with some famous ones being (anti-)de Sitter space and FLRW metrics.

The indices μ, ν can take the values 0,1,2,3. The first is associated with the time-like dimension, and the others correspond to the spatial dimensions. It is important whether indices are written *up* or *down*. For example, the metric with indices down, $g_{\mu\nu}$, is called the **covariant** metric, whereas the metric with upper indices, $g^{\mu\nu}$ is called the **contravariant** metric. Similarly, any covariant four-vector A_μ also has a contravariant counterpart A^μ. The metric provides the correspondence between both, as

$$A^\mu = g^{\mu\nu} A_\nu \,.$$

A few comments are appropriate here. First of all, the name that we give to an index, i.e. μ, ν or even α, is not important. Secondly, the formula above makes use of the **Einstein summation convention**, which dictates that repeated indices on the same side of the equality are summed over (also referred to as *contracting the indices*). Therefore, the expression above should be interpreted as

$$A^\mu = g^{\mu 0} A_0 + g^{\mu 1} A_1 + g^{\mu 2} A_2 + g^{\mu 3} A_3 \,.$$

This summation convention is very useful, to avoid explicitly writing all the summations that appear in formulas. The index μ is called a free index, as it appears in both sides of the equation without being summed over. Often, instead of using the numbers 0,1,2,3 the coordinates to which they refer are used as indices. Explicitly, in the case of spherical coordinates $(x^0, x^1, x^2, x^3) \equiv (t, r, \theta, \phi)$, the indices are often written as e.g. $g_{tt} \equiv g_{00}$. More rules apply to these indices, but they are not treated here.

The metric appears in the formula for the **line-element** (which is sometimes also referred to as the metric):

$$\mathrm{d}s^2 = g_{\mu\nu}(x)\mathrm{d}x^\mu \mathrm{d}x^\nu \,. \tag{A.1}$$

The x^μ are called the coordinates, and the metric can depend on them. Coordinates are not determined uniquely, and changing them is possible if the metric is transformed along with them. This line-element determines the distance between points in spacetime. Keeping the summation convention in mind, the expression (A.1) should be interpreted as

$$\mathrm{d}s^2 = \sum_{\mu,\nu=0}^{3} g_{\mu\nu}(x)\mathrm{d}x^\mu \mathrm{d}x^\nu = g_{00}(x)\mathrm{d}x^0\mathrm{d}x^0 + g_{10}(x)\mathrm{d}x^1\mathrm{d}x^0 + \dots$$

highlighting the merit of the summation convention once again. Furthermore, it should be noted that the metric has the special property that it is *symmetric*, meaning that $g_{\mu\nu} = g_{\nu\mu}$. Arguably, the most important metric is that of **flat spacetime**. This is the metric in the absence of any mass, energy or black hole. It is often referred to as the **Minkowski metric**, and is in its simplest form written as

$$\mathrm{d}s^2 = -c^2\mathrm{d}t^2 + \mathrm{d}x^2 + \mathrm{d}y^2 + \mathrm{d}z^2 \,. \tag{A.2}$$

The constant c is the speed of light, and the coordinate t corresponds to the time. The other three coordinates can be thought of as Cartesian coordinates in a three-dimensional space. It is often written in terms of spherical coordinates:

$$\mathrm{d}s^2 = -c^2\mathrm{d}t^2 + \mathrm{d}r^2 + r^2\left(\mathrm{d}\theta^2 + \sin^2\theta\mathrm{d}\phi^2\right) \,. \tag{A.3}$$

This may look different, but describes the exact same flat spacetime that is described by (A.2).

In principle one could invent any metric, but the "allowed" metrics in GR are the ones that solve the **Einstein equations**

$$R_{\mu\nu} - \frac{1}{2}Rg_{\mu\nu} = \frac{8\pi G}{c^4}T_{\mu\nu} \,. \tag{A.4}$$

This equation features the **Ricci tensor** $R_{\mu\nu}$ and **scalar** R on the left-hand side, which depend on the metric in a complex way. Therefore, the left-hand side describes the *geometry* - and more specifically, the *curvature* - of the spacetime. The right-hand side contains the energy-momentum tensor $T_{\mu\nu}$, which depends on the matter and energy content that is present in the spacetime. This equation has a beautiful interpretation, which can be stated as

Matter and energy curve spacetime.

The equation (A.4) reduces to Newton's laws in the non-relativistic limit, where masses are small and speeds are small compared to the speed of light c. The **Einstein equations in vacuum**, which correspond to setting the energy-momentum tensor $T_{\mu\nu}$ to zero in (A.4), is the starting point when studying black holes or gravitational waves. Contracting the indices on the left-hand side shows that these are equivalent to

$$R_{\mu\nu} = 0\,. \tag{A.5}$$

Given the central role of the speed of light in the theory, it appears in almost every equation. In order to avoid writing it all the time, which would render equations less transparent, physicists have thought of a way to get rid of all the c's. This is done by switching to **natural units**. Essentially, this is similar to switching from SI-units to e.g. cgs-units. The result is that we can replace every instance of c by 1. As an example, Einstein's famous equation for the rest energy E of a particle with mass m, given by $E = mc^2$, would be written as $E = m$ in natural units. There is a consistent way of recovering the original equations containing c from the ones expressed in natural units, but we will not go into these details here. To add even more complexity, the gravitational constant G can also be set to 1 along with c in a consistent way. This allows us to write equation (A.4) in natural units as

$$R_{\mu\nu} - \frac{1}{2}Rg_{\mu\nu} = 8\pi T_{\mu\nu}\,.$$

While the benefits of these natural units may not immediately be clear from these simple examples, the simplification they provide in more complicated formulas is significant.

Appendix B

Additional Figures

This Appendix provides some additional figures that don't belong in the main text.

B.1 Chapter 2

Figure B.1 shows estimates for the different components of the background sourced by coalescing compact binaries, based on extrapolations of values in [Collaboration et al., 2022, Farmer and Phinney, 2003]. Figures B.2 and B.3 shows the contributions of different redshift bins to 10 different frequency bins, for the alternative SFRs (2.50) - (2.52).

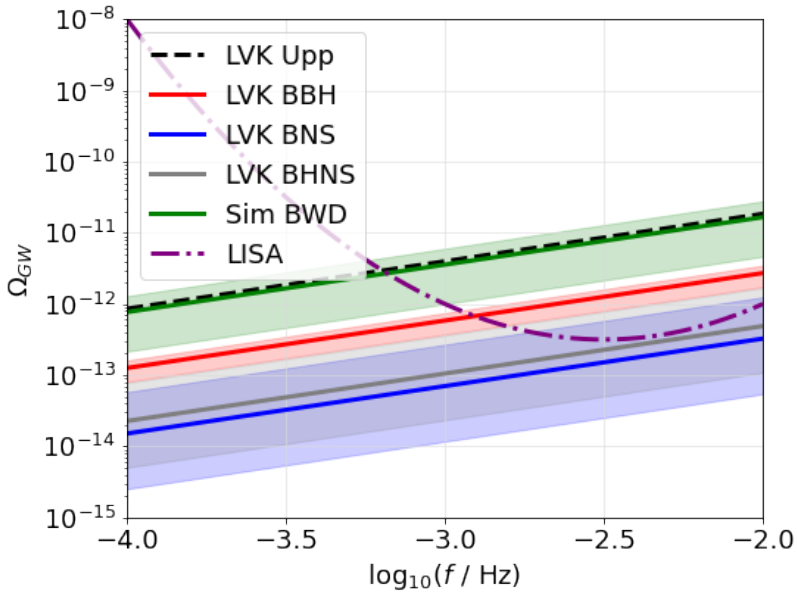

Figure B.1: Comparison of the different components that make up the GWB due to coalescing compact binaries, described by 2.15. The dashed black line describes the extrapolated upper limit on the background as derived in [LIGO Scientific Collaboration, Virgo Collaboration, and KAGRA Collaboration et al., 2021]. The solid lines and shaded regions are the estimates for the backgrounds generated by binary WDs, BHs, NSs and BH-NS binaries [Collaboration et al., 2022, Farmer and Phinney, 2003]. The dot-dash line is a parabola that approximates the sensity curve of the planned LISA mission, for comparison.

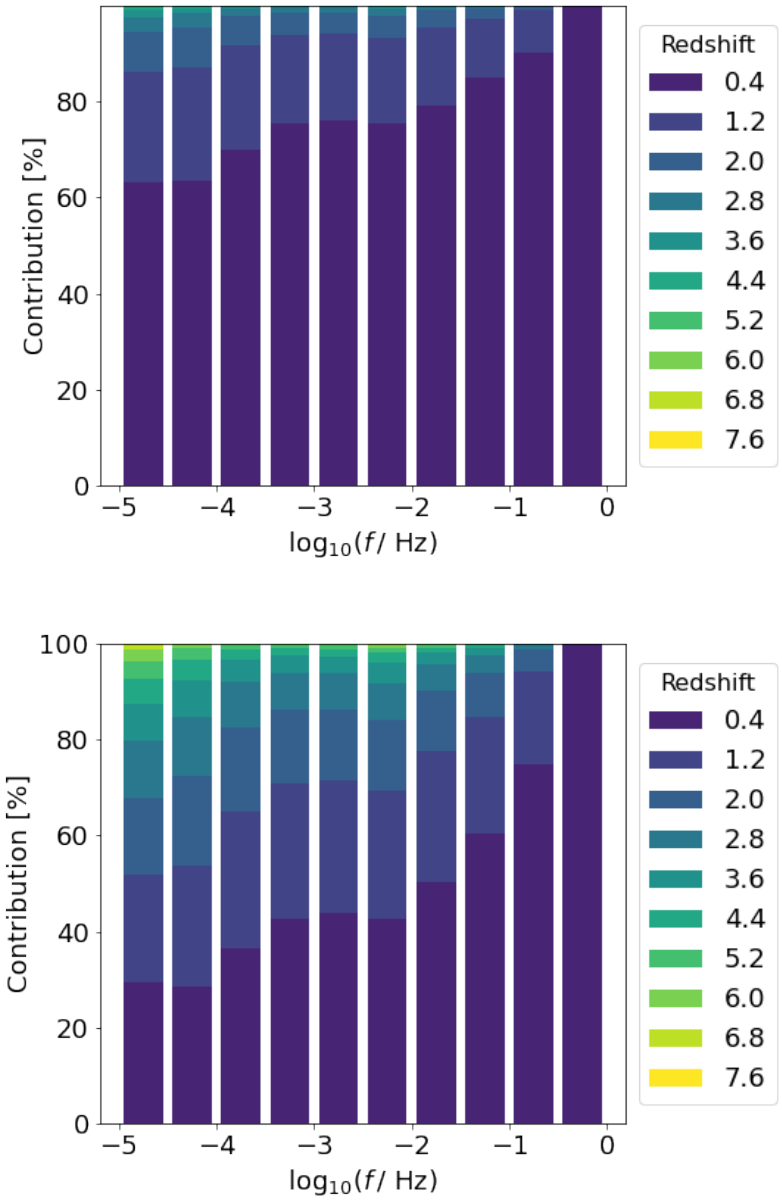

Figure B.2: Contribution of the different redshift bins at different frequencies grouped in 10 frequency bins, for the alternative SFHs (2.50) - (2.51). The size of the rectangle represents the relative contribution. The indicative redshift indicated in the legend is in the middle of the bin, and all have width 0.8.

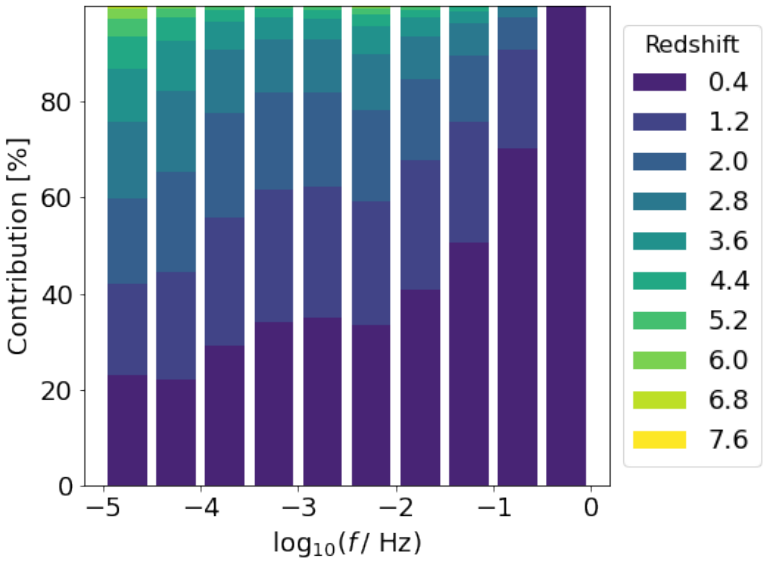

Figure B.3: Contribution of the different redshift bins at different frequencies grouped in 10 frequency bins, for the alternative SFH (2.52). The size of the rectangle represents the relative contribution. The indicative redshift indicated in the legend is in the middle of the bin, and all have width 0.8.

B.2 Chapter 3

Figure B.4 shows that the effective radius r_{eff} grows as $r_{\text{eff}} \propto t^{2/3}$. The dashed lines are drawn according to

$$0.008 + A \cdot t^{2/3}\,, \tag{B.1}$$

where $A = 1.04$ and $A = 0.3$ for the model with and without smBHs, respectively. These are *not* the results of a fitting procedure, but should be considered indicative. Additionally, the model with smBHs is evolved for the first Gyr separately as well, to further confirm the functional behaviour, with respect to Figure 3.4.

Figure B.5 shows the density and enclosed mass profile for the smBH component of our base model, described in Sec. 3.4. Figure B.6 shows a comparison of the enclosed mass profile between the stellar and smBH component.

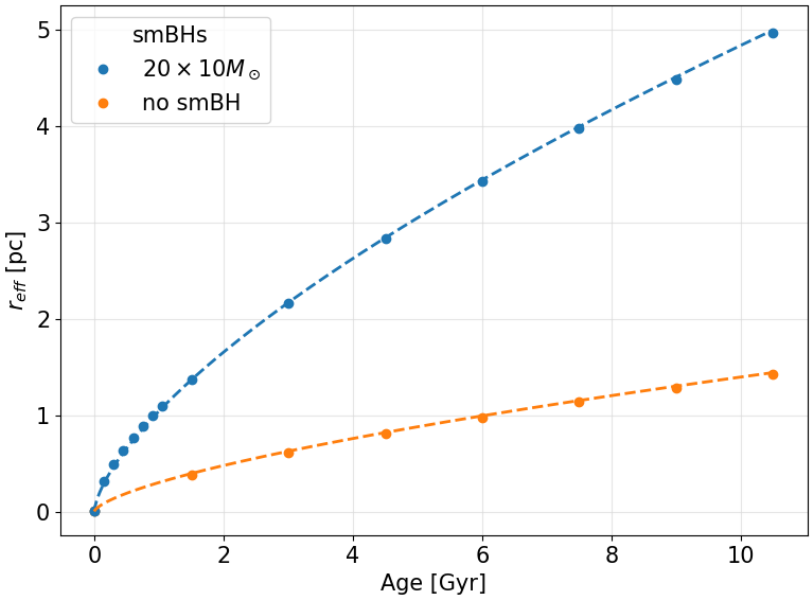

Figure B.4: Figure 3.4, but the dashed lines are now drawn according to $r_{\rm eff} \propto t^{2/3}$. The precise values are given by (B.1) with $A = 1.04$ and $A = 0.3$,

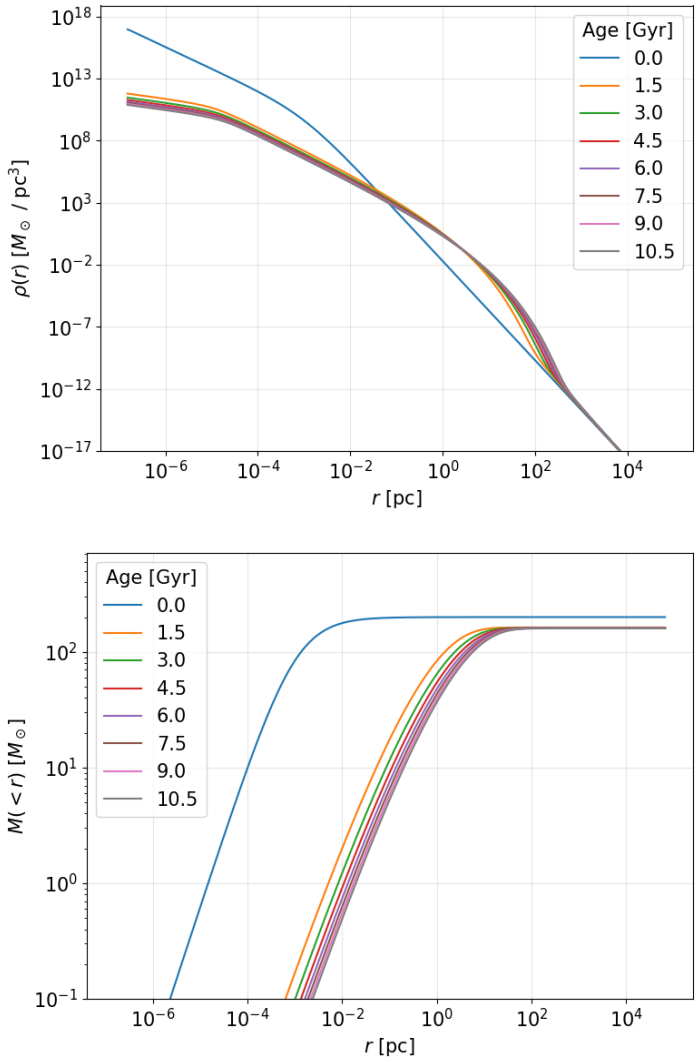

Figure B.5: Density and enclosed mass profile of the smBH population at different times, for $M_\bullet = 10^5 M_\odot, V_k = 325$ km s^{-1} and a population of 20 smBHs of $10 M_\odot$ each. The dashed vertical lines correspond to $r_{\rm eff}$ at the different timesteps, with increasing values for increasing time (see Figure 3.4).

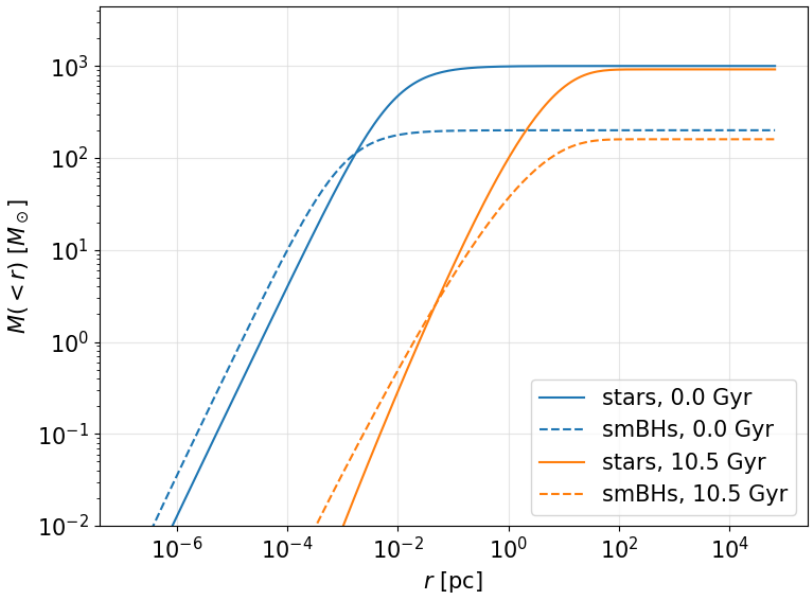

Figure B.6: Comparison of the enclosed mass profile of the stellar and smBH populations, at the start and at the end of the simulation. Initially, they both display the Dehnen profile, as set by the initial conditions. After 10.5 Gyr, the smBHs are concentrated slightly more towards the center, relative to the stellar population. This can be seen from the difference in slope.

DEPARTMENT OF PHYSICS AND ASTRONOMY
Celestijnenlaan 200D bus 2412
3001 LEUVEN, BELGIUM
tel. + 32 16 32 71 24
fys.kuleuven.be